COMBUSTION SYNTHESIS

AND

MECHANICAL PROPERTIES

OF

SiC PARTICULATE REINFORCED MOLYBDENUM DISILICIDE

By

DAMRONGCHAI MANOMAISUPAT, B. Eng. Mgt.

A Thesis

Submitted to the School of Graduate Studies

in Partial Fulfilment of the Requirements

for the Degree

Master of Engineering

McMaster University

SiC PARTICULATE REINFORCED MOLYBDENUM DISILICIDE

MASTER OF ENGINEERING (1995)
(Materials Science and Engineering)

McMASTER UNIVERSITY
Hamilton, Ontario

TITLE: Combustion Synthesis and Mechanical Properties of SiC Particulate Reinforced Molybdenum Disilicide

AUTHOR: Damrongchai Manomaisupat, B. Eng. Mgt. (McMaster University)

SUPERVISOR: Professor D.S. Wilkinson
Professor A. Petric

NUMBER OF PAGES: xii, 192

อุทิศให้

ชาญชัย มโนมัยสุพัฒน์
อรพินทร์ มโนมัยสุพัฒน์

ABSTRACT

Intermetallic composites of molybdenum disilicide reinforced with various amounts of silicon carbide particulate were produced by combustion synthesis from their elemental powders. Elemental powders were mixed stoichiometrically then ball-milled. The cold-pressed mixture was then chemically ignited at one end under vacuum at approximately 700°C. The combustion temperature of the process was approximately 1600°C which was lower than the melting point of molybdenum disilicide. This processing technique allowed the fabrication of the composites at 700°C within a few seconds, instead of sintering at temperatures greater than 1200°C for many hours. The end product was a porous composite, which was densified to >97% of the theoretical density by hot pressing. The grains of the matrix were 8-14 μm in size surrounded by SiC reinforcement of 1-5 μm.

The morphology and structure of the products were studied by x-ray diffraction and scanning electron microscopy (SEM). Samples were prepared for hardness, fracture strength, and toughness testing at room temperature. There were improvements in the mechanical properties of the composites with increasing SiC reinforcement. The hardness of the materials increased from 10.1 ± 0.1 GPa (959 ± 13 kg/mm^2) to 11.7 ± 0.6 GPa (1102 ± 52 kg/mm^2) to 12.7 ± 0.4 GPa (1199 ± 36 kg/mm^2) with the 10 vol% and 20 vol% SiC reinforcement, respectively. The strength increased from 195±39 MPa to 237±39 MPa with 10 vol% and

to 299 ± 43.2 MPa with a 20 vol% SiC reinforcement. The fracture toughness increased from 2.79 ± 0.36 MPa.$m^{1/2}$ to 3.31± 0.41 MPa.$m^{1/2}$ with 10 vol% SiC and to 4.08± 0.30 MPa.$m^{1/2}$ with 20 vol% SiC. The increase in hardness and flexural strength is due to the effective load transfer across the strong interface in the composites. The main toughening mechanism is crack deflection by the residual stress in the materials, induced by the differences in the thermal expansion coefficients and the elastic moduli of the matrix and reinforcement.

ACKNOWLEDGMENTS

Firstly, I would like to thank my parents for their encouragement, patience, support and love throughout my life and education in Canada. Without them I would not have travelled from Thailand to Canada for my education and met friendly Canadians. Also, I would not know what winter, ice hockey and baseball are all about.

I would like to thank my supervisors Dr. D.S. Wilkinson and Dr. A. Petric for allowing me the opportunity to work on my Master's. Their advice, guidance, suggestions and assistance are greatly appreciated. Their efforts made this project possible and successful.

Sincere thanks to Connie Barry and everyone in the Ceramic Structural Group, especially Rosaura Ham-Su for their help and advice, Tom, Ed, Martin, John, Chris and Yosh for their technical assistance.

Thanks to friends in the Materials Department whom I met during my years at MAC, whom gave me academic and personal support, in particular Brian Reeves and Dwayne Wasylyshyn for proof-reading my thesis.

Last but not least, thanks to Anh for her constant motivation, support and love.

TABLE OF CONTENTS

LIST OF FIGURES

LIST OF TABLES

I. PROPERTIES OF MOLYBDENUM DISILICIDE AND THE COMBUSTION SYNTHESIS PROCESS

1.1 INTRODUCTION

At present, there are only a few materials capable of operating structurally above 1000°C, especially in oxidizing environment. Nickel-based and titanium-based superalloys have been used successfully up to about 1000°C, while ceramics such as silicon-based materials (SiC, Si_3N_4) and their composites are proposed to be the most suitable materials above 1000°C. However, utilization of the ceramics has been hindered by various factors such as their inherent brittleness over the entire operating temperature and the high cost and difficulties in their fabrication and machining (Vasudévan and Petrovic 1992). Therefore, other materials, including metal matrix composites, intermetallics and intermetallic matrix composites and ceramic matrix composites, are currently being researched and developed as the potential materials because of their superior high temperature mechanical properties and oxidation resistance.

There have been many studies on improving the mechanical properties of these materials. These include improvement of both fracture strength and toughness at both ambient and high temperature, by means of processing techniques and microstructural

modifications. The processing techniques will determine the overall homogeneity and purity of the materials, which will subsequently determine the critical flaw size and the defects in the final product. Microstructural modifications include controlling the grain size of the monolithic materials, introducing different types of reinforcements such as particulates, platelets, whiskers and fibres to toughen the composites, and controlling the orientation, size and shape of reinforcements.

This thesis involved all of the aspects mentioned above, namely, the study of materials processing by combustion synthesis, and the study of the resulting products, particularly silicide matrix composites. The objective of this study was to produce molybdenum disilicide composites reinforced with silicon carbide using combustion synthesis, and to study the mechanical properties of the product. In addition, the possibility of using the directionality of this synthesis process to induce whisker-like SiC particles was also studied. Following combustion synthesis, the materials were densified by hot-pressing. The final product was then characterized with respect to density, grain size and morphology of the reinforcement phase. Room temperature hardness, fracture strength, and toughness were measured. Fractography was done by means of scanning electron microscopy. Finally, the fracture mechanisms were studied in detail.

This chapter provides a background on molybdenum disilicide and the combustion synthesis process. Chapter 2 consists of a comprehensive literature review on combustion synthesis of molybdenum disilicide and its composites, fracture-initiating defects, toughening mechanisms, SiC reinforcement and mechanical property testing. Chapter 3 discusses the

processing of $MoSi_2$ and SiC-reinforced $MoSi_2$. Chapter 4 presents the experimental part of this thesis, results of the mechanical property testings and discussion of the results thereof. Finally, Chapter 5 summarizes the conclusions resulting from this work and suggests possible future work on the combustion synthesis process and on molybdenum disilicide composites.

1.2 MOLYBDENUM DISILICIDE MATRIX COMPOSITES

Tien *et al.*(1991) compiled and plotted the strength/density ratio vs temperature for metal alloys, ceramics and composites (Figure 1-1). In the high temperature regime with operating temperatures greater than 1000°C, several classes of suitable materials were identified. They included ceramic matrix composites, intermetallics and their composites, carbon-carbon matrix composites and silicide matrix composites. Among these classes, silicide matrix composites can offer a higher strength/density ratio, without decreasing the oxidation resistance.

Molybdenum disilicide ($MoSi_2$) is an intermetallic compound having mixture of Mo-Mo metallic bonding, Si-Si covalent bonding and Mo-Si ionic bonding. It has a body-centered tetragonal crystal structure. The lattice parameters are: a = 3.205 Å and c = 7.845 Å with c/a = 2.448 (Adler and Houska 1978). Figure 1-2 shows the tetragonal unit cell of $MoSi_2$ (Unal *et al.* 1990).

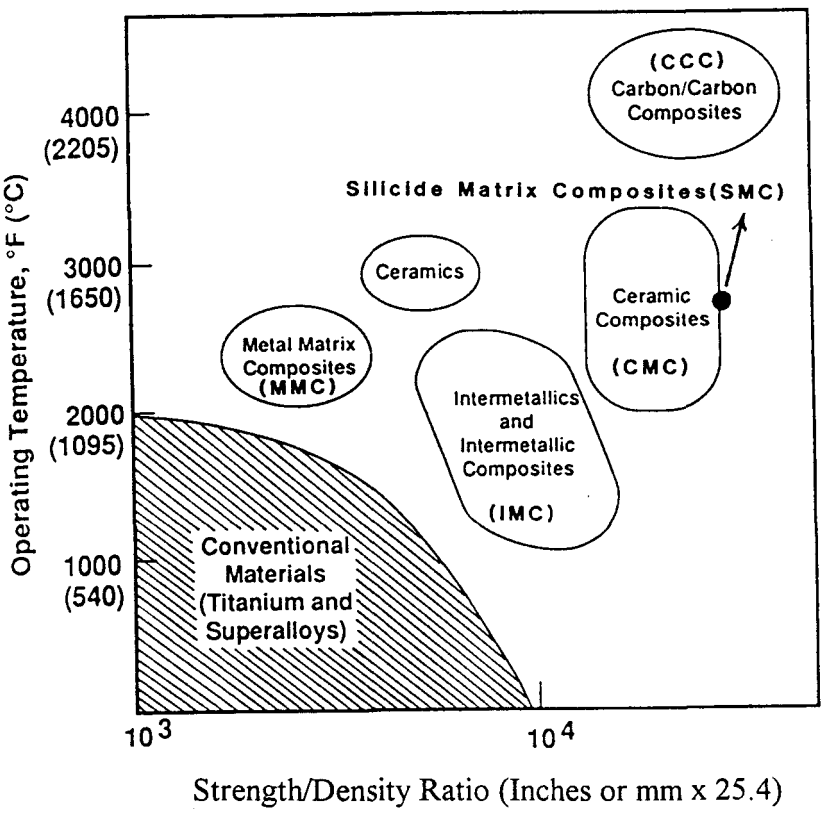

Figure 1-1: Strength/density ratio of several classes of high temperature structural materials as a function of the operating temperature (Tien *et al.* 1991).

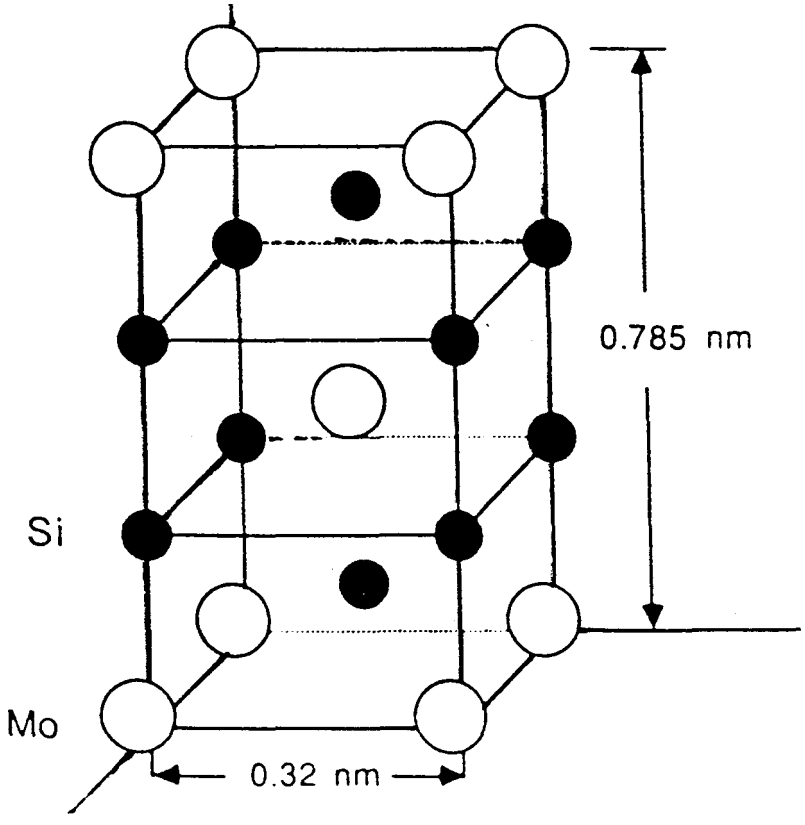

Figure 1-2: Tetragonal unit cell of $MoSi_2$ (Unal *et al.* 1990).

$MoSi_2$ has a relatively high melting point of 2030°C, a modest density of 6.24 g/cm^3 and high thermal conductivity. The latter is due to Mo-Mo metallic bonding. The high thermal conductivity enables electrodischarge machining of parts and is also beneficial to the cooling effectiveness of engine components. Another advantage is its high oxidation resistance up to 1600°C which is equivalent to that of silicon-based structural ceramics, such as Si_3N_4 and SiC. This is due to the formation of a protective glassy silica coating at service temperatures up to 1600°C. A comparison of some of the physical properties of various high temperature structural materials is found in Table 1-1.

Currently, $MoSi_2$ is being used in the heating elements of high temperature furnaces, consisting of 90% $MoSi_2$ and 10% metal of undisclosed composition. Other possible applications include: interconnects in microelectronic chips, oxidation resistance coating for metals, gas turbine engine components, thermoelectrodes, protective thermocouple sheaths, hot pressing and drawing dies and catalysts for the dehydrogenation of alcohol (Samsonov and Kislyi 1967; Scherg 1988; Matveiko and Khramtsov 1980; Samsonov and Vinitiskii 1980).

One problem with $MoSi_2$ is the oxidation near 500°C which can cause rapid disintegration (PEST phenomenon). PEST oxidation is due to the formation of needle-like MoO_3. This formation is accompanied by an increase in molar volume which can disintegrate the materials rapidly. At still higher temperatures, MoO_3 becomes volatile (Meschter and Schwartz 1989). Fortunately, PEST oxidation does not occur in specimens which are pore-free, crack-free (Berkowitz-Mattuck *et al.* 1970; Bartlett *et al.* 1965) and with density greater

Materials	Density ($g\ cm^{-3}$)	$T_{melting}$ (°C)	$T_{oxidation}$ (°C)	BDTT [a] (°C)	CTE [b] ($\times 10^{-6} K^{-1}$)
$MoSi_2$	6.30	2030	1600	1000	8.1
Ti_5Si_3	4.32	2130	?	?	?
FeAl	5.56	1337	1027	430	16.5
Fe_3Al	6.70	1540	?	550	16.5
NiAl	5.86	1647	1227	527	15
Ni_3Al	7.65	1390	?	700	12.5
TiAl	3.91	1462	827	700	11
Ti_3Al	4.20	1602	652	?	10
$TiAl_3$	3.30	1352	1027	527	13
$NbAl_3$	4.50	1577	1027	727	9
Nb_2Be_{17}	3.28	1702	?	>727	16
SiC Ceramic	3.18	2500	1600	NA	5
MAR M-246 [c]	8.44	1317	927	NA	16

?, data not available or not evaluated; NA, not applicable.

[a] BDTT -- brittle-to-ductile transition temperature
[b] CTE -- coefficient of thermal expansion
[c] MAR M-246 -- nickel-base superalloys

Table 1-1: Comparison of physical properties of various high temperature structural materials (Vasudévan and Petrovic 1992).

than 95 % of theoretical density (Lee *et al.* 1991; Chang 1969; Meschter *et al.* 1991).

Due to its body-centered tetragonal structure, $MoSi_2$ has only a few available slip systems, which limits its ductility at low temperature (Maloy *et al.* 1992). Maloy *et al.* (1991) also suggested that the formation of silica at the grain boundaries during the densification process at high temperature may further enhance its brittleness, hence $MoSi_2$ has a poor impact strength and low fracture toughness.

The mechanical properties of $MoSi_2$ change at the brittle-to-ductile transition temperature near 1000°C (Zeitsch *et al.* 1970; Fitzer *et al.* 1973; Schlichting 1978). Below this temperature $MoSi_2$ is brittle like a ceramic, and above this temperature it behaves like a metal, showing yielding and stress-relieving characteristics (Yang and Jeng 1991). At high temperatures, the silica content and the grain size determine the strength of $MoSi_2$, whose high-temperature strength and creep resistance are modest. At lower stress, the overall creep process is dominated by the grain boundary sliding process and at higher stress, it is the combined effects of grain boundary sliding and dislocation glide and climb mechanism (Sadananda *et al.* 1992; Wiederhorn *et al.* 1992).

The mechanical properties of $MoSi_2$ can be improved in several ways. The addition of 2 wt% carbon to $MoSi_2$ forms about 7 vol% SiC which increases the fracture toughness of $MoSi_2$ at high temperature (Maloy *et al.* 1991)(Figure 1-3). This improvement is due to the removal of the silica, the cause of low temperature brittleness and creep behavior due to grain boundary sliding, at the grain boundary by the deoxidation of carbon. Other means of improving the mechanical properties of $MoSi_2$ involve alloying it with other silicides or

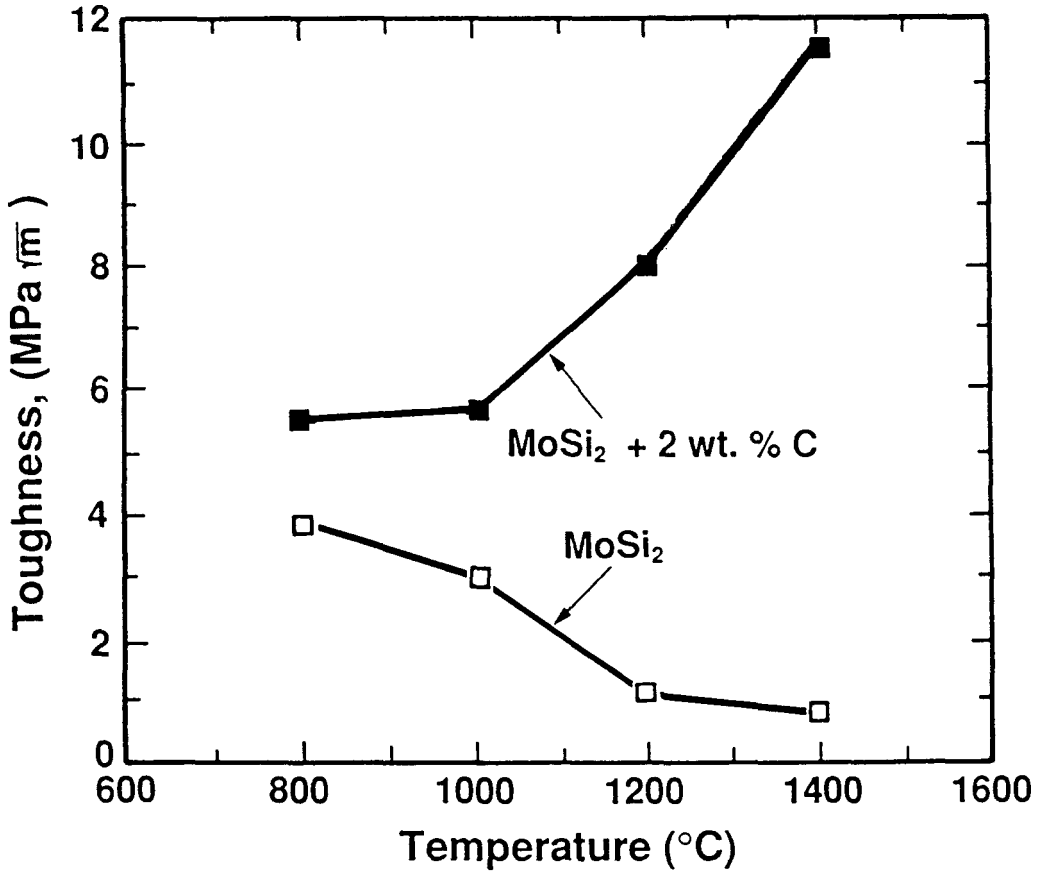

Figure 1-3: Temperature dependence of fracture toughness for pure and alloyed $MoSi_2$ (Maloy *et al.* 1991).

reinforcing it with compatible reinforcements. Vasudévan and Petrovic (1992) have shown that $MoSi_2$ is thermodynamically stable with many important ceramic reinforcements such as SiC and Al_2O_3 with 'no observable' interfacial reaction (Table 1-2). Table 1-3 contains a comprehensive summary of experimental work done to investigate the mechanical properties of $MoSi_2$ and its composites to date. The results show a room temperature toughness improvement of $MoSi_2$ with various reinforcements (Figure 1-4 and Table 1-4). Whisker reinforcement has generally shown the best improvement on the mechanical properties both at room and high temperature. However, whisker reinforcement is expensive, difficult to process and a health hazard.

Petrovic *et al.* (1990) and Sadananda *et al.* (1993) have successfully used both the alloying approach and the reinforcement approach to improve the high temperature mechanical properties of $MoSi_2$, but at the expense of increasing the density. Furthermore, at 1200°C, SiC reinforcement has been shown to reduce the creep rate of $MoSi_2$ (Sadananda *et al.* 1991) as shown by Figure 1-5. A review on the recent experiments on high temperature properties can be found in the literature by Petrovic (1995).

1.3 COMBUSTION SYNTHESIS

There are several processing techniques used to produce $MoSi_2$ and its composites, as listed in Table 1-3. The more conventional processing techniques for silicides are those

Matrix	Compatibility with the following reinforcement materials							
	SiC	Si_3N_4	Al_2O_3	TiC	TiB_2	ZrB_2	Y_2O_3	Nb
$MoSi_2$	C	C	C	C	C	C	C	R
$CoSi_2$	C	C	C	C	C	C?	C/WR	R
Cr_3Si	C	C	C	C	C	R	C	R
Ti_5Si_3	R	R?	C	C	C	R	C?	C
NiAl	C/WR	C/WR	C	C/WR	C/WR	C/WR	C/WR	R
Ni_3Al	R	R?	C	R	R	C/WR	C/WR	R
TiAl	R	R?	C/WR	R	C/WR	R	C/WR	R
Ti_3Al	R	R?	C/WR	R	R	R	C/WR	R
SiC	C	C	R	C	C	R	R	R

C, chemically compatible with no interfacial reactions; C/WR, chemically compatible with interfacial reactions; R, chemically unstable with the (a) formation of one or more interface reaction products, or (b) diffusion of one or more elements into the matrix; ?, possible estimates.

Table 1-2: Compatibility of reinforcements with intermetallic and ceramic matrices (Vasudévan and Petrovic 1992).

References.	Starting Powders (form*, micron, %purity)	Processing Technique **	Density (% of theoretical)	Grain Size (micron)	Fracture Toughness *** (MPa.m^1/2)	Modulus Of Rupture (4-POINT BEND TEST) (MPa)	Vickers Indentation Hardness (GPa)
Chen et al. 1995	Mo - 8, 99.5% Si - 70, 99 % SiC (w) - 0.33 (dia.) - 12 (length)	1) SHS - Mo + Si + 20 vol% SiC (w) 2) HP or HIP	MoSi2 (SHS + HP) - 99.1% MoSi2 (SHS + HIP) - 98.9% 20 vol% SiC/MoSi2 (SHS + HP) - 94.6% 20 vol% SiC/MoSi2 (SHS + HIP) - 95.8%	37 43 6.2 7.2	2.4 (IND, 25 oC), 3.8 (IND ST, 25 oC) 2.7 (IND, 25 oC), 4.2 (IND ST,25 oC) 3.7 (IND, 25 oC), 6.2 (IND ST, 25 oC) 4.8 (IND, 25 oC), 5.4 (IND ST, 25 oC)	170.7 (25 oC), 174.4 (1000 oC) 148.7 (25 oC), 204.3 (1000 oC) 171.8 (25 oC), 126.0 (1000 oC) 174.2 (25 oC), 154.7 (1000 oC)	9.9 (10 kg) 9.4 (10 kg) 13.5 (10 kg) 14.7 (10 kg)
Carter et al. 1989	MoSi2 - 400 mesh, 99.9% SiC (w,VLS) - 5 (dia) - 100-200 (length) - aspect ratio 20-30 :1 SiC (w,VS) - 0.1 (dia) - 1-5 (length) - aspect ratio 10 :1	HP - MoSi2 + 20 vol% SiC (w) - 1800 - 1900 oC, 5 min.	MoSi2 20 vol% SiC/MoSi2 (w, VLS) 20 vol% SiC/MoSi2 (w, VS)		5.32 (CNB, 25 oC) 6.59 (CNB, 25 oC) 8.2 (CNB, 25 oC)	~ 150 (25 oC), ~ 140 (1200 oC) ~ 300 (25 oC), ~ 400 (1200 oC) ~ 300 (25 oC), ~ 250 (1200 oC)	
Richardson et al. 1991	MoSi2 - 16, 99.5% MoSi2 - 8.6, 99.95% SiC (pl) - 17 (dia.) - 2.3(thick.) - aspect ratio 7-8 :1	HP - MoSi2 + 20 vol% SiC (pl) - 1700 oC, 34.5 MPa, 90 min.	20 vol% SiC/MoSi2 (pl, 99.5%) - 96.6% 20 vol% SiC/MoSi2 (pl, 99.95%) - 98.0%		7.5 (CNB, 25 oC), 6 (CNB, 1100 oC)	~ 220 (25 oC), ~ 340 (1100 oC) 297 (25 oC), ~ 220 (1100 oC)	
Tuffe et al. 1993	MoSi2 - 12, 99.5% Al2O3 (pl) - 10-15	HP - MoSi2 + 25 vol% Al2O3 - 1500 - 1600 oC, 46 MPa, 1 HR.	25 vol% Al2O3/MoSi2 - 88- 99%	10	4.9 (SENB, 25 oC)	340 (25 oC), ~ 280 (1000 oC) 270 (25 oC), ~ 490 (1000 oC)	
Bhattacharya et al. 1991	MoSi2 - 400 mesh SiC(p) - 0.5	HP - MoSi2 +20 vol% SiC(p) - 1850 oC, 30 MPa	MoSi2 - 93-96 % 20 vol% SiC/MoSi2 (p) - 93-96%	MoSi2 - 28 SiC - 5	2.85 (IND, 25 oC) 4.5 (IND, 25 oC)		~ 9.3 (5, 10, 20, 30, 40 kg) ~ 12.5 (5kg), 13 (10 kg), ~ 14 (20 kg), 16 (30 kg),
Alman et al. 1995	MoSi2 SiC (p) SiC (w)	HIP - MoSi2 (1350 oC, 172 MPa, 6 hr) HP - 30vol% SiC(p) (1800 oC, 30 MPa, 30 min) HP - 30vol% SiC(w) (1800 oC, 30 MPa, 30 min)	MoSi2 - 93 % 30 vol% SiC/MoSi2 (p) - 90% 30 vol% SiC/MoSi2 (w) - 94.7%				8.3 (10 kg) 16.1 (10 kg) 15.9 (10 kg)
Yang et al. 1990	MoSi2 - 325 mesh SiC(w) - 100 (dia.) SiC(f) - 150 (dia)	HP - MoSi2 (1700 oC, 35 MPa) HP - 20vol% SiC(w) (1700 oC, 35 MPa) HP - 20vol% SiC(f) (1700 oC, 200 MPa, 1 hr.)		MoSi2 - 25	6.37 (SENB, 25 oC)	224 (25 oC) 263 (25 oC)	
Gac et al. 1985	MoSi2 - 20 ---> 5 SiC (w, VLS) - 1-3 (dia.) - aspect ratio 20-40:1	HP - MoSi2 (1625 - 1640 oC, 41.4 MPa) HP - 20 vol%SiC(w)/MoSi2 (1625 - 1640 oC, 41.4 MPa)	MoSi2 - 95.3% -97.5% 20 vol% SiC/MoSi2 (w) - >95.2%	MoSi2 - 30	5.32 (CNB, 25 oC) 8.20 (CNB, 25 oC)	140-160 (25 oC) 310 (25 oC)	
Wade et al. 1992	MoSi2 - 400 mesh, 99.9%	HP - MoSi2 (1820 oC, 32 MPa, 15 min.)	MoSi2 - >97%	MoSi2 - 18 SiO2 - 1-3 (in MoSi2) - 5-8(at G.B.)	3.0 (IND - 1,5,10,20,30 kg, 25 oC)		8.7 (1,5,10,20,30 kg)
Wade et al. 1992	MoSi2 - 400 mesh, 99.9%	HP - MoSi2 (1500 oC, 32 MPa, 15 min.) HP - MoSi2 (1600 oC, 32 MPa, 15 min.) HP - MoSi2 (1700 oC, 32 MPa, 15 min.) HP - MoSi2 (1800 oC, 32 MPa, 15 min.) HP - MoSi2 (1880 oC, 32 MPa, 15 min.) HP - MoSi2 (1920 oC, 32 MPa, 15 min.)		MoSi2 - 13.5 MoSi2 - 15.3 MoSi2 - 18.4 MoSi2 - 20.5 MoSi2 - 22.2 MoSi2 - 31.9	3.0 (IND - 10 kg, 25 oC) 3.6 (IND - 10 kg, 25 oC) 2.7 (IND - 10 kg, 25 oC) 3.0 (IND - 10 kg, 25 oC) 2.9 (IND - 10 kg, 25 oC) 2.3 (IND - 10 kg, 25 oC)		9.73 (10 kg) 9.87 (10 kg) 9.07 (10 kg) 9.08 (10 kg) 9.12 (10 kg) 8.92 (10 kg)

Table 1-3: A comprehensive summary of experimental works done to investigate the mechanical properties of MoSi2 and its composites

References.	Starting Powders (form*, micron, %purity)	Processing Technique **	Density (% of theor.)	Grain Size (micron)	Fracture Toughness *** (MPa.m^1/2)	Modulus Of Rupture (4-POINT BEND TEST) (MPa)	Vickers Indentation Hardness (GPa)
Gibbs et al. 1987	MoSi2 SiC (w,VLS)	HP - MoSi2 (1500 oC) HP - 20 vol% SiC(w)/MoSi2 (1500 oC)	MoSi2 - 98%	MoSi - 8-10	4.38 (CNB, 25 oC) 5.68 (CNB, 25 oC)	173 (25 oC), 120 (1200 oC) 331 (25 oC), 240 (1200 oC)	
etrovic et al. 1990	MoSi2/WSi2 - 400 mesh SiC(w, VS) SiC(w, VLS) SiC (p)	HP - MoSi2/WSi2 (1800 oC, 30 MPa) HP - 20 vol% SiC(w,VS)/MoSi2 (1900 oC, 30 MPa) HP - 20 vol% SiC(w,VLS)/MoSi2 (1900 oC, 30 MPa) HP - 20 vol% SiC(p)/MoSi2 (1900 oC, 30 MPa)	93-96%			140 (1200 oC) MoSi2 - 140 (1200oC) 20 vol% SiC (w, VS)/MoSi2 - 400 (1200 oC) 20 vol% SiC (w, VSL)/(Mo,W)Si2 - 300 (1200 oC) 20 vol% SiC (w, VS)/(Mo,W)Si2 - 600 (1200 oC) 20 vol% SiC (p)/(Mo,W)Si2 - 450 (1200 oC)	
etrovic et al. 1990	MoSi2 - 400 mesh PSZ - 5	HP - MoSi2 (1700 oC, 30 MPa) HP - 30 vol% PSZ/MoSi2 (1700 oC, 30 MPa)	96 %	MoSi2 - 15 PSZ - 20	2.58 (IND, 10 kg, 25 oC) 6.56 (IND, 10 kg, 25 oC)		10.00 (10 kg) 8.49 (10 kg)
Maloy et al. 1991	MoSi2 - 400 mesh 2 wt% C - 325 mesh	HP - MoSi2 (1830 oC, 50 min.) HP - 2 wt%C/MoSi2 (1830 oC, 50 min.)		MoSi2 - 15 2wt%C/MoSi2 - 20	4 (SENB, 800 oC) 5.5 (SENB, 800 oC)		900 kg/mm2 (1kg, 1300 oC) 1300 kg/mm2 (1kg, 1300 oC)
Shankar et al. 1994	Mo - 3-7, 99.9% Si - 325 mesh, 98% C - 300 mesh, 99.5% MoSi2 - 325 mesh, 99.9 % SiC - <1, 99.9 %	MA + HP (1650 oC, 35-40 MPa, 1 hr.) HP (1600 oC, 35 MPa, 1 hr.)	>99%		20 vol%SiC/MoSi2 - 3.5 (IND, 10-20 kg, 25 oC) 40 vol%SiC/MoSi2 - 4.5 (IND, 10-20 kg, 25 oC) 20 vol%SiC/MoSi2 - 4.25 (IND, 10-20 kg, 25 oC) 40 vol%SiC/MoSi2 - 4.5 (IND, 10-20 kg, 25 oC)		MoSi2 - 8.56 (10-20 kg) 20vol%SiC/MoSi2 - 12.70 (10-20 k 40vol%SiC/MoSi2 - 14.50 (10-20 k MoSi2 - 8.56 (10-20 kg) 20vol%SiC/MoSi2 - 12.50 (10-20 k 40vol%SiC/MoSi2 - 13.50 (10-20 k
Shankar et al. 1994	MoSi2 - 5-45 SiC - ?	VACUUM PLASMA SPRAY	>98%		MoSi2 (VPS)- 4.7 (IND, 25 oC) MoSi2 (HP) - 2.9 (IND, 25 oC) 4 vol%SiC/MoSi2 - 5.4 (IND., 25 oC) 20 vol%TiB2/MoSi2 - 6.1 (IND., 25 oC)	MoSi2 (VPS)- 280 (25 oC) MoSi2 (HP) - 185 (25 oC) 4 vol%SiC/MoSi2 - 300 (25 oC) 20 vol%TiB2/MoSi2 - 380 (25 oC)	MoSi2 (VPS)- 1200 kg/mm2 MoSi2 (HP) - 950 kg/mm2 4 vol%SiC/MoSi2 - 1228 kg/mm2 20 vol%TiB2/MoSi2 - 1057 kg/mm2
trovic et al. 1991	MoSi2 - 400 mesh ZrO2 - 3	HP (1700 oC, 32 MPa)	94-95%		MoSi2 - 2.6 (IND, 25 oC) 20 vol%PSZ (2.5mole% Y2O3) - 4 (IND,25 oC) 20 vol%ZrO2 (0 mole% Y2O3) - 7.8 (IND,25 oC)		

* p = Particulate
pl = Platelet
w = Whisker (VS -- Produced by Vapour-Solid Process, VLS -- Produced by Vapour-Liquid-Solid Process)

** MA = Mechanical Alloying
SHS = Self-Propagating High Temperature Synthesis (Combustion Synthesis)
HP = Hot Pressing
HIP = Hot Isostatic Pressing
VPS = Vacuum Plasma Spray

*** IND = Indentation Method
IND ST = Indentation + Bend Method
CNB = Chevron Notched Bar
SENB = Single Edge Notch Beam

Table 1-3: A comprehensive summary of experimental work done to investigate the mechanical properties of $MoSi_2$ and its composites (continued).

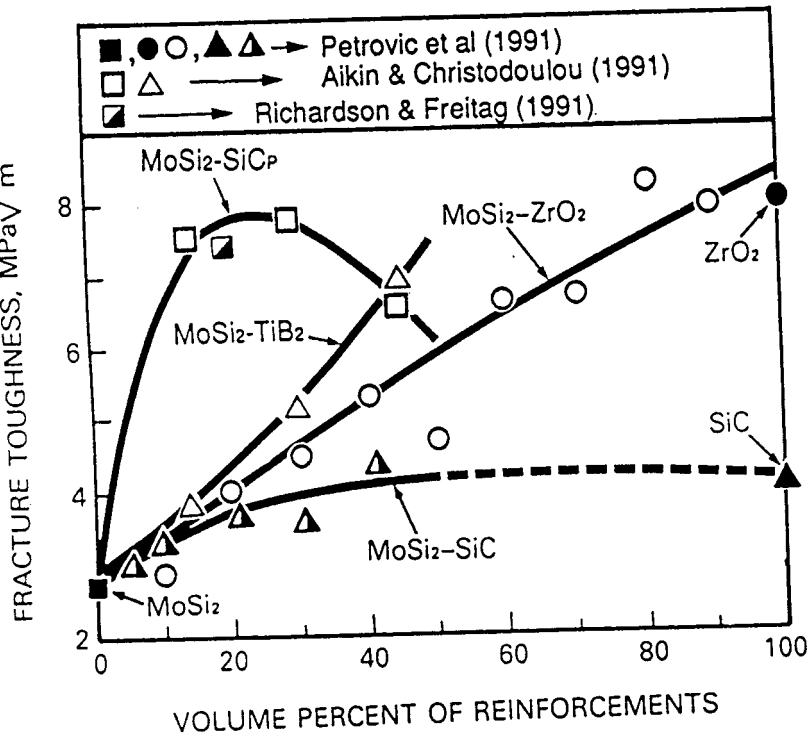

Figure 1-4: Room temperature fracture toughness improvements in $MoSi_2$ (Vasudévan and Petrovic 1992).

Type of Reinforcement	Highest Fracture Toughness ($MPa.m^{1/2}$)
Refractory metal (Nb, W, Mo) Wires	>15
20 vol% Ta Particles	10
20 vol% ZrO_2 Particles	7.8
20 vol% SiC Whiskers	4.4
20 vol% SiC Particles	4.0
Polycrystalline $MoSi_2$	3

Table 1-4: Room-temperature fracture toughness of $MoSi_2$-based composites (Petrovic 1995).

a)

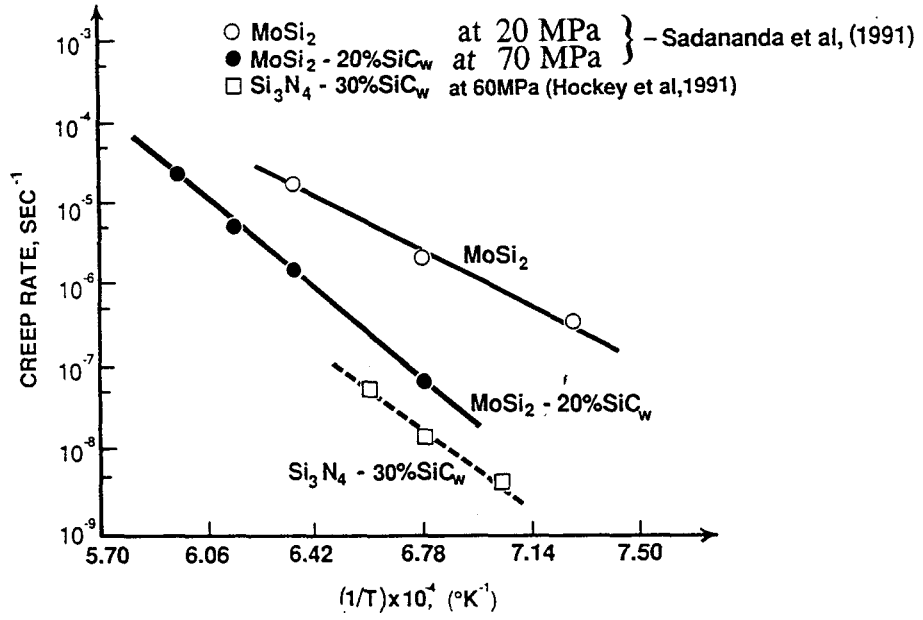

b)

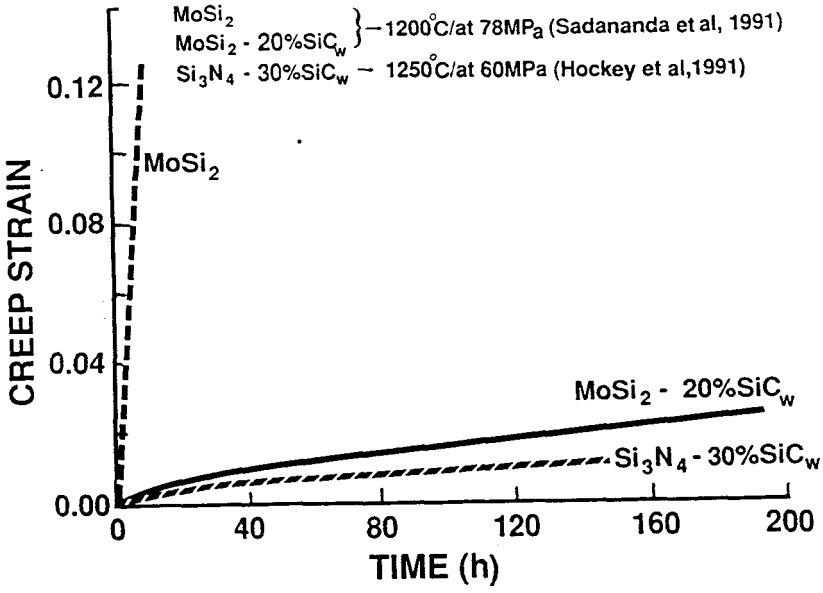

Figure 1-5: Comparison of creep deformation of $MoSi_2$ and its composites: a) creep rate vs temperature and b) creep strain vs time (Sadananda *et al.* 1991).

employed for ceramics. The procedure is to obtain the precursor materials in powder form, mix and disperse the powders, consolidate into a green body with the final shape and densify at an elevated temperature (Lange 1989). For each step, various techniques can be used as shown in Table 1-5. In addition, more novel techniques have been developed and proven successful in producing these composites. These include mechanical alloying (MA) by high energy ball milling (Patankar *et al.* 1993; Jayashankar and Kaufman 1993; Ma *et al.* 1993; Schwarz *et al.* 1992), injection molding (Alman *et al.* 1992), plasma-spraying (Alman *et al.* 1992; Tiwari *et al.* 1992; Jayashankar *et al.* 1994), vapor infiltration (Patibandla and Hillig 1993), in-situ exothermic dispersion or XD™ process (Aikin 1991; Suzuki *et al.* 1993) and combustion synthesis (Subrahmanyam *et al.* 1994, 1995; Govindarajan *et al.* 1994; Deevi 1991, 1994; Gedevanishvili 1994). Of the publications available on combustion synthesis, none discusses the mechanical behavior of the product.

Combustion synthesis is a processing technique pioneered by Merzhanov and his co-workers in the former Soviet Union during the 1970's (Khaikin and Mershanov 1966; Mershanov and Borovinskaya 1972, 1975). Since then, this technique has been used to produce many advanced high temperature materials such as ceramics, intermetallics and their composites. Table 1-6 shows some of these materials and their respective calculated adiabatic temperatures during synthesis.

The basis of the combustion synthesis process is to utilize the self-sustaining exothermic reaction between these powders to yield the final product without additional heat, in the form of a reaction (combustion) wave. There are two modes to the combustion

Procedure	Options
1) Precursor Materials	Elemental powders Compounds Reinforcements (Platelets, Particulates, Fibres, Whiskers)
2) Mixing and Dispersing	Dry State: Dry Ball Milling Wet State: Wet Ball Milling Colloidal Processing
3) Consolidation	Slurry Casting: Slip Casting Tape Casting Electrophoretic Deposition Cold Pressing
4) Densification	Pressing: Hot Pressing Hot Isostatic Pressing Sintering Reaction Sintering

Table 1-5: Steps in the processing technique for fabricating silicide/ceramic composites.

Materials	Combustion Synthesized Materials and Their Calculated Adiabatic Temperatures in Kelvin
Borides	TiB_2 (3190), ZrB_2 (3310), NbB_2 (2400), TaB_2 (3370), MoB_2 (1800), LaB_6 (2800), HfB_2 (3520), CrB, VB, TiB (3350)
Carbides	TiC (3210), HfC (3900), B_4C (1000), Al_4C_3 (1200), TaC (2700), SiC (1800), WC (1000), ZrC (3400), NbC (2800), Cr_3C_2, Ta_2C (2600)
Carbonitrides	TiC-TiN, NbC-NbN, TaC-TaN
Nitrides	TiN (4900), ZrN (4900), BN (3700), AlN (2900), Si_3N_4 (4300), TaN (3360), HfN (5100), NbN
Silicides	$MoSi_2$ (1900), Ti_5Si_3 (2500), Zr_5Si_3 (2800), Nb_5Si_3 (3340), $NbSi_2$ (1900), $TaSi_2$ (1800), $ZrSi_2$ (2100), WSi_2 (1500), V_5Si_3 (2260), TiSi (2000)
Hydrides	TiH_2, ZrH_2, NbH_2
Intermetallics	NiAl (1910), FeAl, N_6Ge, TiNi, CoTi, CuAl, CoAl (1900)
Chalcogenides	MoS_2, $TaSe_2$, NbS_2, WSe_2
Cemented Carbides	TiC-Ni, TiC-(Ni, Mo), WC-Co, Cr_3C_2-(Ni, Mo)
Composites	TiC-TiB_2, TiB_2-Al_2O_3, B_4C-Al_2O_3, TiN-Al_2O_3, $MoSi_2$+Al_2O_3 (3300), $MoSi_2$+SiC, MoB+Al_2O_3 (4000), Cr_2C_3+Al_2O_3 (6500), 6VN+5Al_2O_3 (4800), TiC+Al_2O_3 (2300), TiAl+TiB_2

Table 1-6: Combustion synthesized materials and their calculated adiabatic temperatures in Kelvin.

synthesis: self-propagating high temperature synthesis mode (SHS) and thermal explosion mode/combustion mode.

In SHS mode, the reaction is initiated locally at one end of the sample with the aid of a localized heat pulse and propagates through the free-standing pelletized mixture's volume in the form of a combustion wave, leaving behind the condensed product of combustion as shown in Figure 1-6. This mode is generally used for producing materials with adiabatic temperatures higher than 2000 K, for example, refractory materials such as TiC and Si_3N_4. In thermal explosion mode, the whole sample is heated uniformly to the ignition temperature whereupon the reaction takes place simultaneously throughout the volume. This mode is used to produce materials with adiabatic temperature lower than 2000 K, in which if SHS mode is used, the ignition temperature is so high that it requires pre-heating before ignition. These systems include intermetallics such as TiAl and NiAl. Figure 1-7 shows a typical temperature-time relationship for the thermal explosion mode of combustion synthesis (Yi and Moore 1990).

Compared to other conventional powder processing techniques such as sintering, hot pressing and hot-isostatic-pressing (HIP), combustion synthesis is an attractive, practical and viable alternative. General advantages include (Munir and Anselmi-Tamburini 1989; Deevi 1994):

1) Simplicity of the process with an easy experimental configuration and low energy/temperature requirement;

2) Short time requirement due to the extremely high speed of the propagating wave front

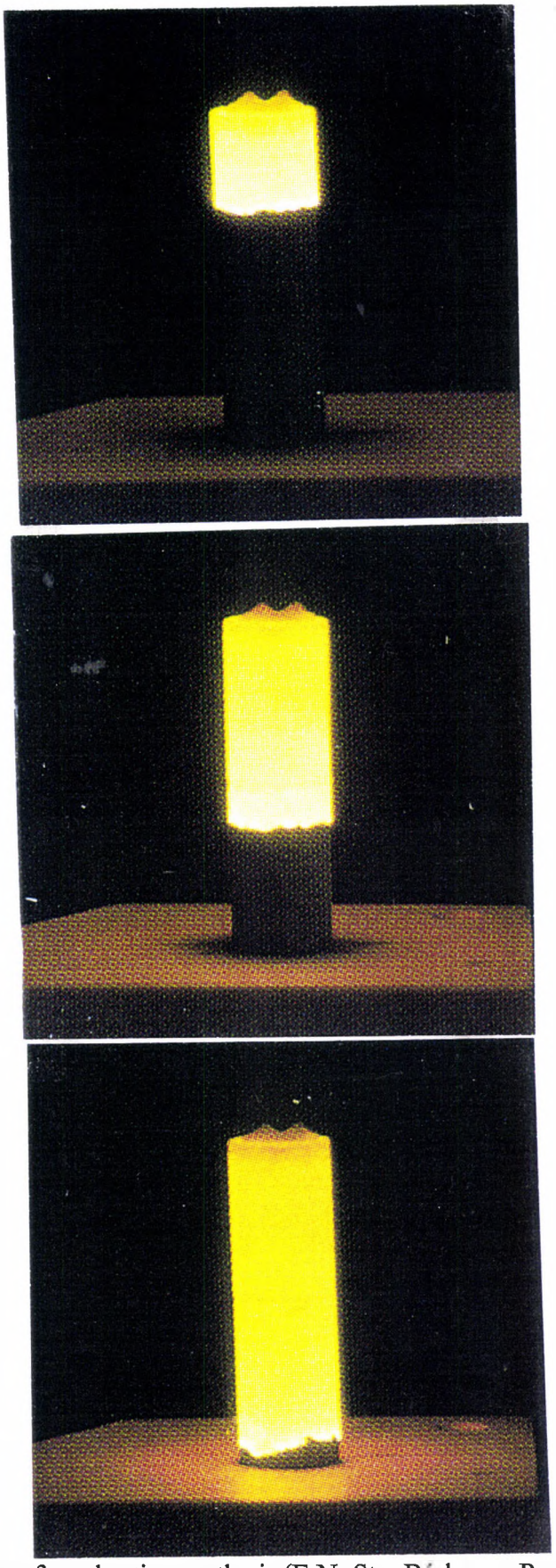

Figure 1-6: SHS mode of combustion synthesis (E.N. Sta. Bárbara - Paracuellos del Jarama).

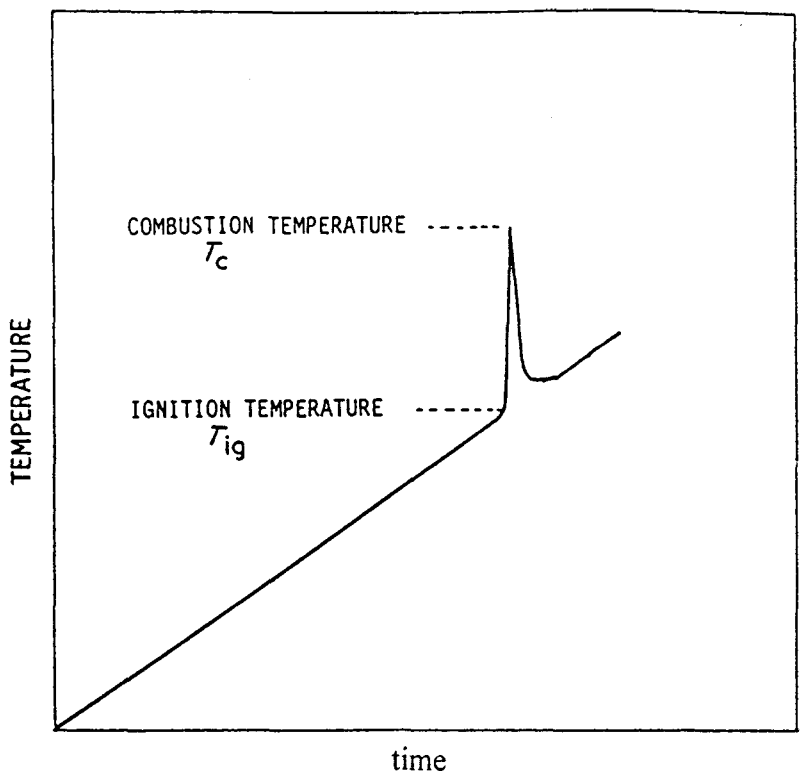

Figure 1-7: A typical temperature-time relationship for the thermal explosion mode of combustion synthesis (Yi and Moore 1990).

which can reach as high as 25 cm/s;

3) A better control of the final product in terms of grain size and purity. Conventional techniques involve processing of the commercially available compounds in which the size and purity are limited. Combustion synthesis processes involves producing compounds from the elemental powders, therefore, the final products can be engineered by controlling the powder sizes and the purity of the elemental powders;

4) Ability to produce high purity products, since the extremely high temperature of the combustion wave may expel the volatile impurities. In most systems, the products are purer than the reactants (Deevi 1991);

5) Ability to produce near-net shape and metastable phase materials, due to the high thermal gradient and high cooling rate during the process;

6) Ability to produce monolithic materials with uniform grains and composites with homogeneous distribution of reinforcements, due to the in-situ reaction of combustion synthesis; and,

7) Ability to predict and control structural defects associated with the processing and manufacturing of complex shapes.

However, one drawback to this method is the porosity of the final product, which can vary from 30% to 60% of the theoretical density. Rice (1985) distinguished the porosity into two categories: extrinsic and intrinsic. Extrinsic porosity is due to a) the porosity of the green compact being carried over to the final product due to the lack of external forces to cause shrinkage; b) diffusion of one component across a boundary into another component resulting

in porosity and a large skeletal structure; c) by-product gases and out-gassing of volatile components (both adsorbed and absorbed gases) which can expand within the closed pores. Intrinsic porosity is due to the molar volume difference between the reactants and the products.

To densify these materials, numerous methods of external pressure applications have been utilized. These include hot pressing (Holt and Munir 1986; Holt 1987; Richardson *et al.* 1986), shock wave consolidation (Holt 1987; Kecskes *et al.* 1990), hot isostatic pressing and high pressure self-combustion sintering (Miyamoto *et al.* 1984; Yamada *et al.* 1985; Adachi *et al.* 1989; Adachi 1990; Miyamoto 1990) and hot rolling (Rice *et al.* 1986; Rice 1990).

1.3.1 THERMODYNAMIC CONSIDERATION

The viability of combustion synthesis depends on the enthalpy of the reaction. With a high enthalpy change for an exothermic reaction, the combustion will occur and self-propagate, but with a low enthalpy change, there will be no combustion. This heat of chemical reaction raises the temperature of the product of combustion, until the maximum temperature is attained. With a highly exothermic reaction, this temperature can be achieved in a very short time. Therefore, it is reasonable to treat this as a thermally isolated exothermic system because there is very little time for the heat to disperse to its surroundings and this

maximum temperature is assumed to be the adiabatic temperature, T_{ad} (Yi and Moore 1990). In addition, it is assumed that the reaction goes to completion. Thus, T_{ad} is a good indicator of the exothermicity of the reaction. It defines the upper limit for any combustion system (Subrahmanyam and Vijayakumar 1992), since a total adiabatic condition is very difficult to achieve. Table 1-7 shows a comparison of calculated and experimental combustion temperatures in SHS studies (Merzhanov 1990).

Theoretically, the adiabatic temperature can be calculated from the heat balance condition (Subrahmanyam *et al.* 1989, Holt and Munir 1986, Novikov *et al.* 1975);

$$\Delta H^{o}_{T_{ad}} = \Delta H^{o}_{T_o} + \int_{T_o}^{T_{ad}} \Delta C_p dT \qquad (1)$$

where ΔH^{o}_{To} , ΔH^{o}_{Tad} are the standard enthalpies of formation at the initial temperature, T_o, and at the adiabatic temperature, T_{ad}, respectively. ΔC_p is the change in heat capacity between reactants and products. A schematic representation of the calculation is shown in Figure 1-8. In SHS mode, the initial temperature is the temperature of the reactants before ignition. Moreover, the effect of the heating rate in the combustion mode is generally considered equivalent to the effect of initial temperature in SHS mode.

For a thermally isolated (adiabatic) system, $\Delta H^{o}_{Tad} = 0$, hence,

Reaction	T_{ad} (calculated) (K)	T_{ad} (experimental) (K)
$Ni + Al \rightarrow NiAl$	1910	1910
$Co + Al \rightarrow CoAl$	1900	1880
$Ti + Si \rightarrow TiSi$	2000	1850
$Ti + 2Si \rightarrow TiSi_2$	1800	1770
$Nb + 2Si \rightarrow NbSi_2$	1900	1880
$Mo + 2Si \rightarrow MoSi_2$	1900	1920
$5Ti + 3Si \rightarrow Ti_5Si_3$	2500	2350
$Si + C \rightarrow SiC$	1800	1953
$Nb + C \rightarrow NbC$	2800	2650
$2Ta + C \rightarrow Ta_2C$	2600	2550

Table 1-7: Comparison of calculated and experimental combustion temperature in SHS system (Merzhanov 1990).

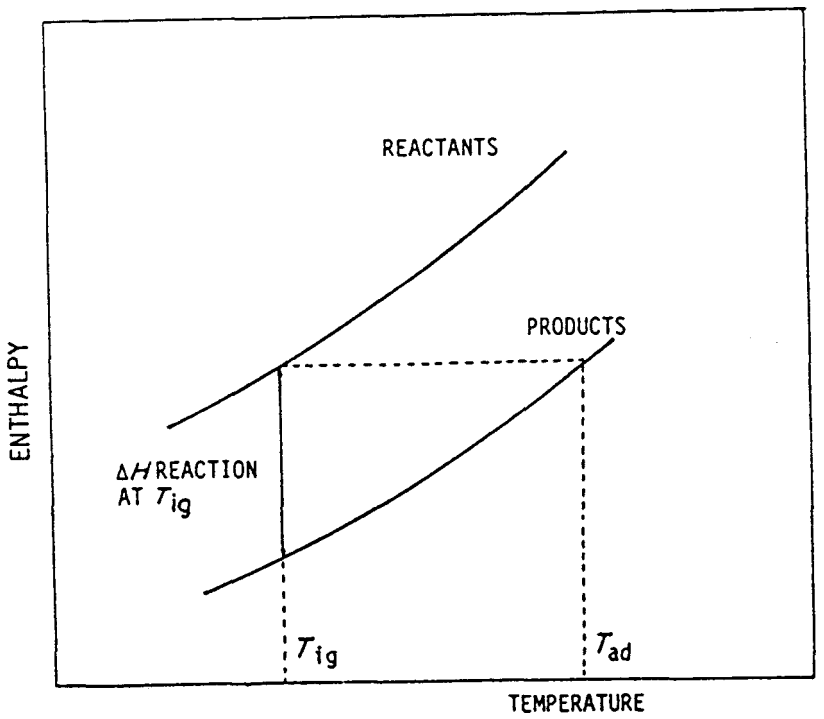

T_{ig} -- ignition temperature

T_{ad} -- adiabatic temperature

Figure 1-8: A diagrammatic representation of the calculation of the adiabatic temperature (T_{ad}) (Yi and Moore 1990).

$$-\Delta H^{o}_{T_o} = \int_{T_o}^{T_{ad}} \Delta C_p dT \qquad (2)$$

With this equation, the adiabatic temperature of the reaction can be calculated when the required thermodynamic data are available (Barin *et al.* 1977). Enthalpies of formation (or reaction) are commonly tabulated at 298 K, hence adiabatic temperatures of those listed in Table 1-6 are calculated on the basis of T_o = 298 K. Also, the adiabatic temperature can be calculated from any thermodynamics software such as F*A*C*T (Facility for the Analysis of Chemical Thermodynamics).

The adiabatic temperature allows one to determine the suitability of intermetallic systems for combustion synthesis. Merzhanov (1975) has suggested that combustion will not occur if T_{ad}< 1800 K, and will only be self-sustaining if T_{ad} > 2500 K. For 1800 K < T_{ad} < 2500 K, the system requires an external heat source such as preheating the precursors or by putting them inside another highly exothermic reactant mixture termed a "chemical oven" by Yi and Moore (1990).

1.3.2 KINETICS CONSIDERATION

The process modeling of combustion synthesis is very complicated in view of the heterogeneous systems and multidimensional unsteady state heat and mass transfer problem,

involving moving boundaries (Khaikin *et al.* 1966, 1975; Morgolis *et al.* 1990). Previous process modeling is based on the utilization of Fourier's one-dimensional heat conduction equation with a heat source. A simple form of this equation is (Munir and Anselmi-Tamburni 1989);

$$C_p\rho\left(\frac{\partial T}{\partial t}\right)=k\left(\frac{\partial^2 T}{\partial x^2}\right)+q\rho\left(\frac{\partial f(\eta)}{\partial t}\right) \qquad (3)$$

where C_p is the specific heat capacity of the product ($J\cdot kg^{-1}\cdot K^{-1}$), ρ is the density of the product ($kg\cdot m^{-3}$), k is the thermal conductivity of the product ($J\cdot m^{-1}\cdot K^{-1}\cdot s^{-1}$), q is the heat of reaction ($J\cdot kg^{-1}$), T is the absolute temperature (K), t is the time (s), x is the dimension along which the wave is propagating (m), and ($\partial f(\eta) / \partial t$) is the reaction rate ($s^{-1}$).

To solve for the velocity of the propagation from the above equation, a function of the temperature profile and the kinetics of the reaction are required. The former can be approximated experimentally or calculated through various models (Dunmead *et al.* 1992; Lakshmikantha and Sekhar 1993; Feng and Munir 1995). As for the latter, two general approaches have been used to solve the differential equation: 1) Arrhenius (chemical) kinetics and 2) diffusion kinetics.

By using the Arrhenius kinetic approach, the following velocity equation was derived (Maksimov and Shkadinskii 1971; Novozhilov 1960, 1962; Khaikin and Merzhanov 1966);

$$v^2=f(n)\left(\frac{C_p k}{q}\right)\left(\frac{RT_c^2}{E^*}\right)K_o\exp\left(\frac{-E^*}{RT_c}\right) \qquad (4)$$

where v is the velocity of the propagation of combustion ($m\cdot s^{-1}$), f(n) is a function of kinetic order, n, of reaction, T_c is the combustion temperature (adiabatic temperature)(K), R is the gas constant ($J\cdot mol^{-1}\cdot K^{-1}$), K_o is a constant, E^* is the activation energy ($J\cdot mol^{-1}$), and all other symbols are as defined previously.

By using the diffusion kinetics approach, the following velocity equation is obtained (Hardt and Phung 1973):

$$v^2=\left(\frac{2K}{d^2 C_p \rho S}\right)D_o\exp\left(\frac{-E^*}{RT_c}\right) \qquad (5)$$

where d is the particles size of one the reactants (m), S is the stoichiometric ratio of the reactants, D_o is the diffusion coefficient pre-exponent ($m^2\cdot sec^{-1}$), K is a constant, and all other symbols are as defined previously.

Considerable work has also been done in the former Soviet Union and the United States to analytically solve these equations. However, thus far, the success of these models in predicting the velocities of the propagating wave is very limited. In some cases, the predicted and measured velocities can be different by more than an order of magnitude (Hardt and Phung 1973). This discrepancy occurs because combustion synthesis involves both

chemical and diffusion kinetics and in these models, the effects of porosity on the parameters are not considered. Further complications arise since thermodynamic data, diffusion coefficients, activation energies, etc., are not available in the literature for very complex systems. To date, these models have only been used successfully to calculate the activation energy of some simple systems such as Ti + C (Holt and Munir 1986).

1.3.3 FACTORS INFLUENCING COMBUSTION SYNTHESIS

There are various factors that affect the propagating rate of the combustion front and the adiabatic temperature, and hence the quality of the product, which modeling is not able to correlate. These factors are a) stoichiometric ratio, b) pre-heat temperature, c) particle size, d) amount of diluent, e) specimen diameter and f) green density (Frankhouser *et al.* 1985; Yi and Moore 1990). These are briefly discussed below:

a) Stoichiometric ratio: any deviation from stoichiometric ratio reduces the adiabatic temperature, hence the velocity of combustion front (Figure 1-9a);

b) Pre-heating temperature: combustion rate will increase with increased pre-heat temperature because less heat is required to ignite the reaction (Figure 1-9b);

c) Particle size: particle size will influence the dispersion and the effective contact area of the reactant, hence the kinetics of solid state reaction. Thus, the combustion rate will increase with decreasing diameter of particles (Figure 1-9c);

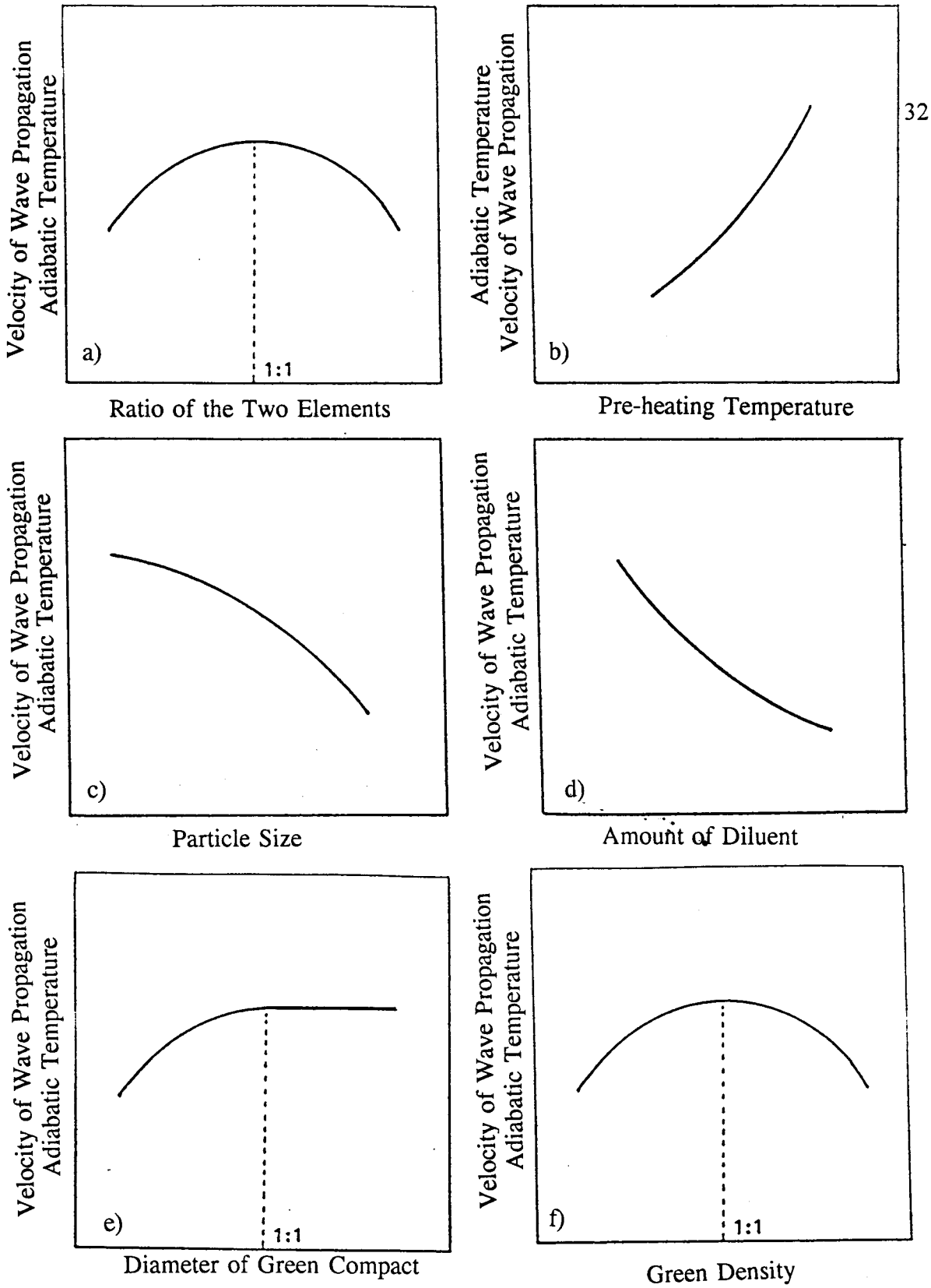

Figure 1-9: Effect of a) stoichiometric ratio, b) pre-heat temperature, c) particle size, d) amount of diluent, e) specimen diameter, and f) green density on propagation rate and combustion temperature (Frankhouser *et al.* 1985; Yi and Moore 1990).

d) Amount of diluent: diluent in the sample will be a heat sink as the combustion front passes through, hence slowing the propagation rate (Figure 1- 9d);

e) Specimen diameter: combustion rate increases with the specimen diameter and remains constant after reaching a threshold value. This threshold value will depend on the system. A small diameter will decrease the combustion rate due to the high radial heat losses (Figure 1-9e); and,

f) Green density: green density will affect the thermal conductivity and the specific heat of the green compact. With low green density, the heat of combustion will not be able to transfer effectively, hence may slow down or even cause extinction of the reaction. On the other hand, with high green density, the rapid heat transfer will lead to greater heat loss from the sample so that a complete conversion to the final product is not achieved (Figure 1-9f).

II. LITERATURE REVIEW

2.1 COMBUSTION SYNTHESIS OF $MoSi_2$ AND SiC-REINFORCED $MoSi_2$

Bhattacharya (1991) developed a model in terms of temperature-enthalpy relationships to simulate the self-propagating high temperature synthesis of $MoSi_2$ and SiC-$MoSi_2$ composites. Although this model was able to predict the relationship between the combustion wave velocity and other parameters such as green porosity and amount of SiC-reinforcement, the sources of the thermophysical properties were not mentioned and were questionable.

By using the SHS mode and varying the initial temperature, Zhang and Munir (1991) were able to measure different propagating wave velocities. The results are summarized in Table 2-1. Based on the Arrhenius kinetic model equation (4) introduced in Section 1.3.2, they calculated the activation energy by plotting an Arrhenius plot as seen in Figure 2-1. This value was calculated to be 139.4 kJ/mole, compared to 167.2 kJ/mole (Bloshenko *et al.* 1985) also measured for combustion synthesis, 183.9 kJ/mole (Brewer *et al.* 1980) measured for the diffusion of Si into Mo and 240.8 kJ/mole (Ivanov *et al.* 1967) measured for the reactive diffusion of Si into $MoSi_2$. The lower activation energy measured for combustion synthesis was attributed to the high point defect concentration at the reaction front which occur in high thermal gradient systems like combustion synthesis, contributing to the

T_o (K)	T_{ad} (K)	T_c (K)	Velocity (mm/s)
298	1913	1615	1.30
373	1961	1798	2.09
473	2029	1884	2.81
573	2099	1974	3.05
673	2173	2046	5.84

T_o -- initial temperature
T_{ad} -- adiabatic temperature
T_c -- combustion temperature

Table 2-1: Effect of preheating on the combustion temperature and wave velocity for $MoSi_2$ (Zhang and Munir 1991).

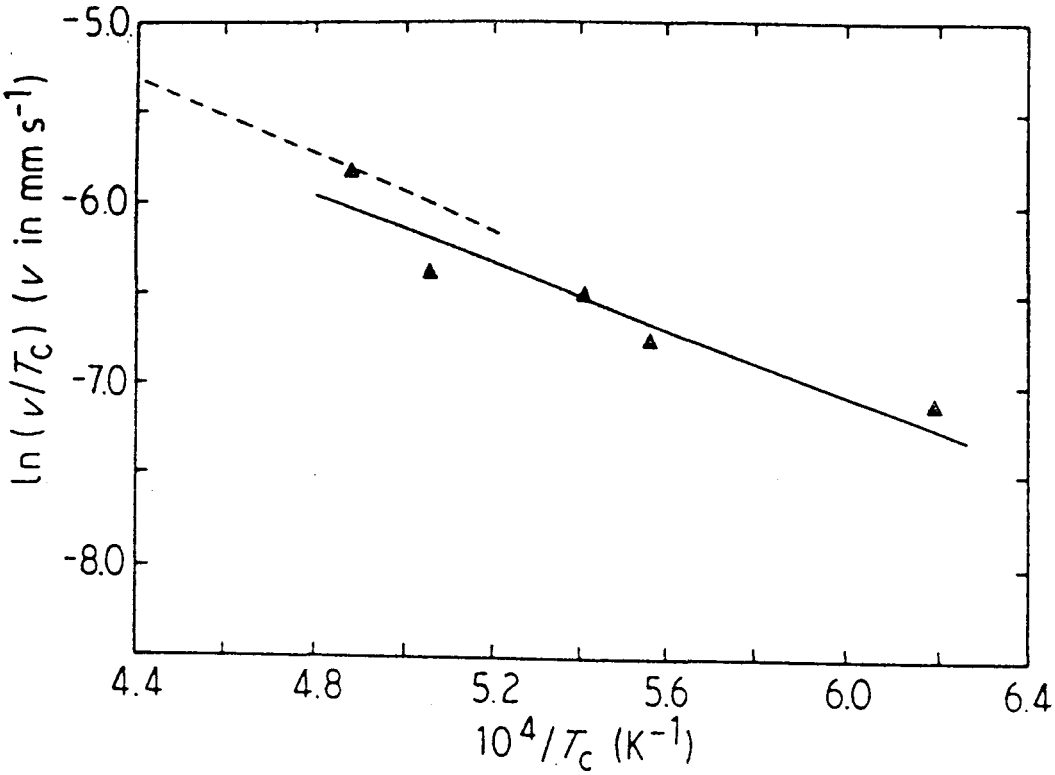

Figure 2-1: The temperature dependence of the wave velocity in the synthesis of $MoSi_2$ and the corresponding activation energy (▲Zhang and Munir 1991; ------Bloshenko *et al.* 1985).

enhancement of vacancy-assisted diffusion.

Bhaduri (1992) has performed thermochemical calculations on combustion synthesis of $MoSi_2$, while Subrahmanyam (1993) has done the same for SiC-$MoSi_2$ composites. The former concluded that $MoSi_2$ was at the border of being self-propagating, i.e., T_{ad} was 1900 K which was slightly higher than the critical temperature of 1800 K. Hence if the SHS mode was used, preheating would be required. As for the latter, Subrahmanyam (1993) concluded that it was possible to produce SiC-$MoSi_2$ composites by combustion synthesis starting from the elemental powders, since the calculated adiabatic temperatures were all higher than 1800 K (Figure 2-2a and 2-2b). Furthermore, according to the free energy change, the initial temperature of the process must be below 1750 K to produce SiC-reinforcement, instead of Mo_2C in the composites (Figure 2-2c).

Deevi (1991, 1994) investigated the reaction mechanism in SHS synthesized $MoSi_2$, by combusting the compact in both argon and vacuum. In both environments, he was able to produce $MoSi_2$ with no traces of the other two equilibrium phases, namely Mo_3Si and Mo_5Si_3. However, in vacuum, the velocity of the propagating wave was observed to be slower. Some samples were quenched while the combustion wave was propagating through. In the region preceding the combustion wave, he observed no solid-solid diffusional reaction which would have produced the intermediate phases such as Mo_3Si and/or Mo_5Si_3. This was expected since the diffusional fluxes ahead of the combustion zones and residence times were low. In the region behind the combustion wave, only $MoSi_2$ was detected. Moreover, there was evidence of wetting and capillary spreading of liquid Si in the microstructure of $MoSi_2$

a)

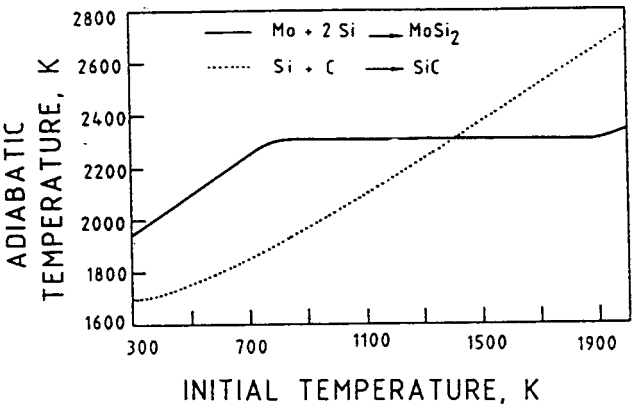

b)

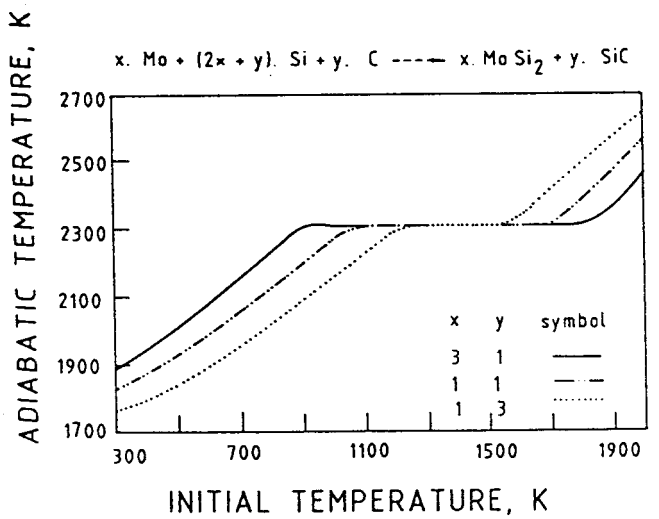

c)

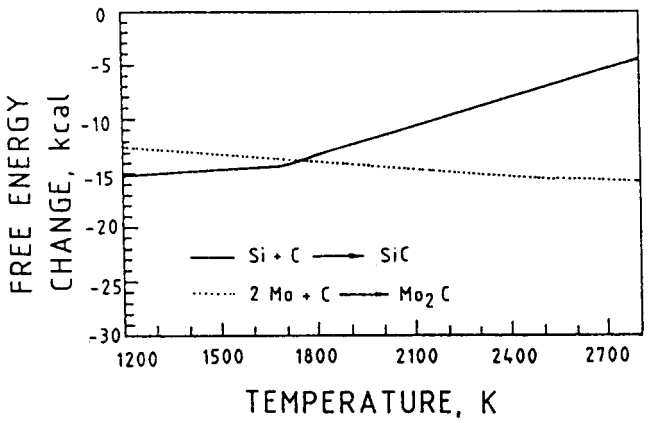

Figure 2-2: Variation of adiabatic temperature with initial temperature for the formation of a) $MoSi_2$ and SiC, b)$MoSi_2$ + SiC composites and c) variation of free energy with temperature for the formation of SiC and Mo_2C (Subrahmanyam 1993).

for all the samples. These results led Deevi to the following conclusions (Deevi 1991, 1994):

1) In argon atmosphere, due to its high thermal conductivity, the heat was able to spread efficiently through the pores of the green compact, hence the velocity and the adiabatic temperature were higher than those in vacuum, for which heat transfer can rely only on the particle-particle contacts and radiation;

2) The SHS of $MoSi_2$ consisted of a one-step process since no intermediate Mo_5Si_3 and/or Mo_3Si phases was found in the reacted and unreacted portions of the sample;

3) The SHS of $MoSi_2$ involved the solid-liquid reaction between liquid silicon and solid molybdenum; therefore, the melting, particle size and size distribution of silicon was the rate limiting factor for the initiation of the reaction and the associated heat release. The SHS was not possible if the particle size of silicon was greater than 80 μm; and,

4) Finally, chemical analysis indicated that the final product had a lower oxygen content than the original powders, hence less silica was present. This was one of the advantages of SHS.

The final conclusion made by Deevi (1991) was further researched by Hardwick *et al.* (1992). Monolithic $MoSi_2$ was produced by simultaneous reaction and densification by hot isostatic pressing at 1400 °C. The final, fully-densified product consisted of $MoSi_2$ and traces of Mo_5Si_3 and SiO_2. The consumption of Si to form SiO_2 caused the mixture to be slightly Mo-rich, leading to the formation of Mo_5Si_3. The amount of SiO_2 in $MoSi_2$ produced by this method was much lower than those produced by hot pressing $MoSi_2$ powder. It was also concluded that SiO_2 grains hindered grain growth resulting in larger $MoSi_2$ grains in the purer

materials.

Subrahmanyam *et al.* (1994) successfully produced $MoSi_2$, $MoSi_2$-WSi_2 and $MoSi_2$-Mo_5Si_3 alloys, using the thermal explosion mode. Morphological and x-ray analyses were performed on the materials. It was suggested that $MoSi_2$ was formed by diffusional reaction between liquid silicon and solid molybdenum, thus confirming Deevi's (1991, 1994) findings. Furthermore, they suggested that $MoSi_2$ melted partially during the combustion process and coalesced to form particles which were greater than 20 μm from the 15-μm molybdenum powder and the 2-μm silicon powder.

Using another approach, Govindarajan *et al.* (1994) used SHS to produce functionally graded materials (FGM) of SiC-reinforced $MoSi_2$ composites in vacuum. The FGM was densified by hot pressing. They found that as the green density increased, the porosity of the final sample decreased (Figure 2-3). Contrary to Deevi's findings, they found traces of Mo_5Si_3, Mo_3Si and molybdenum in the final product; however, explanations were not given. They concluded that the exothermicity (adiabatic temperature) of the reaction decreased with increasing amounts of SiC and with increasing layers of FGM of SiC-reinforced $MoSi_2$ composites, whose mole percentages varied from 0% to 20%. Extinction occurred when a threshold thickness of layers was reached.

Gedevanishvili and Munir (1994) have recently produced SiC-reinforced $MoSi_2$ composites by field-assisted combustion synthesis from their elemental powders. With this method, a voltage was applied simultaneously when the sample was ignited at one end. With the applied voltage, both $MoSi_2$ and the composites were produced. However, without the

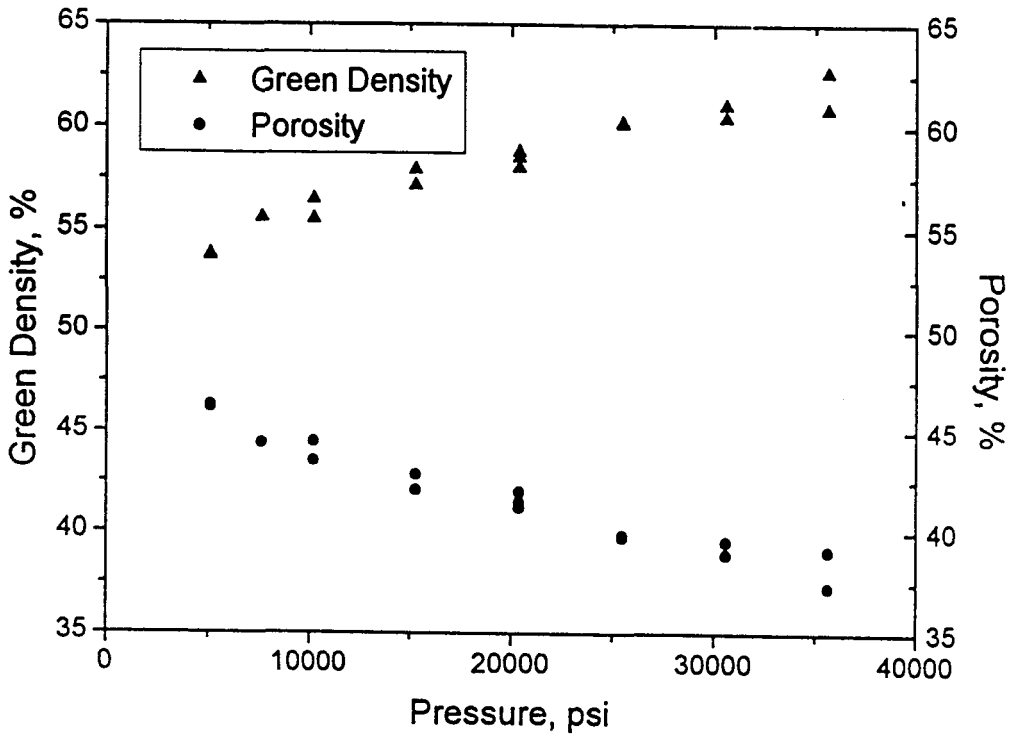

Figure 2-3: Green density and porosity variation for Mo + 2Si = $MoSi_2$ system (Govindarajan *et al.* 1994).

voltage, only $MoSi_2$ was produced and the composites consisted of $MoSi_2$ and unreacted silicon and graphite powders. From these results, they concluded that the composites cannot be produced by using the SHS process, unless it was assisted by an applied voltage. No explanation was given.

Recently, Subrahmanyam and Mohan Rao (1995) produced SiC-$MoSi_2$ composites from the elemental powders, using the thermal explosion mode. They used the results from their thermochemical calculation (Figure 2-2) to explain both morphologies of $MoSi_2$ and SiC in the composites. They suggested that, with a sufficiently high preheat temperature, the corresponding adiabatic temperature would be high enough to complete the Mo + 2Si = $MoSi_2$ reaction, followed by a partial melting of $MoSi_2$. The partially-molten $MoSi_2$ would then coalesce to form a uniform distribution of large-sized grains. However, for the composites, the presence of SiC slightly reduced the exothermicity of the reaction and led to less melting. Therefore, there would be a broader distribution of $MoSi_2$ grain sizes. SiC was uniformly distributed as fine particles, since SiC has a higher melting point than $MoSi_2$, so coalescence of SiC would be unlikely (M.P. of $MoSi_2$ = 2030°C, M.P. of SiC = 2545°C). The actual adiabatic temperatures of these reactions were not measured to confirm these conclusions.

2.2 STRENGTH AND TOUGHNESS OF MATERIALS

Intermetallic compounds are a relatively new class of materials which occupy an intermediate position between the metallic alloys and ceramics. The long range ordering in these materials results in room temperature brittleness like ceramics, but they are ductile like metals at high temperature. Reasons for their brittleness vary for different materials, but are commonly attributed to a limited number of slip systems for plastic flow, a large Burgers vector, restricted cross-slip, difficulty in slip transmittal across grain boundaries and segregation of impurities at grain boundaries (Munroe and Baker, 1988). Therefore, attempts are made to increase the reliability of these materials by improving both the room temperature and high temperature mechanical properties.

Fracture behavior in brittle materials can be described by linear elastic fracture mechanics (LEFM) (Knott 1973a). Fracture under the plane strain conditions can be correlated with the fracture toughness and the flaw-related defect size at the fracture origin (Knott 1973b) by the Griffith fracture criterion:

$$\sigma_f = \frac{K_{IC}}{Y\sqrt{C}} \qquad (6)$$

where σ_f is the fracture stress (MPa), K_{IC} is the plan strain fracture toughness ($MPa \cdot m^{1/2}$), Y is the crack and specimen geometry parameter, and C is the critical flaw size (m).

From this criterion, two fundamental approaches can be used to increase the reliability

of the materials: First, the reduction of the critical flaw size in the materials during processing, and second, the toughening of materials by creating a microstructure that is sufficiently tougher. By doing so, the fracture mode will change from the catastrophic brittle failure to one that is more controllable. The second approach has the advantage that appreciable processing and post-processing damage can be tolerated without compromising the structural reliability (Rühle and Evans 1989; Evans 1990).

2.2.1 FRACTURE-INITIATING DEFECTS

To eliminate and/or reduce the critical flaw size in the materials, the origin of these defects must be first understood. The major types of the fracture-initiating defects are machining flaws, agglomerates, inclusions and pores. These defects constitute fracture origins via peripheral cracks developed during processing (Evans 1979, 1982; Reed 1978; Rice 1979) or in-situ cracks developed in loading (Evan 1980).

Rice (1979) defined machining flaws as surface penny-shaped or semi-elliptical cracks that resulted from surface impact or penetration by hard objects such as grinding and cutting tools. The formation of machining flaws are often simulated by indentation in which the residual tensile stresses underneath the indent due to non-accommodation of the elastic/plastic field amplify pre-existing flaws and result in local fracture (Ostojic 1987). Machining defects

are detrimental to the mechanical properties of materials and obscure the natural strength of the materials if present in fracture test specimens, but they can be avoided by a precision finishing procedure. This procedure is being standardized for the preparation of flexural test specimens. Relevant standards include MIL-STD 1942(A) (1983) and ASTM C1161-90.

Agglomerates are microstructural inhomogeneities due to the pre-association of a number of grains in the precursor powders (Pampuch 1983) and the coalescence of certain grains during the processing and densification processes. Agglomerates are observed to have either higher or lower green density with respect to the surrounding compact matrix (Lange 1983; Kellett 1984). In conventional terminology, these can be divided into "hard" agglomerates which are thought to be held by stronger bonds, resulting from the partial sintering during powder synthesis (Lange 1983), and the "soft" agglomerates which are held by weak Van der Waals interactions and surface charges (Barringer 1984). Since these are relatively weak bonds, they will not survive powder treatments like sedimentation, ball milling and green compaction (Graaf 1983; Lange 1986). Hence, during processing by combustion synthesis and densification, the product will contain a small amount of large grains from the hard agglomerate. These large grains will induce a thermal stress, especially in anisotropic materials with non-cubic crystal structure, which are common in the long range ordered intermetallics. These are the source of defect fracture during loading. Elimination of the agglomerates in precursor powders will result in a more uniform grain size and increase the strength of the final products by minimizing the residual stress due to the coefficient of thermal expansion (CTE) mismatch. This can be achieved by several ways, such as ball

milling or colloidal processing.

Inclusions are the embedded particles with physical properties and chemical compositions different from the surrounding matrix (Sung 1988). Inclusions can be introduced during any of the processing stages. These include impurities in the precursor materials, impurities introduced during milling, green compaction, densification or from atmospheric contamination. Sung (1988) divided inclusions into two types: organic and inorganic. Organic inclusions are usually introduced due to the addition of organic binders and plasticizers during colloidal mixing. They are easily burnt out, but can create pore-like defects in the product if the materials are not densified properly. Inorganic inclusions are usually the oxide impurities which can induce residual stresses due to the CTE mismatch upon cooling from the high temperature densification process and/or the elastic mismatch upon loading. Complicated inclusion fracture, interfacial cracking or radial cracking may occur, depending on the elastic modulus and the fracture toughness of the inclusions with respect to the matrix (Evans 1982; Green 1983). Thus, precautions must be taken in each stage of the processing techniques to eliminate inclusions as they can become fracture origins.

Pore defects can be residual porosity from the green density or they can be produced during the processing stages. Pores may originate from powder density gradients due to non-uniform size distribution of agglomerated powders or inhomogeneities developed during green compaction (Kingery 1976b). Large pores may develop from the ripening of the grain-boundary porosity (Kingery 1976b) or the expansion of existing voids by gaseous phases generated and trapped on the decomposition of extraneous particles (Evan 1982). Large

pores will induce high stress concentrations while small pores may interact with other defects in their vicinity, and both will result in fracture-initiating defects. The pore defects can be eliminated or minimized by employing the proper densification process.

The usual and common method of classifying and identifying fracture-initiating defects is to examine the fracture surface under the scanning electron microscope (SEM). Once identified, the defects can be eliminated or minimized during the subsequent processing steps to improve the fracture strength.

2.2.2 TOUGHENING MECHANISMS

The second approach to strengthen materials is to create a microstructure that is sufficiently tougher; therefore, possessing a greater resistance to crack propagation. The basic toughening processes are : 1) load transfer, 2) crack deflection, 3) zone shielding and 4) crack wake toughening.

Load transfer involves the ability of the material to transfer the load from the matrix, which has a lower elastic modulus, to the reinforcement, which has a higher elastic modulus (Rice 1981). This concept has been applied successfully in the toughening of polymeric and metal matrix composite materials. Assuming the rule of mixtures, the elastic modulus of the composites can be approximated as follows (Ashby and Jones 1980):

1) upper bound :

$$E_c = V_r E_r + (1 - V_r) E_m \qquad (7)$$

2) lower bound :

$$E_c = 1/\left[\frac{V_r}{E_r} + \frac{(1 - V_r)}{E_m}\right] \qquad (8)$$

where E_c is the elastic modulus of the composite (MPa), E_m is the elastic modulus of the matrix (MPa), E_r is the elastic modulus of the reinforcement (MPa), and V_r is the volume fraction of the reinforcement.

The extent of toughening due to load transfer to the reinforcement generally increases as the E_r/E_m ratio (since generally $E_f > E_m$) and volume fraction (V_r) of the reinforcement increases, and is sensitive to the anisotropic nature of the reinforcement (Rice 1981). Furthermore, this mechanism will require a strong interface between the matrix and the reinforcement for effective transfer of the load. Figure 2-4 shows both the upper bound and the lower bound of the rule of mixtures.

Crack deflection can be achieved in two ways. First, it can be deflected by the grains of the matrix material or by the second phase particles if there is a weak grain boundary interface or weak particle-matrix interface as shown in Figure 2-5 (Cook and Gordon 1964; He and Hutchinson 1989). Second, it can be deflected by residual or induced stress fields as shown in Figure 2-6 (Rice 1981). The basis of crack deflection is to reorient the normal direction of the crack by lowering the stress field at the crack tip and/or in front of the crack

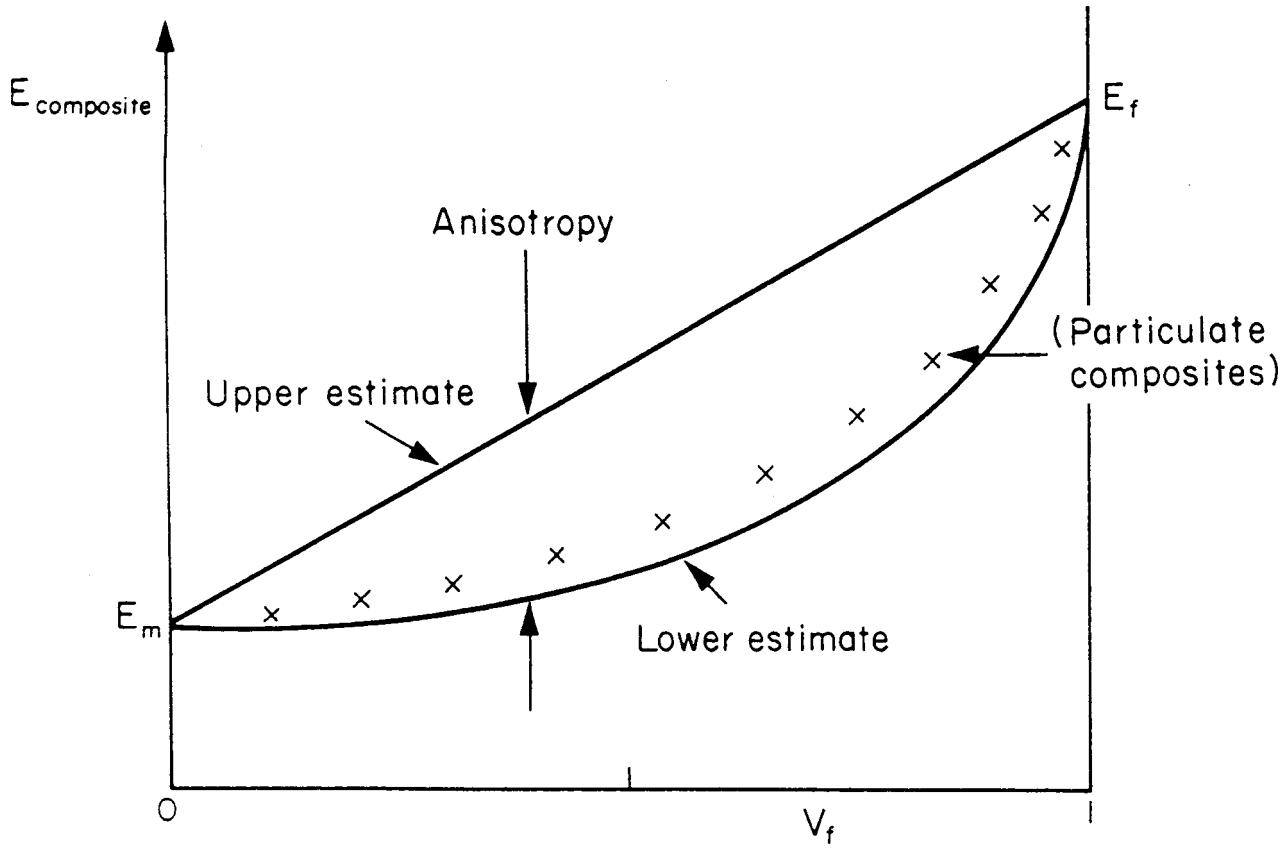

Figure 2-4: Composite modulus for various volume fraction of reinforcement (Ashby and Jones 1980).

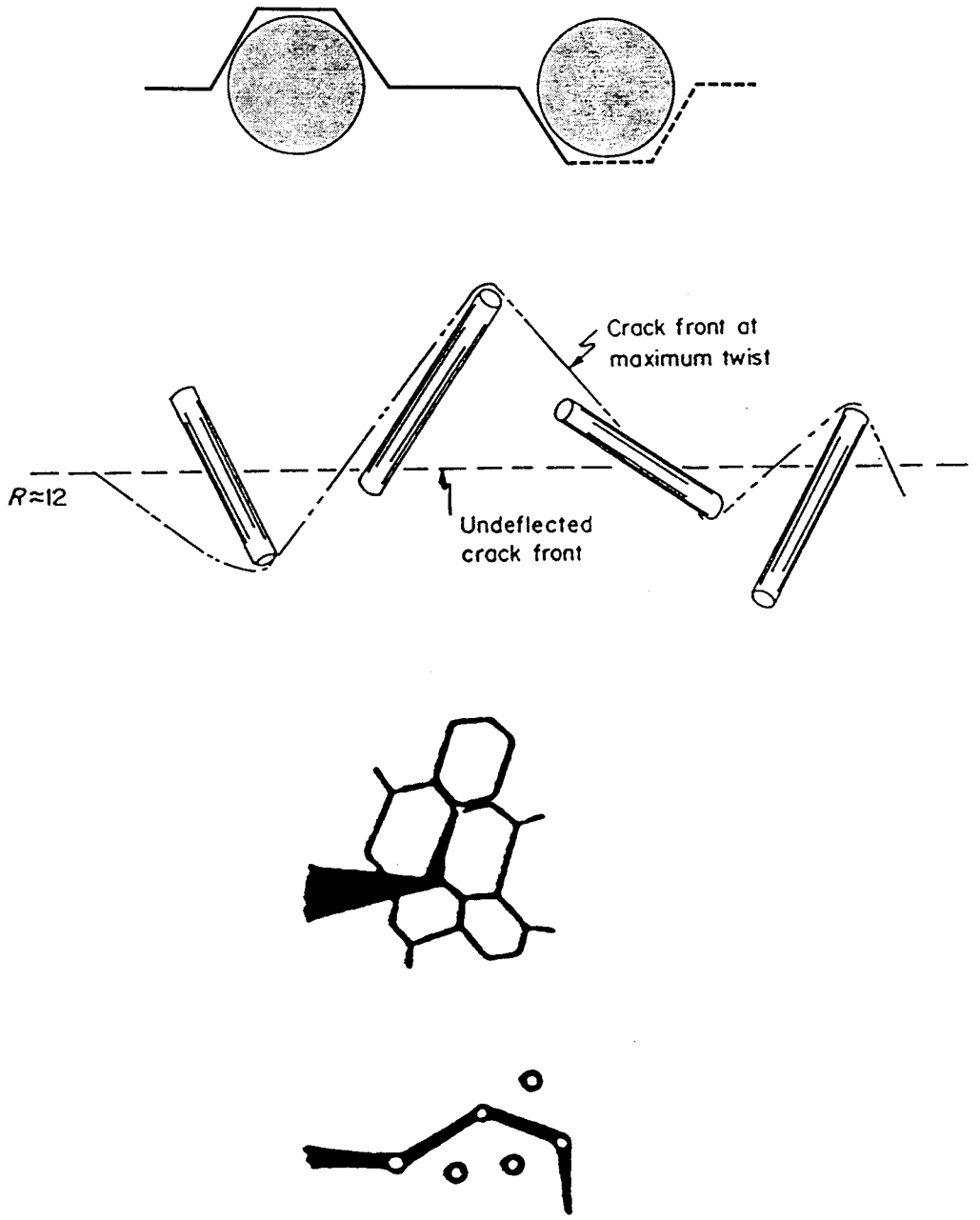

Figure 2-5: A schematic representation of crack deflection as a toughening mechanism (Steinbrech 1992; Faber and Evans 1983).

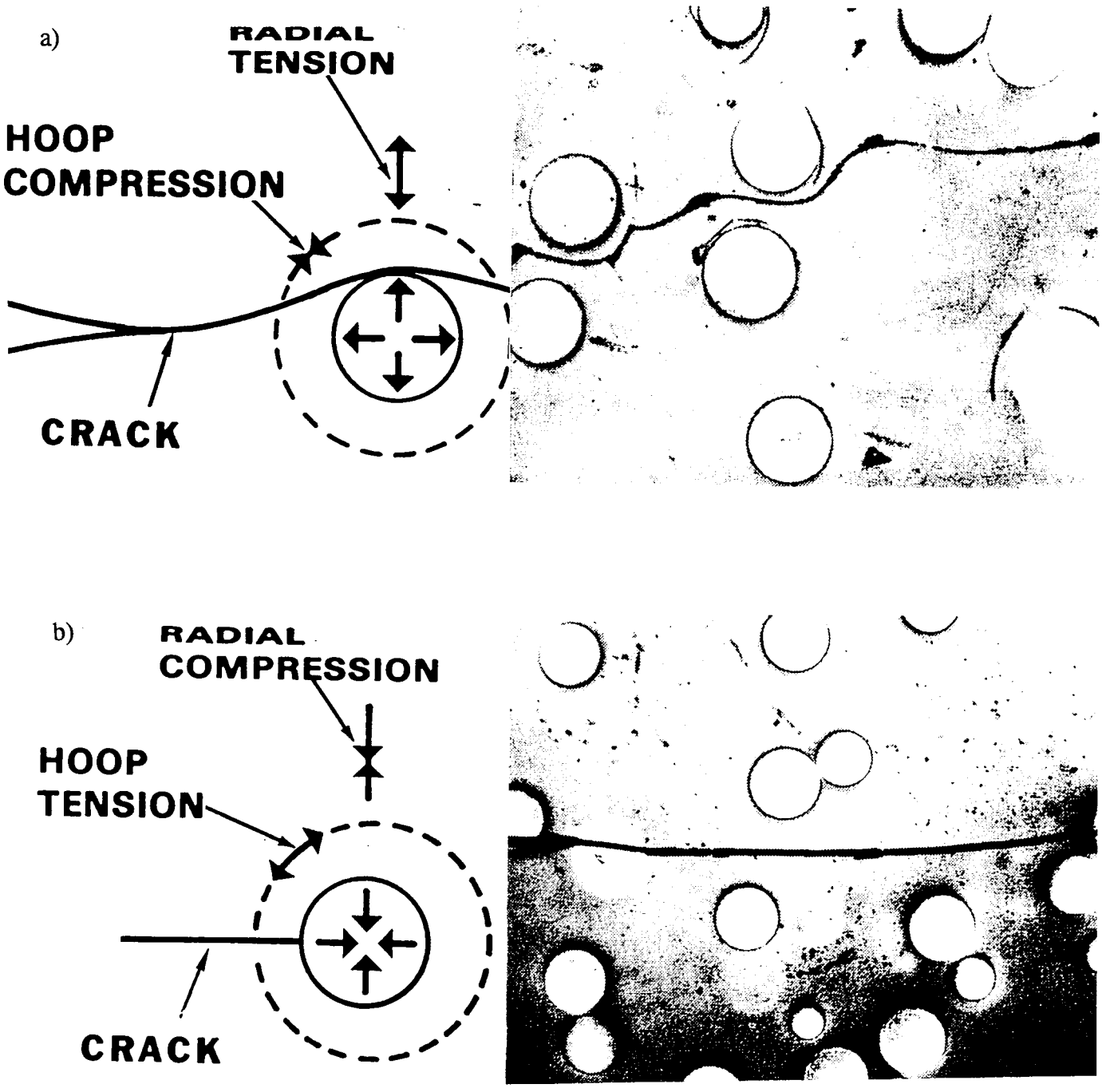

Figure 2-6: Prestressing as a toughening mechanism (Rice 1981; Davidge and Green 1968).

tips, and hence reduce the driving force of the cracks.

The basis of the crack deflection by weak interface is to dissipate the driving force of the crack growth into the creation of new surfaces as it is deflected along the interface, hence increasing the resistance to crack propagation. Whether the crack will propagate along the interface or penetrate through the interface will depend on the strain energy release rate for both processes. This has been analyzed in detail by He and Hutchinson (1989).

Crack deflection by residual or induced stress field arises from the prestressing of the composites due to the differences of coefficients of thermal expansion (CTE) or the differences in the elastic properties between the matrix and the reinforcement. Residual stress is generated during the cooling of the materials from a high temperature (usually greater than 1000 °C) to room temperature during the processing and/or densification of the composites. Together with induced elastic mismatch stress, both can create a net elastic stress field. If this net elastic stress causes the reinforcement to be in tension and the matrix to be in compression, the crack will be deflected around the reinforcement, hence reducing the driving force for crack propagation. On the other hand, if this net elastic stress causes the reinforcement to be in compression and the matrix to be in tension, the crack will be attracted or drawn into the reinforcement. For this case, there is a high probability that the crack reaching the second phase will not fully relieve the compressive stress in the reinforcement. This interaction significantly inhibits the motion of the crack and will arrest the crack propagation completely or temporarily (Rice 1981). This toughening mechanism is also called crack impediment. Figure 2-6 shows a schematic of the prestressing as a toughening

mechanism (Rice 1981).

The effectiveness of this toughening mechanism also relies on the elastic modulus, shape, size, orientation and volume percent of the reinforcement in the composites. The effect of the fibre orientation on the crack deflection mechanism has been analyzed by Evans (1972). This mechanism is most effective with uniaxial fibres aligned parallel with the principal stress, but the effectiveness of such fibres decreases to zero, or less, as the fibre-stress angle increases to 90°. Thus, in this view, particulates seem to give a better isotropy for toughening, but the level of toughening would be substantially less than the fibre's since cracks frequently go around the particles (Rice 1981). An excellent compromise is an ordered array of short fibres or elongated particles distributed such that there are an equal number and spacing in three dimensions. An example of this is the non-cubic precipitates in partially stabilized ZrO_2 (PSZ) as illustrated in Figure 2-7 (Lawn 1993).

The zone shielding toughening mechanism includes phase transformation toughening and microcrack toughening and is shown in Figure 2-8 (Porter *et al.* 1979; Rühle *et al.* 1986). This mechanism arises from an increased screening of the crack tip from the applied stress as the crack grows. The screening causes the irreversible deformation behavior of the individual toughening elements during the passing of the local stress field of the crack. This phenomenon is illustrated by the hysteretic elemental response in their stress-strain curve shown in Figure 2-9 (Steinbrech 1992).

An example of stress induced phase transformation toughening occurs for ceramics containing zirconia. The stress concentration near the crack tip induces the tetragonal to

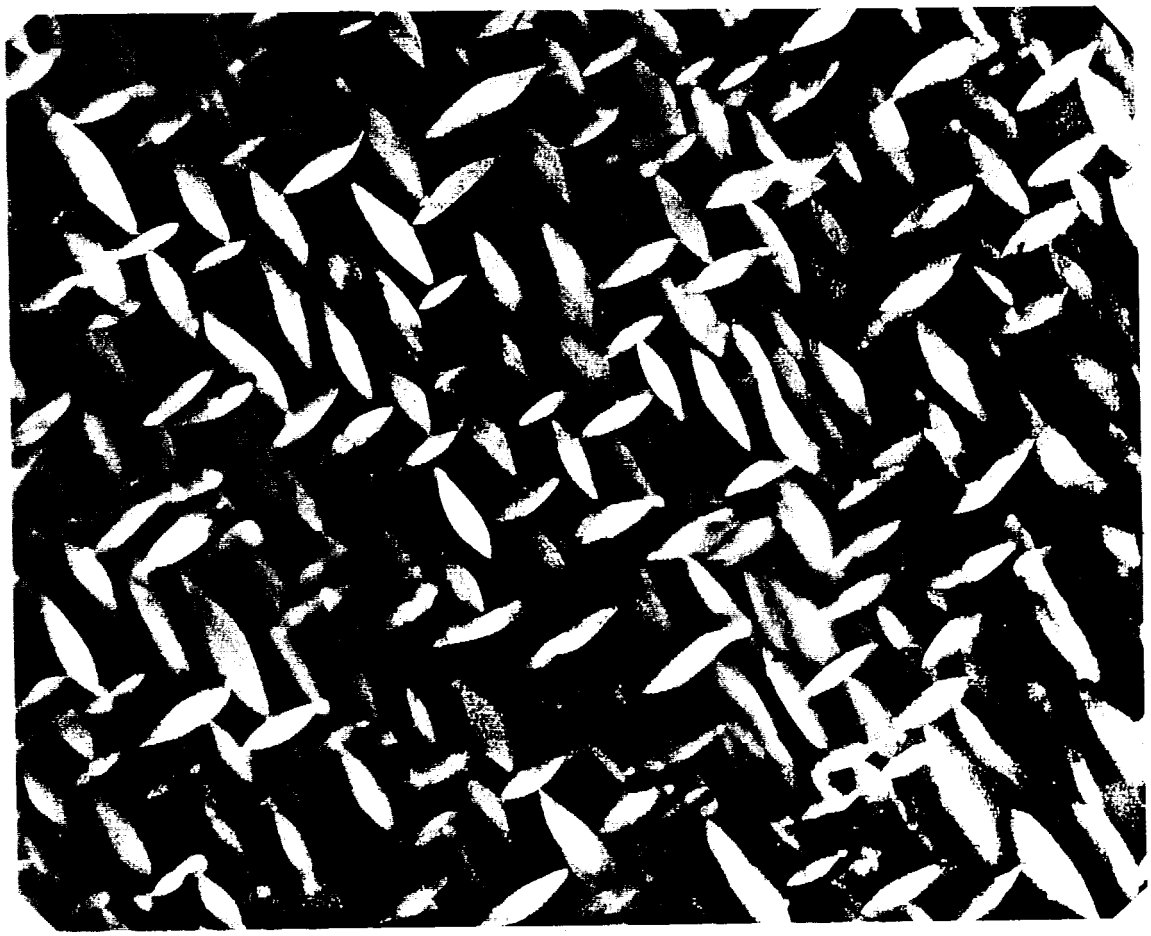

Figure 2-7: Transmission electron micrograph of Mg-PSZ showing untransformed tetragonal precipitates in cubic matrix (Lawn 1993a).

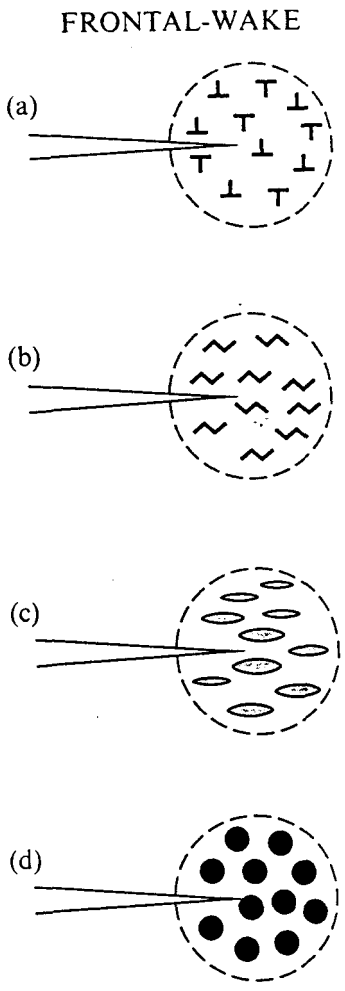

Figure 2-8: A schematic representation of zone shielding as a toughening mechanism: a) dislocation cloud, b) microcrack cloud, c) phase transformation, and d) ductile second phase (Lawn 1993b).

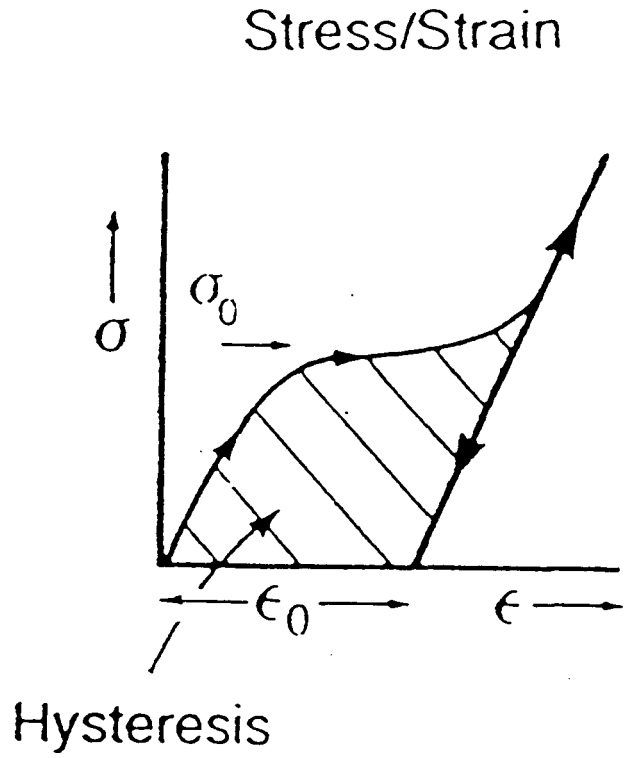

Figure 2-9: A diagram showing non-linear hysteretic elemental response, that leads to enhanced toughness (Steinbrech 1992).

monoclinic transformation of zirconia, which is accompanied by a volume dilation 4.7% (Rühle and Heuer 1984). This dilation will cause a reduction in the crack tip stress, thereby increasing the toughness. More details of this mechanism are described in the literature by Rühle and Evans (1989).

Analogous to the phase transformation behavior of zirconia, stress-induced microcrack formation represents an irreversible deformation phenomenon which is associated with energy dissipation, hence increasing toughness (Evans 1990; Buresch 1975). This induced stress can arise from thermal expansion and elastic modulus anisotropy of non-cubic polycrystalline materials such as $MoSi_2$ or differences in elastic moduli and thermal expansion coefficients in composite materials (Evans and Faber 1984). The residual stresses are then relieved by forming a damage zone of microcracks. Evans (1988) proposed that toughening arises from two effects. The crack tip causes a dilation of the microcracks which is governed by the volume they displace. This dilation of the crack surface gives rise to frictional crack bridging effects which shield the crack tip from the external applied stresses. However, this toughening mechanism arises only from particles or grains within a narrow range as shown in Figure 2-10 (Evans and Faber 1984; Evans 1984). Thus, there are strict requirements on microstructural dimensions and uniformity to achieve a large increase in toughness due to microcracking (Evans 1988). Moreover, in the absence of an applied stress, microcracking will simply degrade the material but this can be inhibited by reducing the grain size or inclusion size below a critical point (Green 1981). Finally, the microcracks can toughen the materials by crack-branching. This process will reduce the driving force of the main crack,

a)

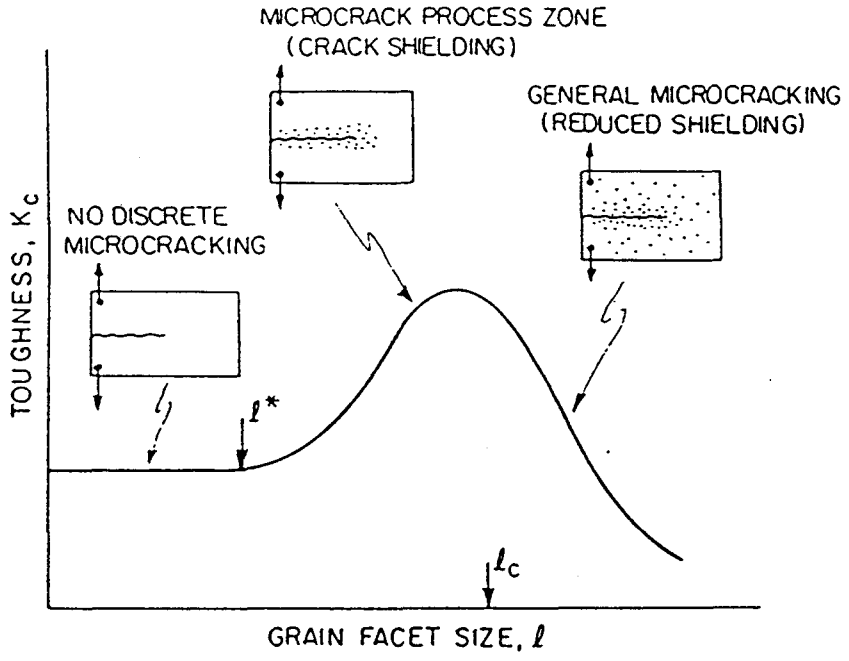

b)

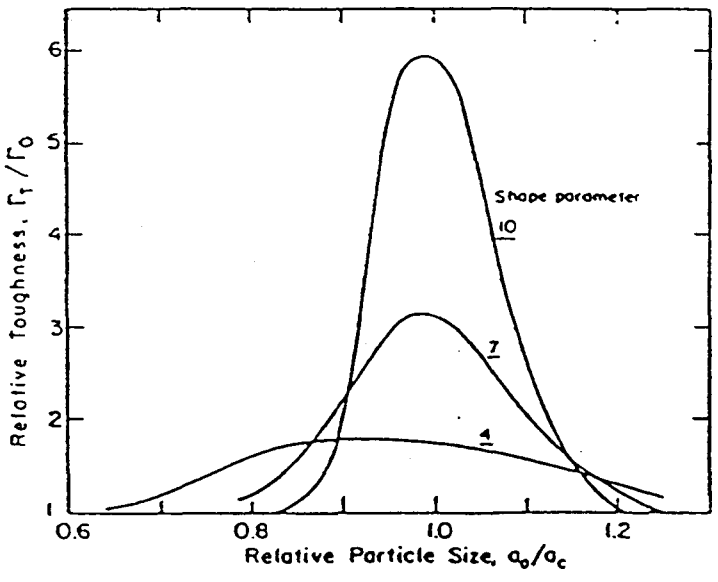

Figure 2-10: Effect of a) grain size (Evans and Faber 1984) and b) particle size (Evans 1984) on microcracking toughness.

hence increase the resistance to crack propagation.

Crack wake toughening involves localized interaction at the crack faces in the form of crack bridges and pullout in the crack wake as illustrated in Figure 2-11. In this case, the energy dissipation arising from the separation of the interacting element is responsible for the additional toughening effect. The interacting elements include grain localized bridging, and whisker, fibre and platelet pullout. Specifically, the energy is dissipated while overcoming the friction controlled pull out behavior found in materials such as fibre strengthened composites as shown in Figure 2-12 (Rühle and Evans 1989). A detailed description of this toughening mechanism can be found in the review articles by Steinbrech (1992) and Rice (1981), and will not be discussed further. Furthermore, this mechanism is not expected to contribute to the toughening of the composites used in this study.

By studying the experimental results on ceramic matrix composites over the years, Evans (1990) has ranked the effectiveness of the types of reinforcement/toughening mechanism, as follows :

1) continuous fibres reinforcement (most effective);

2) ductile metal second-phase dispersion;

3) ceramic composites with zirconia transformation toughening effect;

4) second-phase whiskers/particulates/platelets; and,

5) matrix microcracking (least effective, but still significant).

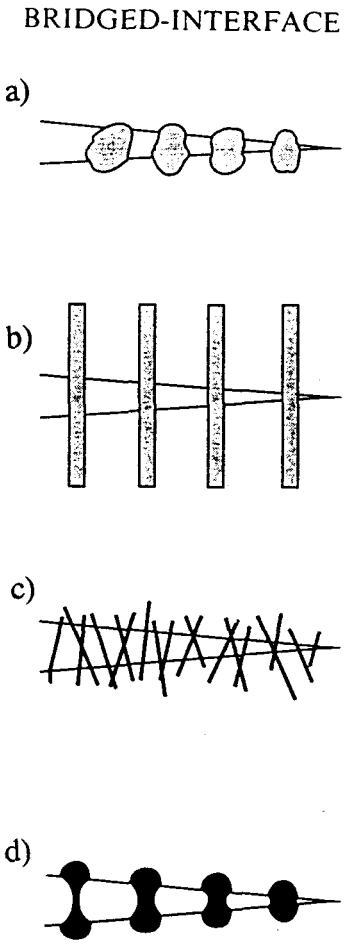

Figure 2-11: A schematic representation of crack wake toughening as a toughening mechanism: a) grain interlock, b) continuous-fibre reinforcement, c) short-whiskers reinforcement, and d) ductile second phase (Steinbrech 1992; Lawn 1993c).

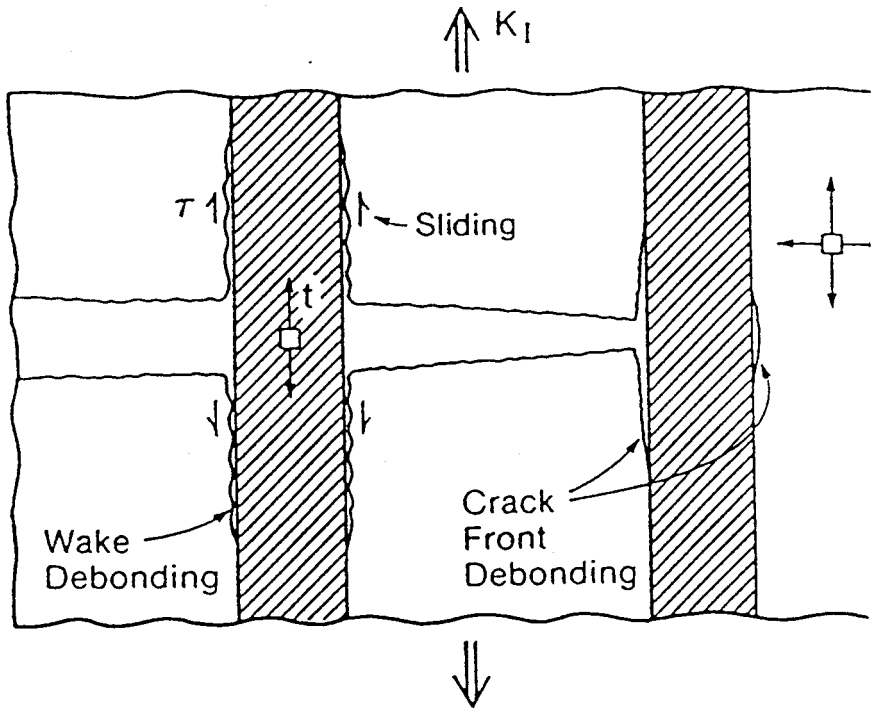

Figure 2-12: A schematic diagram of whisker/fibre debonding (Rühle and Evans 1989).

2.3 SiC-REINFORCEMENT

When designing composites, matching the coefficients of thermal expansion (CTE) between the matrix and the reinforcements is very important. The idea is to minimize the effects of interfacial cracks on mechanical properties (Lu 1991) and on shock resistance due to thermal stress, which will become crack initiation sites. Figure 2-13 shows the CTE of various reinforcements and of $MoSi_2$ with temperature. Although the CTE differs by nearly a factor of two between SiC and $MoSi_2$, SiC reinforcement was still chosen. The main reason it was chosen was to produce SiC-$MoSi_2$ composites from their elemental powders by combustion synthesis, which was the objective of the study. This intent would not be possible if Al_2O_3 was chosen, although its CTE matches quite closely with that of $MoSi_2$. Furthermore, it has been shown experimentally that there is no interfacial crack or reaction in SiC-$MoSi_2$ composites if the size of SiC reinforcements is less than 20 μm, regardless of the shape of reinforcements (Lu 1991; Jang and Koch 1990), showing that there is no effect of the geometry of the reinforcement on the residual stress state in the composite. Also, the addition of SiC reinforcements does not significantly change the oxidation resistance of $MoSi_2$ (Lee *et al.* 1991). As for Al_2O_3 reinforcements, at typical densification temperature of 1600°C, experiments have shown that $MoSi_2$ was reduced by Al_2O_3 to form Mo_5Si_3 and SiO (g) (Meschter and Schwartz 1989).

The size, geometry and distribution of the SiC reinforcements will significantly affect the properties of the resulting composites, but they were not predetermined in this study

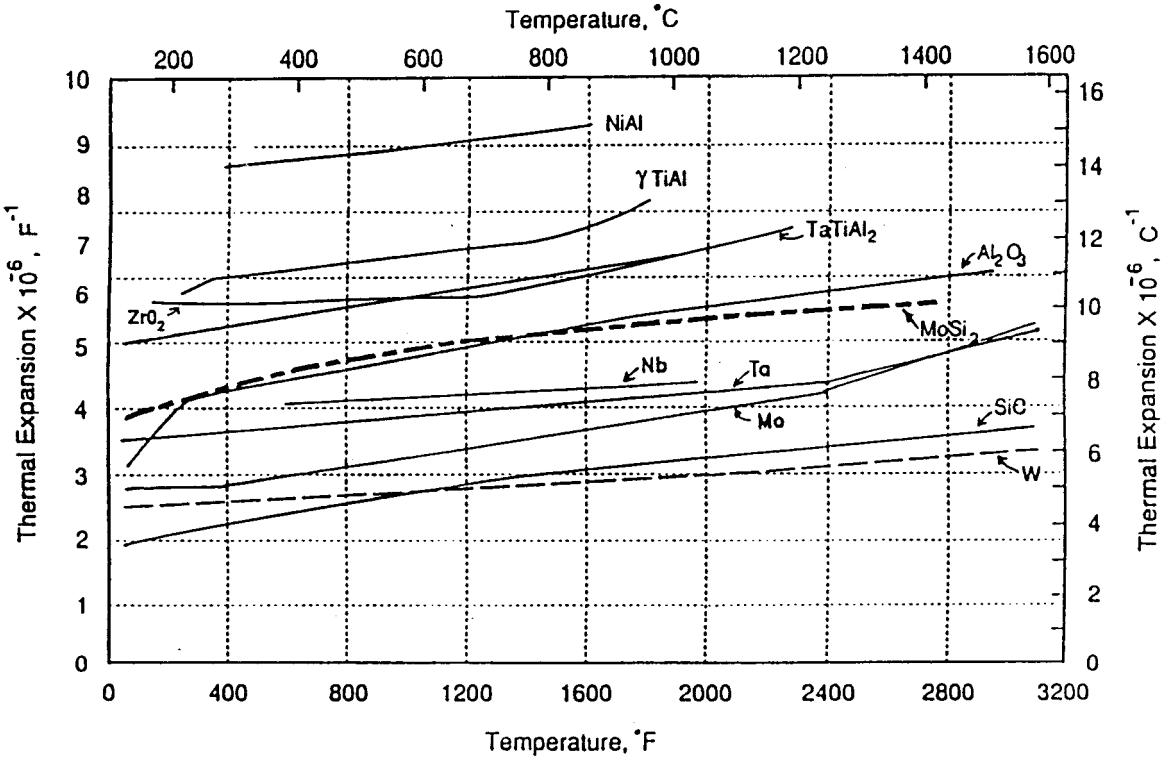

Figure 2-13: Thermal expansion coefficients of various materials (Vasudévan and Petrovic 1992).

because they were formed in-situ and controlled by the combustion synthesis process. The initial intent was to use the SHS mode of combustion synthesis to produce SiC whiskers, since TiB whiskers were produced using this method (Petric *et al.* 1993). However, in this study, SiC particulates were formed instead of whiskers. The reason for the formation of TiB whiskers is still under investigation.

2.4 TOUGHENING MECHANISMS IN SiC-$MoSi_2$ COMPOSITES

By examining the fracture surfaces under the SEM, Wade and Petrovic (1992a, 1992b) determined that the dominant fracture mechanisms operating in $MoSi_2$ was transgranular fracture, regardless of the grain size. However, as the grain size decreased, the transgranular fracture mode became less dominant. Moreover, when examining the crack paths produced by indentations, crack deflection was observed at the grain boundary.

In SiC-whisker and -particulate reinforced $MoSi_2$ composites, the toughening mechanism is attributed to crack deflection, crack branching, crack bridging and residual stress at the reinforcement-matrix interface (Bhattacharya and Petrovic 1991; Carter and Hurley 1987; Gac and Petrovic 1985). In addition to the toughening mechanisms mentioned, microcracking is also attributed to toughening SiC-fibre reinforced $MoSi_2$ (Yang and Jeng 1991).

It is important to note that no work to date has been done on the room temperature

properties of SiC-$MoSi_2$ composites produced by combustion synthesis. Therefore, the objective of this project is to study the mechanical properties of combustion synthesized SiC-$MoSi_2$ composites.

2.5 MECHANICAL TESTING

2.5.1 HARDNESS

The hardness test is an alternative to the tensile test, as the resistance of the materials to indentation can be correlated, qualitatively and sometimes quantitatively, to its strength. Hard indent contact with the surface of brittle materials produces irreversible damage in the area of the indent impression and can initiate various cracks propagating away from the indent (Evans 1976; Lawn 1979). Figure 2-14 shows a schematic of a Vickers-produced indentation-fracture system (Chantikul 1981; ASTM E92-82). The extent of the indent impression and cracking is related to the elastic/plastic stress field beneath the indenter which is determined by the applied load and the properties of specimen (Lawn *et al.* 1980; Marshall and Lawn 1979). Indenters are available in different geometries and are made from different materials, leading to variations in hardness tests. Examples include Brinell, Vickers, Knoop and Rockwell hardness tests. The details of each test can be found in any introductory text book on materials engineering. Empirical hardness numbers are calculated from the

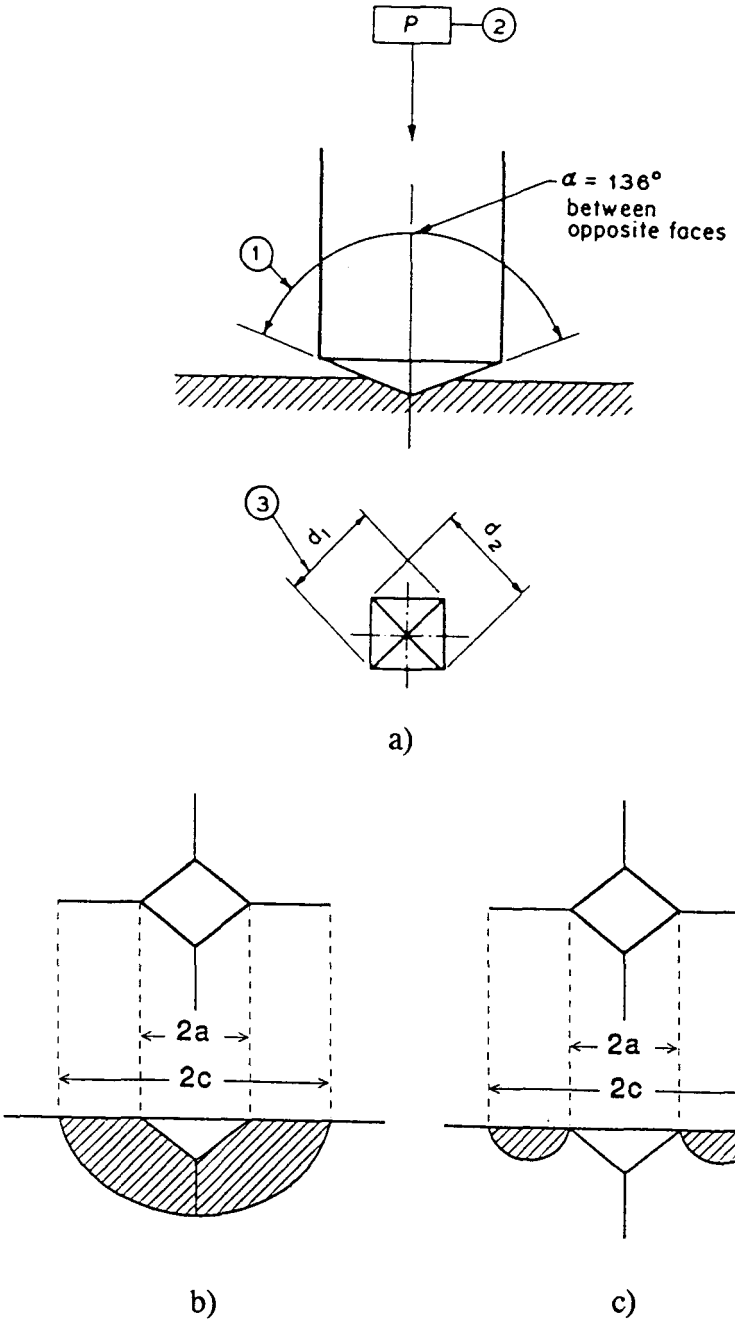

Figure 2-14: A schematic of a)Vickers-produced indentation-fracture system (Chantikul 1981), b)median crack profile, and c) Palmqvist crack profile.

appropriate formulas using the indentation geometry measurement, and hence comparisons of hardness between materials should be done only if they are subjected to the same indentation test.

2.5.2 FLEXURAL STRENGTH

Fracture strength is an important mechanical property for the purpose of materials development and design. It is defined as the maximum opening-mode (mode I) fracture stress in a uniform tensile stress state and is related to the fracture-initiating flaws through the fracture toughness (Sung 1988). The flexural strength of brittle materials is usually measured in bending rather than in tension because of the difficulties with the fixture grip and the specimen preparation problem of these materials. In the bend test, a load is applied through loading pins to create a pure bending moment on a parallelepiped specimen. Three test geometries are typically used as shown in Figure 2-15. On loading, the specimen is subjected to a stress distribution with a compressive stress on the top surface and a tensile stress on the lower surface. The maximum tensile stress will occur along the extreme outer lower surface between the inner loading pins (Figure 2-16). This maximum tensile stress is defined as the flexural strength of the material in bending.

As shown in Figure 2-16, there is a greater area of the specimen that is subjected to the maximum tensile stress in the four-point bend test. The four-point bend test ensures a

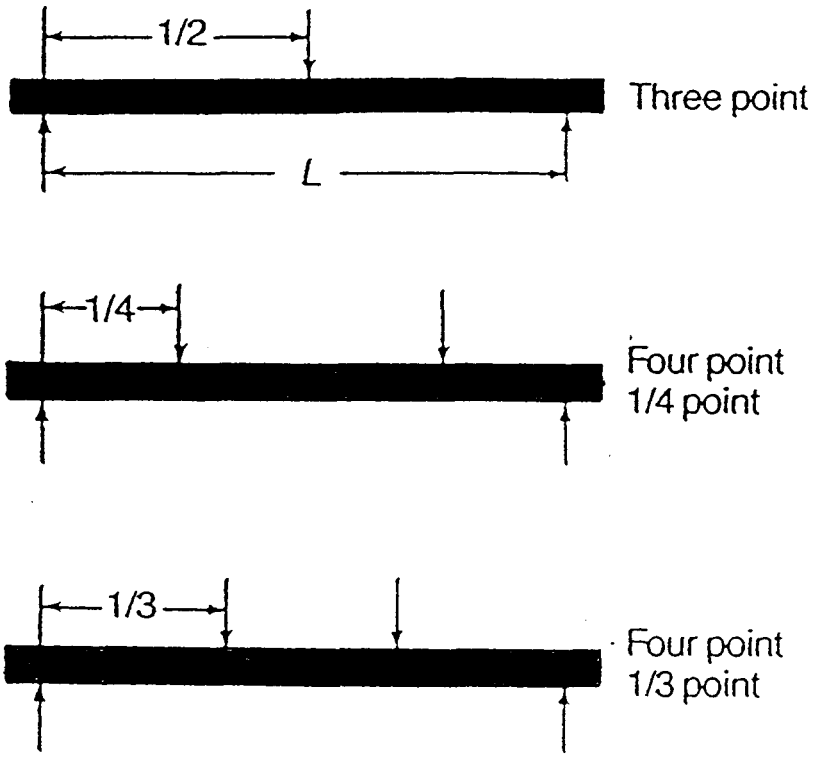

Figure 2-15: Geometries for bend test to determine the flexural strength.

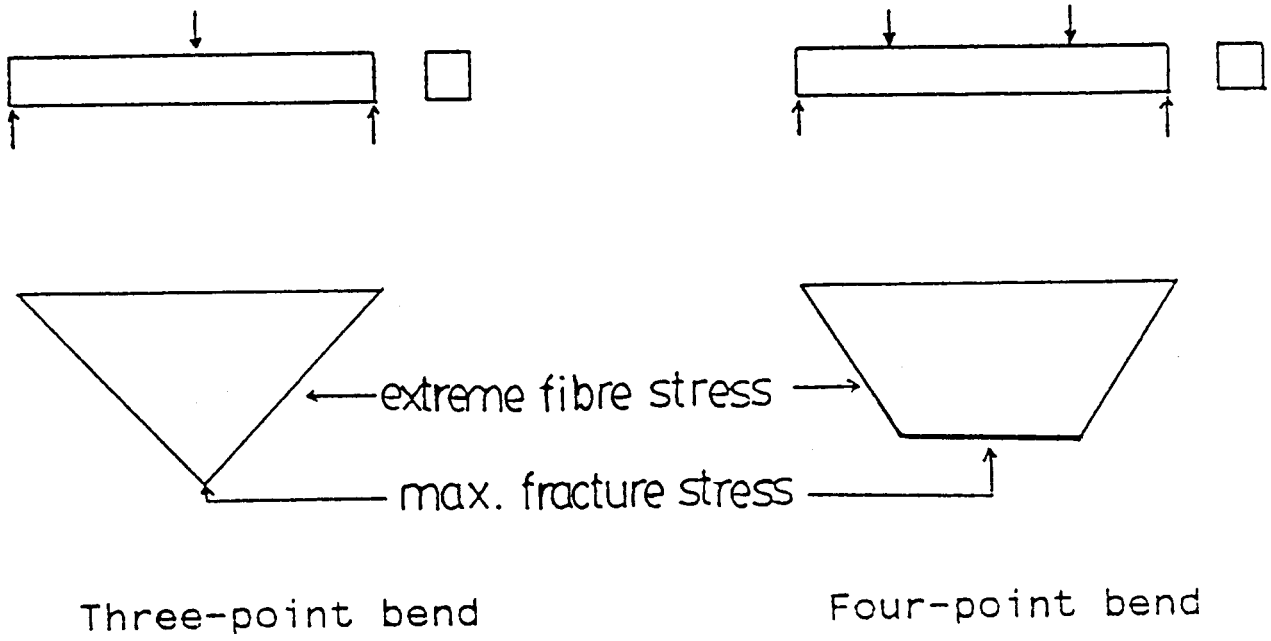

Figure 2-16: A schematic of the volume of material subjected to the maximum tensile stress during three and four-point bending (Sung 1988).

higher probability of stressing a critical flaw than the three-point bend test. Calculation of the flexure stress is based on the simple beam theory with the assumptions that the material is isotropic and homogeneous, the moduli of elasticity in tension and compression are identical and the material is linearly elastic. Thus, this test is not suitable for continuous fiber-reinforced specimens.

To achieve reliable results from this test, extreme care must be taken during specimen preparation since it is very surface and edge sensitive, and the test itself is very error-prone (Hanney and Morrell 1982). Therefore, testing standards have been developed for the flexural strength at ambient temperature (MIL-STD 1942(A) 1983, ASTM C1161-90) which specify the rigorous requirements for the fixture design, specimen dimension, specimen preparation (shape and finish), loading-machine, cross-head speed and number of samples to be tested for reliable results. Figure 2-17 shows ASTM C1161-90 standard specimen dimensions and rig set-up for a four-point bend test. In addition, the results of these tests have to be analyzed statistically (for example, Weibull statistic) to characterize the inherent variability of strength of the materials which depends on the size and geometry of the test specimens.

2.5.3 FRACTURE TOUGHNESS

The fracture toughness relates the fracture stress to the critical flaw size and the

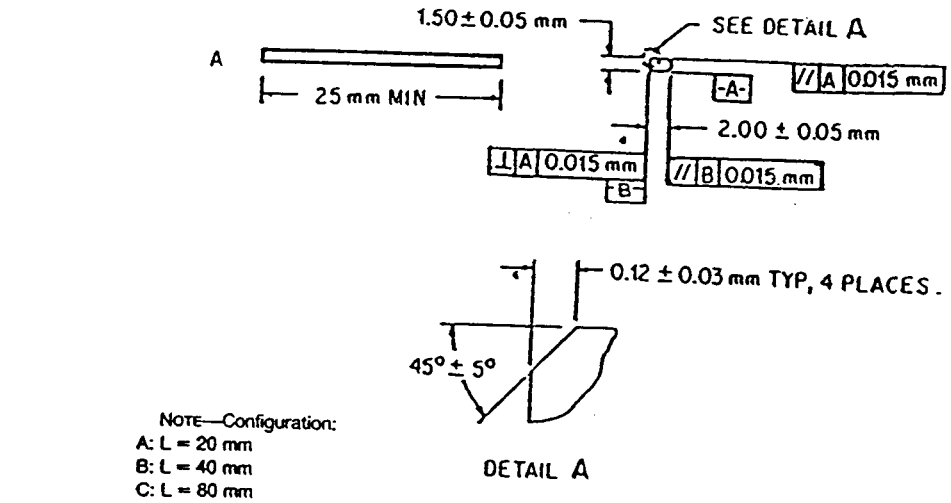

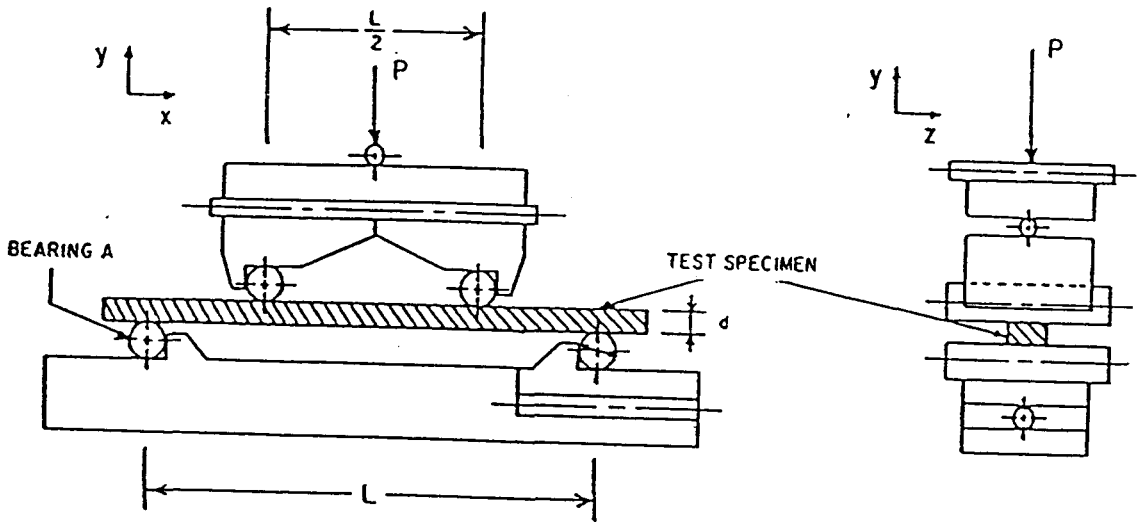

Figure 2-17: ASTM C1161-90 standard specimen dimensions and rig set-up for a four-point bend test.

geometry of the specimen. This mechanical property is one of the most important parameters in the evaluation and design of the materials. ASTM E399 standard testing method can only be used to measure the fracture toughness of metallic materials. It is not suitable for brittle materials, because the test requires measurement from a fatigue precrack in the specimens, which is not applicable in brittle materials.

The basic requirement for this test is that the specimen should contain a stable straight crack that is stress free and sufficiently sharp such that the test measures the difficulty of initiating fracture (Almond and Roebuck 1978). A variety of tests have been designed to meet this criteria: double-cantilever beam (DCB) (Gillis and Gillman 1964), double torsion (DT) (Freiman 1988), indentation technique (Chantikul *et al.* 1981), single-edge pre-cracked-beam (SEPM) (Nose and Fujii 1988) and chevron-notched-bend-bar method (CNB) (Munz *et al.* 1980). The advantages and disadvantages of these methods have been discussed in detail in the literature by Freiman (1983). Since the chevron-notched-bend bar method and the indentation-crack technique were used in this study, only these two techniques will be discussed further.

The fracture toughness test by the chevron technique is employed to facilitate and guarantee the development of a slowly advancing steady-state sharp crack from the chevron-shaped notch and propagating in a chevron-shaped ligament. This technique has the merit of easy specimen preparations without pre-cracking and data procurement without the knowledge of the crack length, since subcritical crack growth and problems with crack initiation difficulties can result in invalid measurement (Barker 1977; Shih 1979). Several

specimen types are possible for this test, but the bend-bar specimen is chosen for the ease of specimen preparation and mechanical testing. The loading arrangement and the geometry of the four-point-bend chevron-notched bar are shown in Figure 2-18 (Munz *et al.* 1981).

A chevron-shaped notch is cut into one side of the specimen and, upon loading, a crack with initial length, a_o, will propagate from the chevron apex. The crack width, b, will continuously increase from zero to the full specimen thickness, B, corresponding to a crack of length a_1 (Sung 1988). The geometry of the chevron-notched bar requires that an increasing load is needed to maintain crack extension which results in the stable crack growth (Sung 1988). Therefore, for the measurement to be valid, stable crack growth must precede final failure, which appears as the non-linear region on the load-displacement curve between the initial elastic region and final failure (Figure 2-19) (Munz 1983).

The indentation-crack method involves the measurement of radial cracks introduced by an indenter. Generally, a Vickers indenter is used because of its ability to produce well defined radial cracks on ceramic surfaces as shown in Figure 2-14 (Swain 1976). The fracture toughness can then be calculated by a relationship developed by Anstis *et al.* (1985). The advantages of this method are its ease and simplicity of implementation, since there is no stressing of the specimen and the test requires a minimal amount of materials. Furthermore, for many brittle materials, indentation fracture is a better approximation than the fracture from small, naturally occurring flaws. However, the derivation of the relationship by Anstis *et al.* (1985) is based on the dimensional analysis of a well defined radial/median crack, assuming that there is no lateral crack formation and interaction. This assumption is material

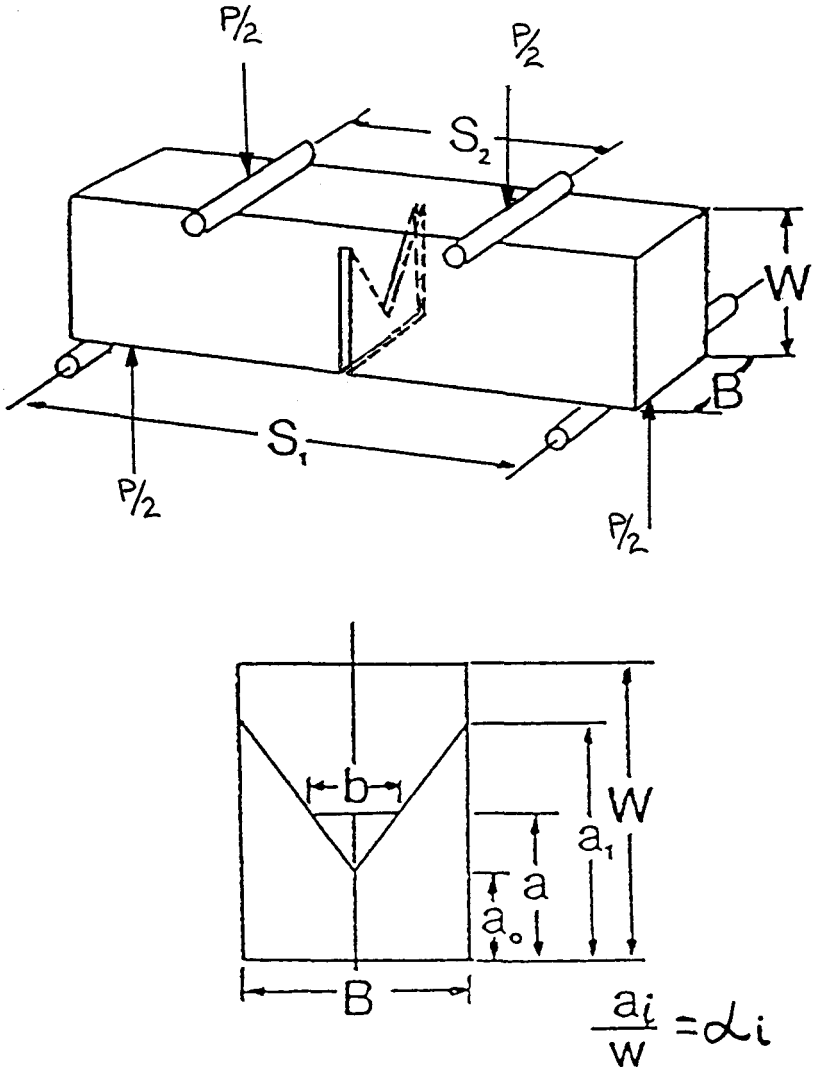

Figure 2-18: A schematic diagram of the loading arrangement and the geometry of the four-point-bend chevron-notched bar (Munz *et al.* 1981).

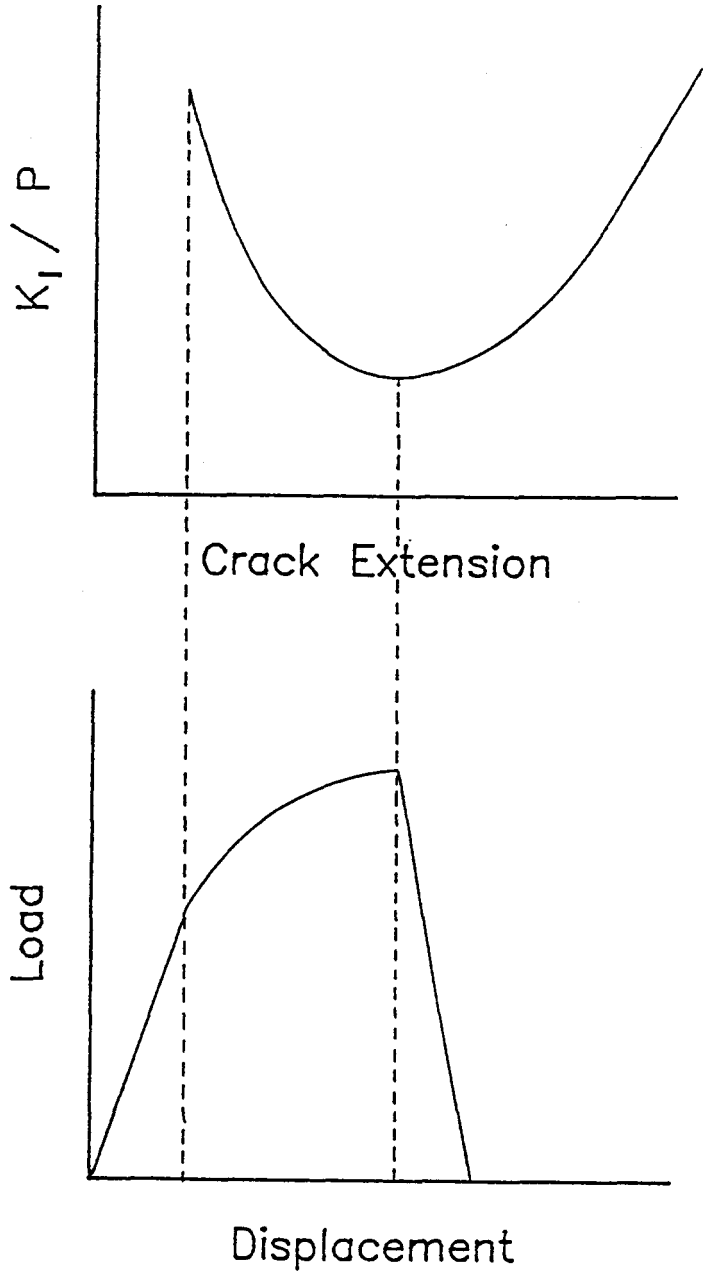

Figure 2-19: Non-linear region on the load-displacement curve for a chevron-notched bend bar (Munz 1983).

dependent, hence this method is only a rough estimate of fracture toughness. Furthermore, residual stress effect produced by the indentation is not taken into account in the formulation.

On loading, the indentation produces a plastic impression and a semi-elliptical microcrack (median crack), but on unloading, compressive stresses persist in the plastically deformed region, creating residual tension at the tip of the microcrack (Figure 2-20). This process will have an effect on the extension of the crack length, which is the chief cause of the discrepancy between the results produced by this method and other conventional methods. The results obtained by indentation are generally 20-30 % higher (Petrovic and Jacobson 1974; Inglestrom and Nordberg 1974; Petrovic *et al.* 1975). To minimize the error, a 30-kgf load was used to produce a well-developed (uniform and reproducible) indentation pattern by giving rise to crack lengths substantially larger than the indentation diagonals. In this study, all ratios of total crack length to indentation diagonal were greater than 2, which was recommended for reliable results (Anstis *et al.* 1981; McColm 1990). Regardless of the precautions, this method was only used to complement the chevron-notched technique.

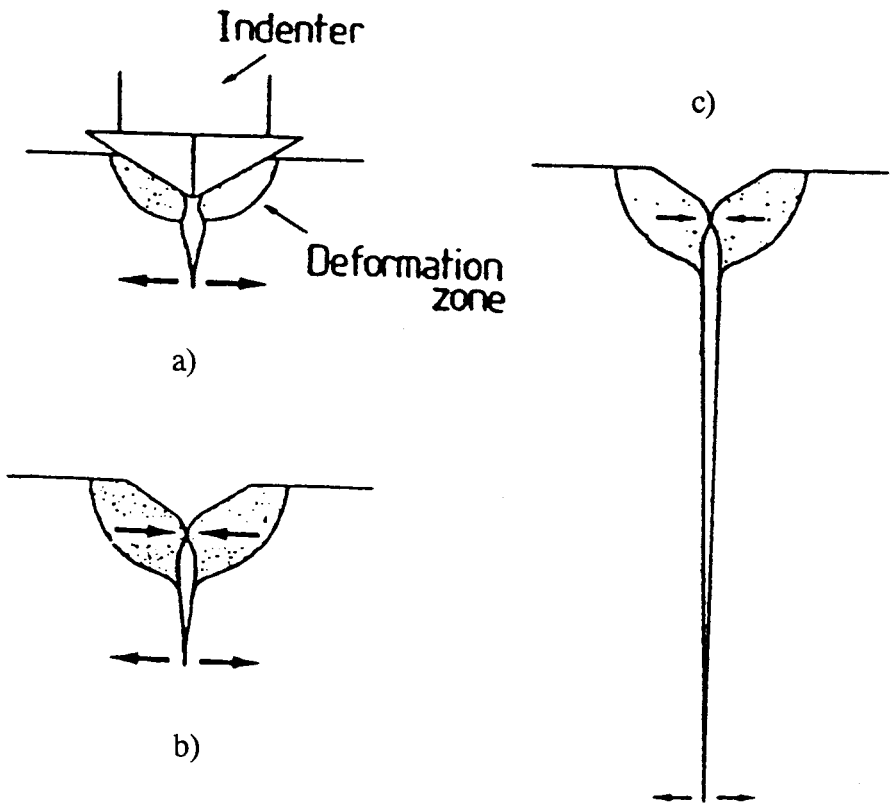

Figure 2-20: A schematic of the residual stress effect of an indentation (Bloyce 1993).

III. THE PROCESSING OF $MoSi_2$ AND SiC-REINFORCED $MoSi_2$

3.1 THE MATERIALS PROCESSING

Commercially available molybdenum, silicon and graphite powders obtained from Johnson Matthey[1] were used in this study. The powder compositions and sizes reported by the manufacturer are shown in Table 3-1. To further characterize these powders, their particle size distributions and mean powder sizes were measured by an optical transmission method based on the principle of liquid-phase sedimentation[2] (Figure 3-1). The mean particle sizes of the molybdenum, silicon and graphite powders were 5.84, 1.95 and 2.85 μm, respectively. Figure 3-2 shows the flow chart of the processing steps employed in this study. Figure 3-3 shows the photographs of the samples after each step.

3.2 THE COMBUSTION SYNTHESIS PROCESS

Molybdenum, silicon and graphite powders were weighed and mixed stoichiometrically to produce $MoSi_2$, 10 vol% and 20 vol% SiC-$MoSi_2$ composites. The

---

[1]Johnson Matthey, Alfa Aesar, Massachusetts, USA.
[2]CAPA-700 Horiba Particle Size Analyzer, SSCAN, Richmond Hill, Canada.

Element	Molybdenum Powder	Silicon Powder	Graphite Powder
Mo	>99.95%	0.3ppm	
Si	<0.001%	99.999%	1ppm
C	0.001%		99.9995%
Fe	<0.001%	1ppm	2ppm
Al	<0.001%	0.5ppm	1ppm
Mg	<0.001%	2.0ppm	1ppm
Mn	<0.001%	0.1ppm	
Cr	<0.001%	0.2ppm	
Ca	<0.001%	0.6ppm	
Pb	<0.0015%		
Cu	<0.001%		
Sn	<0.001%		
N	<0.001%		
W		0.2ppm	
Ti	<0.001%		

Molybdenum powder = 5.84 microns
Silicon powder = 1.95 microns
Graphite powder = 2.85 micron

Table 3-1: Composition of molybdenum, silicon, and graphite powders.

a)

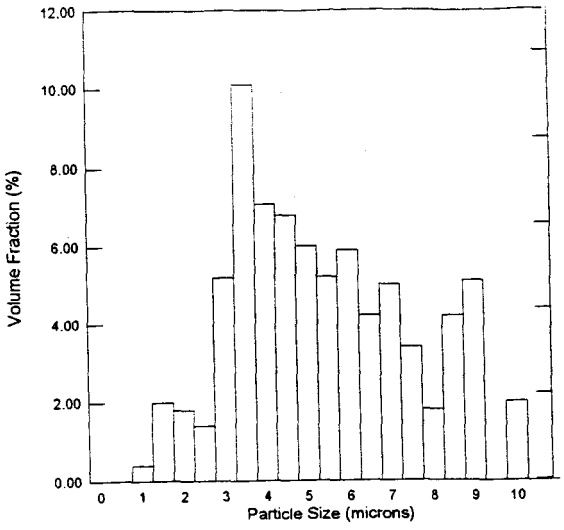

b)

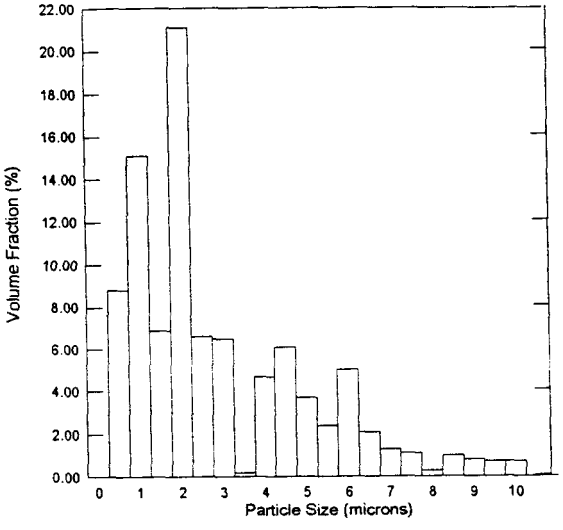

c)

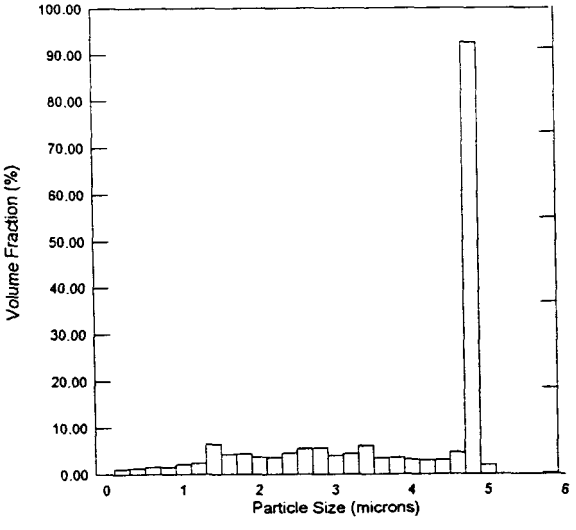

Figure 3-1: Particle size distributions of a) molybdenum, b) silicon, and c) graphite powders.

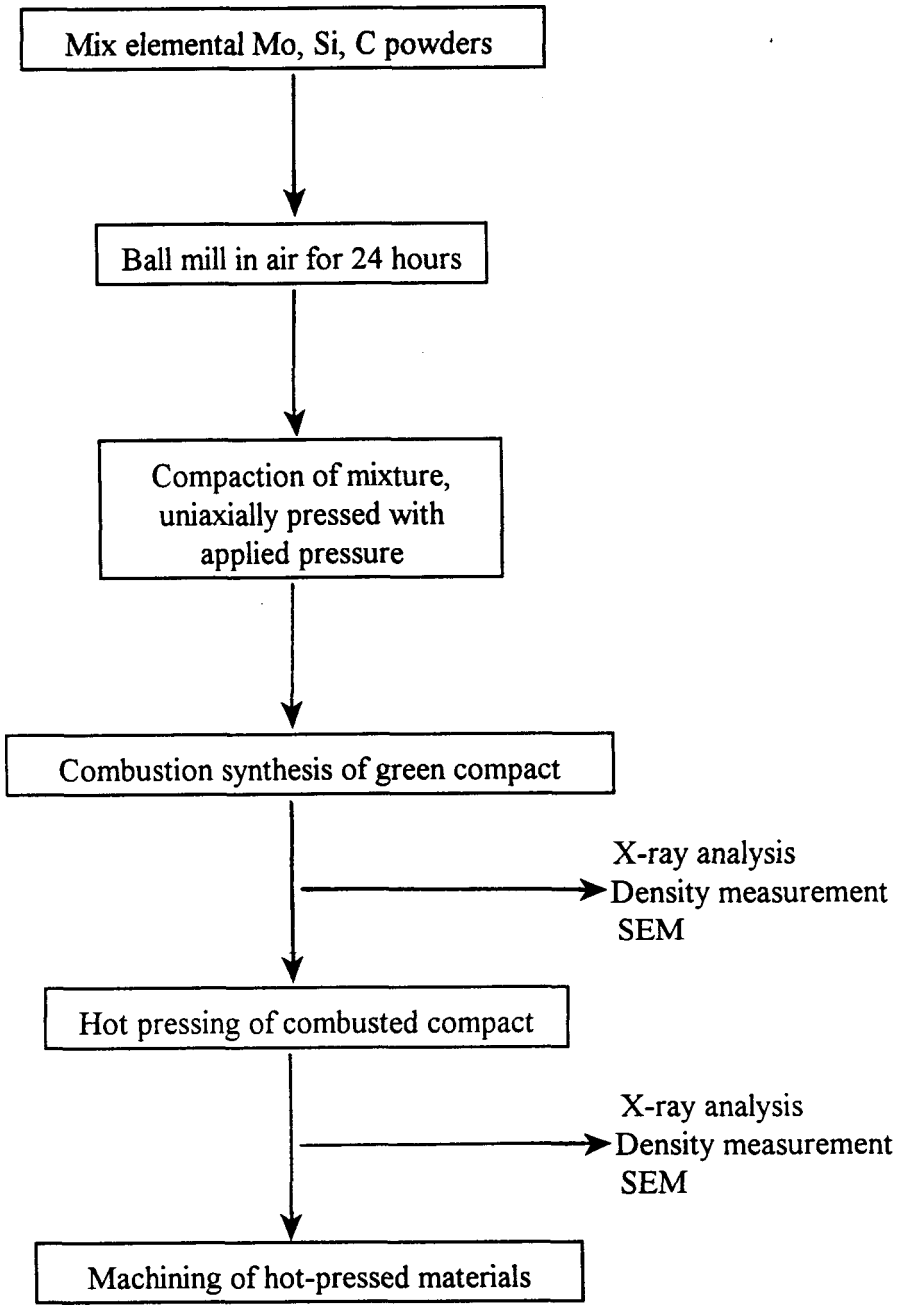

Figure 3-2: Flow chart of the processing steps employed in this study.

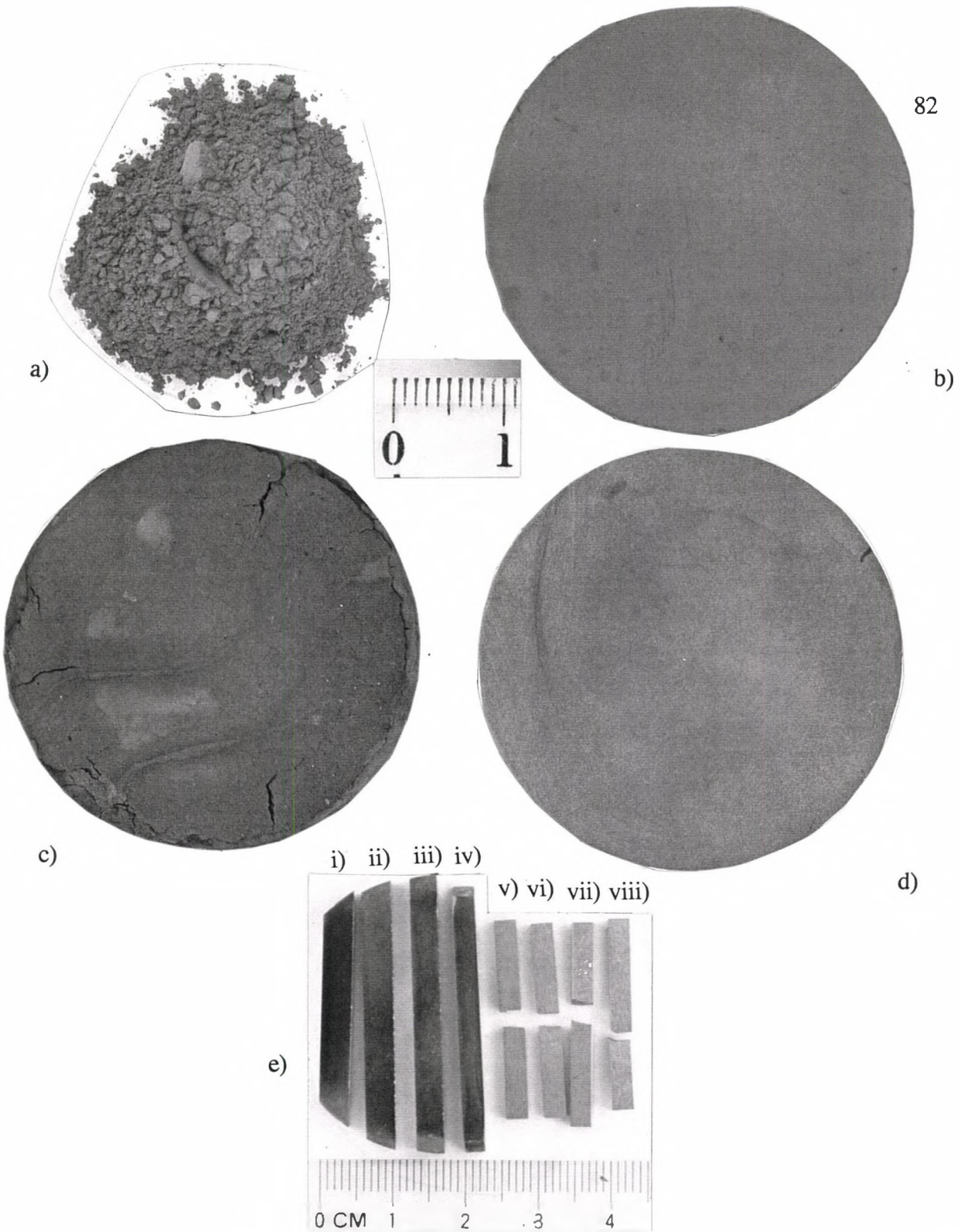

Figure 3-3: Photographs of a) powder mixture, b) pellet after consolidation, c) pellet after combustion synthesis, d) hot pressed pellet, and e) (i-iv) bars before machining, (v, vi) chevron-notched bars after testing and (vii, viii) bend bars after four-point bend test.

mixtures were ball-milled with Si_3N_4 balls in air for twenty-four hours in a polyethylene container. This procedure was to break apart the agglomerates in the powders, to create a homogeneous consistency and to further refine the particles.

X-ray analysis of the ball milled powder mixture (Figure 3-4) showed no evidence of either amorphization or compound formation. The SEM micrograph of the powder mixture is shown in Figure 3-5. The largest particles were molybdenum, the grey particles were silicon, and the darkest particles were graphite. Using stainless steel dies, each with two plungers, the mixture was uniaxially pressed with a hand press[3] into cylindrical pellets of two diameters; 1.27 cm and 3.81 cm, with applied pressures of 175 MPa and 50 MPa respectively. The typical weight, height and relative density of the former samples were about 5 g, 1.50 cm and 40%-50% of the theoretical density (TD), respectively. The latter samples were about 35 g, 1 cm and 45%-55% TD. The green density was calculated using geometric and mass measurement, while the relative density was determined by dividing the green density by the theoretical density (TD). The theoretical densities of $MoSi_2$ and SiC are 6.25 Mg/m^3 and 3.17 Mg/m^3 , respectively (Barin 1977; Vasudévan and Petrovic 1992). The theoretical densities of the composites were calculated using the rule of mixtures (Table 3-2).

The smaller diameter samples were used to measure the ignition temperature and the adiabatic temperature of the reaction. A hole approximately 1 mm in diameter and

---

[3]20 Ton Hand Press, Model C, Carver Laboratory Press, Wisconsin, USA.

a)

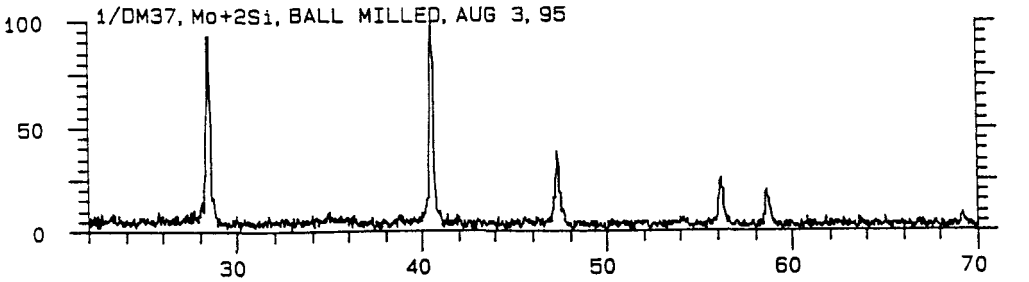

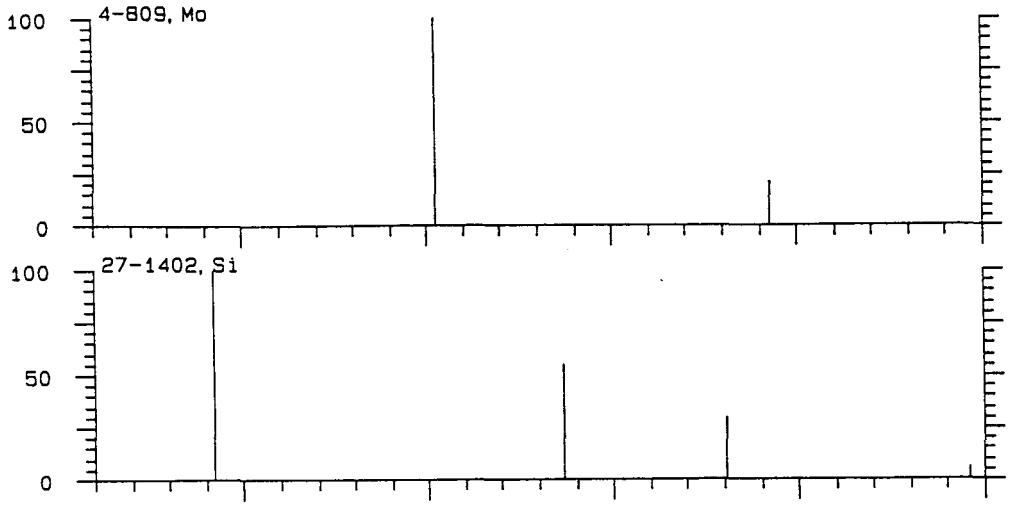

b)

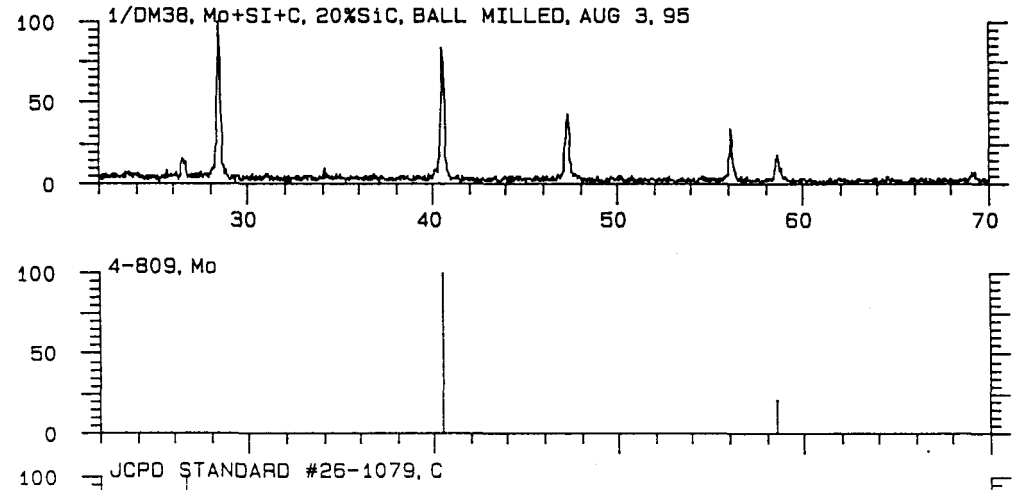

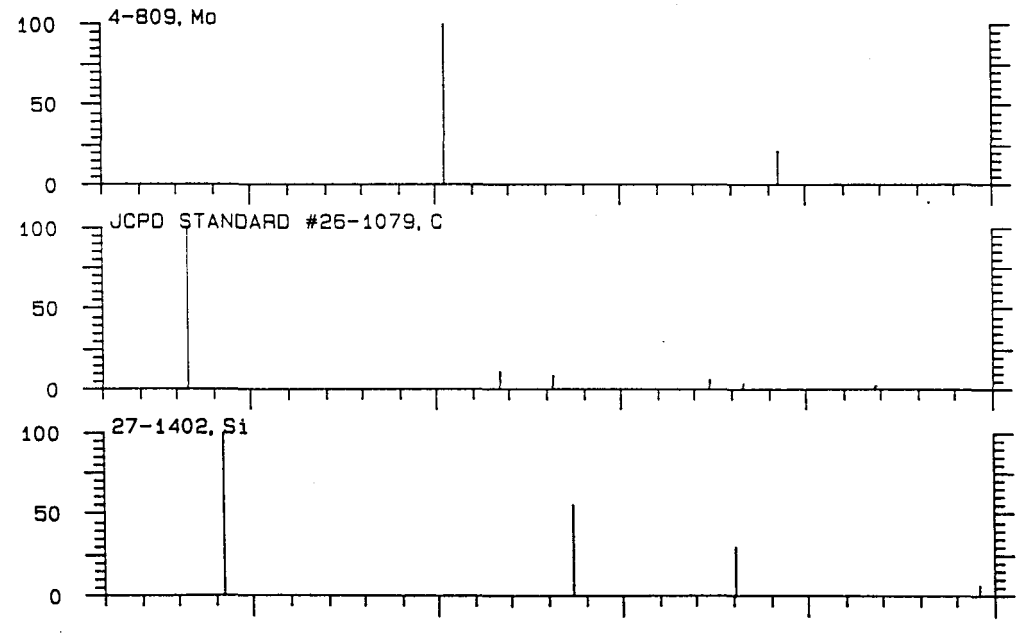

Figure 3-4: X-ray analysis of powder mixture a) Mo+Si and b) Mo+Si+C, after ball-milling in air for 24 hours.

Figure 3-5: SEM micrograph of the powder mixture (Mo+Si+C) after ball-milling in air for 24 hours.

Materials	Molar Mass (g/mol)	Density (g/cm^3)
Mo	95.54	10.22
Si	28.086	2.329
C	12.011	2.26
$MoSi_2$	152.112	6.25
SiC	40.097	3.17

Vol% SiC	Wt% SiC	Mol% SiC	Density (g/cm^3)
0	0	0	6.25
10	5.33	17.61	5.94
20	11.25	32.48	5.63

Table 3-2: Densities of $MoSi_2$, SiC and SiC-reinforced $MoSi_2$, assuming rule of mixtures.

5 mm in depth was bored into the center of one end of the sample to allow insertion of a tungsten-3% rhenium vs tungsten-25% rhenium thermocouple. The thermocouple was connected to a multimeter[4] and a chart recorder[5] that had been calibrated with a digital voltmeter[4]. The purpose of the chart recorder was to record the temperature profile of the sample during the combustion process. The multimeter was equipped to store in memory the maximum voltage attained during a specified period of time, which was recorded as the adiabatic temperature.

The first procedure attempted to achieve for combustion synthesis was to place the samples inside a sealed muffle tube in a $MoSi_2$ furnace[6], turn on a mechanical vacuum pump for one hour until a pressure of 0.1 atm was reached, then heat the furnace to 1550°C at 10°C/min. This is the thermal explosion mode of combustion synthesis. The temperature profile for the combustion of $MoSi_2$ is shown in Figure 3-6. The ignition and adiabatic temperatures were 1390°C and 1600°C, respectively.

The above procedure was inefficient and time consuming, since the furnace had to be heated up to 1550°C and cooled down to room temperature before a sample could be produced and analyzed. Therefore, the alternate procedure used was to ignite the specimens chemically with a different powder mixture, which is the self-propagating high temperature synthesis (SHS) mode of combustion synthesis. The ignition temperature of

---

[4]HP 34401A Multimeter, Hewlett-Packard Company, Colorado, USA.
[5]Fisher Recordall Series 5000, Model B5117-5I, OmniScribe Recorder, Texas, USA.
[6]1700 Series Furnace, CM Inc., New Jersey, USA.

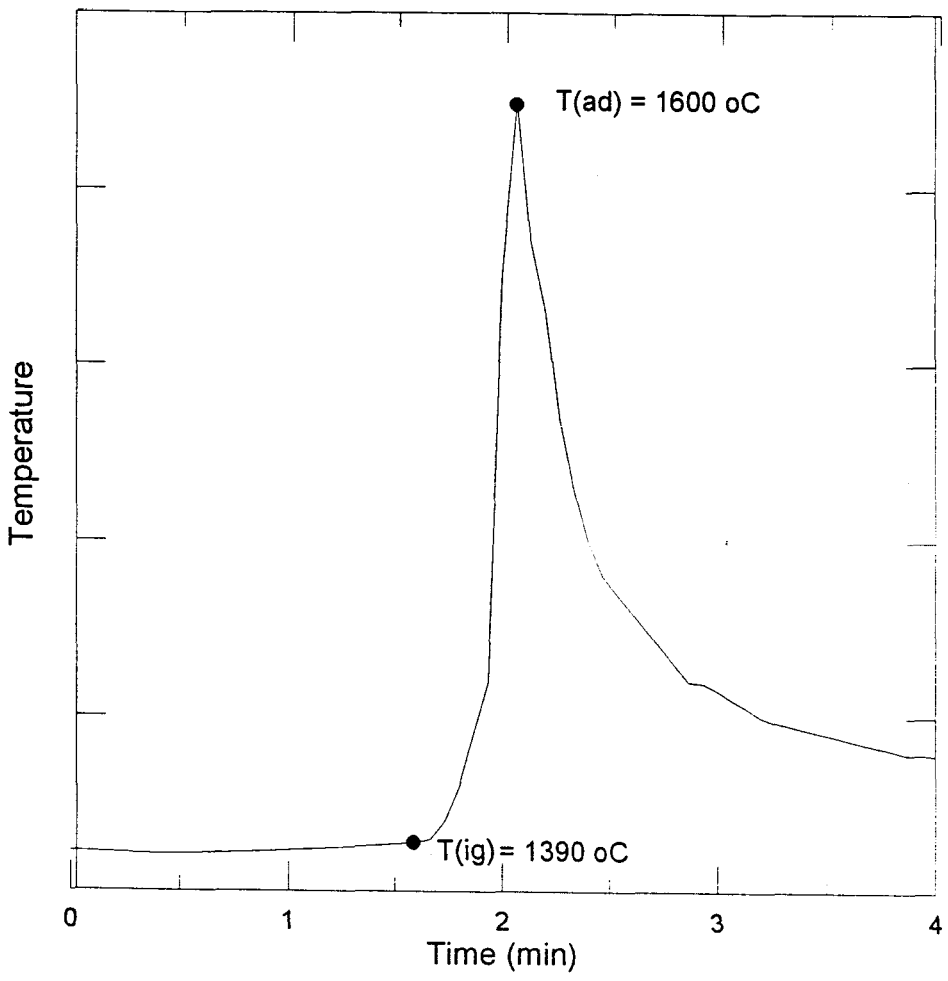

Figure 3-6: Thermogram of combustion synthesis of $MoSi_2$.

this ignitor must be as low as possible, while the adiabatic temperature must be high enough to initiate the $MoSi_2$ reaction.

Yi *et al.* (1992) have produced TiAl intermetallic compounds using the combustion synthesis process. The ignition temperature of Ti+Al = TiAl reaction was the melting point of aluminum, which is 660°C, and the adiabatic temperature was 1300 °C. Coupled with the high adiabatic temperature of a TiB_2 reaction of 3190 K (Table 1-4), the Ti/Al/B mixture was chosen as the ignitor for this study. Various mole ratios of the Al/Ti/B mixture were ball-milled for 24 hours in air and pressed uniaxially into cylindrical pellets of 1.27 cm in diameter and 1.50 cm in height with an applied pressure of 175 MPa. The typical weight of the pellets were 5.00 g. The pellets were ignited in a furnace[7] at about 700 °C under a pressure of 0.1 atm. After a few trials, a mixture made of 50 mol% TiAl and 50 mol% TiB_2 was found to produce sufficient heat to initiate the $MoSi_2$ reaction. The thermogram of the combustion of the Ti/Al/B mixture is shown in Figure 3-7. The ignition temperature was 660°C and the adiabatic temperature was 1688° C. With this Ti/Al/B mixture, $MoSi_2$ and its composites can be produced at 660°C instead of 1550°C.

Specimens containing Mo+Si(+C) were then ignited with the Al/Ti/B mixture to measure the respective adiabatic temperatures. The Al/Ti/B mixture was uniaxially pressed into a disc with a diameter of 23.8 mm and a thickness of 5.0 mm with an applied pressure of 30 MPa. Mo+Si (+C) compacts (1.27 cm diameter, 1.50 cm height, 5.00g

---

[7]Furnace Model 59744, Lindberg Hevi-Duty, Wisconsin, USA.

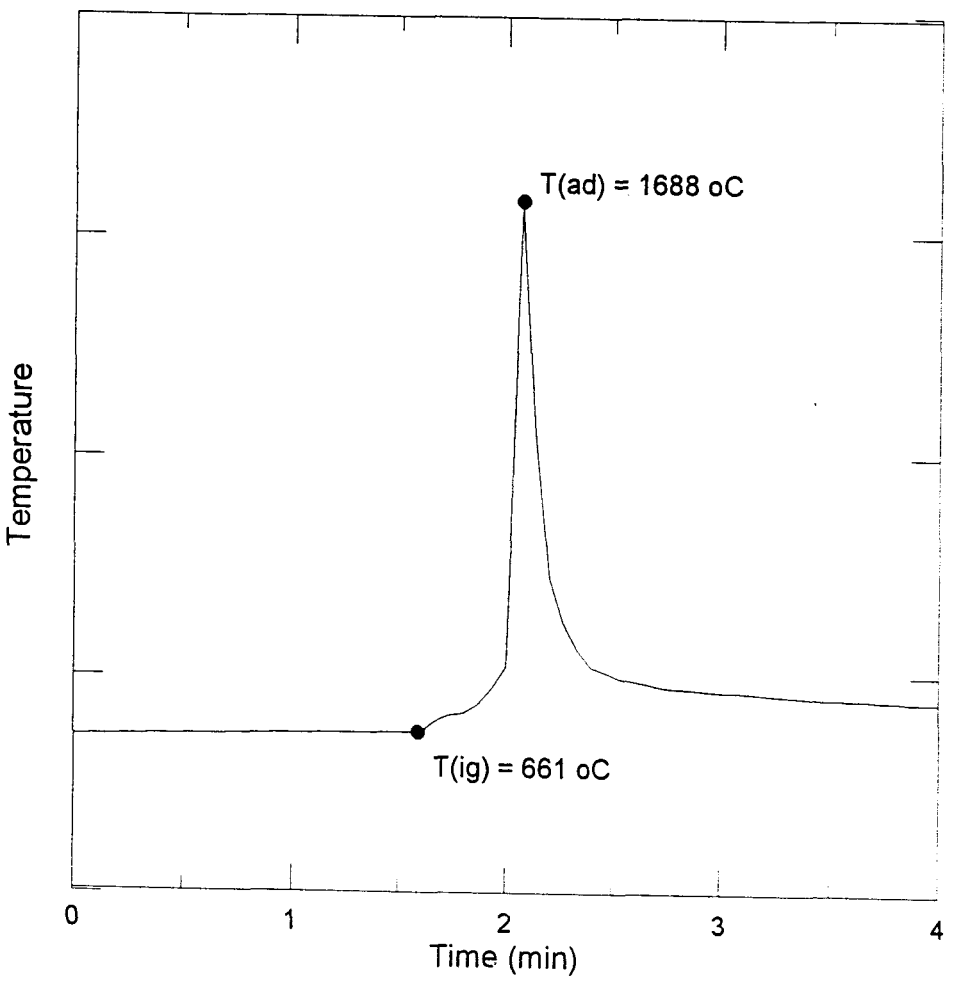

Figure 3-7: Thermogram of combustion synthesis of 50 mol% TiB_2 + 50 mol% TiAl.

weight) were placed on top of the Al/Ti/B discs and loaded into the furnace with the thermocouple embedded as before. The furnace was heated to 700°C under a pressure of 0.1 atm. The respective thermograms and the adiabatic temperatures are shown in Figures 3-8, 3-9 and 3-10. The respective adiabatic temperatures were 1591°C, 1562°C and 1550 °C.

For mechanical testing purposes, the experiments were repeated with larger diameter specimens. The cold-pressed reactants had a diameter of 3.81 cm, height of 1.00 cm and weight of 35.00 g. All were ignited with the aid of the Al/Ti/B discs.

3.3 THE CHARACTERIZATION OF COMBUSTION SYNTHESIZED MATERIALS

Some swelling and disintegration at the surfaces were observed for the combustion synthesized samples, but in general, the cylindrical shape from the green sample was retained. The densities were measured by the Archimedes method and were found to be in the range of 35-45% TD, which is lower than that of the green density. The specimens were then ultrasonically cleaned in acetone and methanol before further characterization.

Sections of the samples were analyzed for their compositions using x-ray[8] diffraction. The relative peak intensities and diffraction angles, 2θ, were compared with those prepared from JCPDS (Joint Committee on Powders Diffraction Standards) standards

[8]Nicolet X-ray Diffractometer (30 kV, 20mA, Cu K_α Radiation)

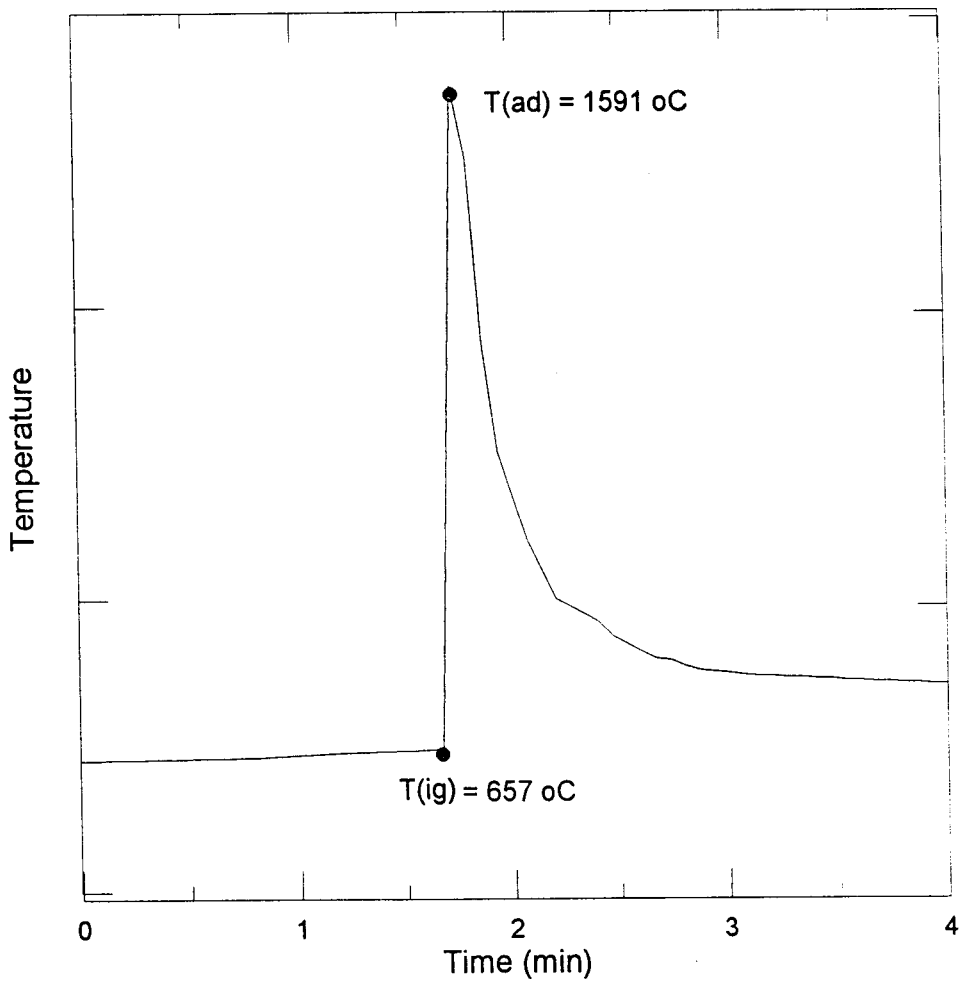

Figure 3-8: Thermogram of combustion synthesis of $MoSi_2$ chemically ignited by Ti/Al/B mixture.

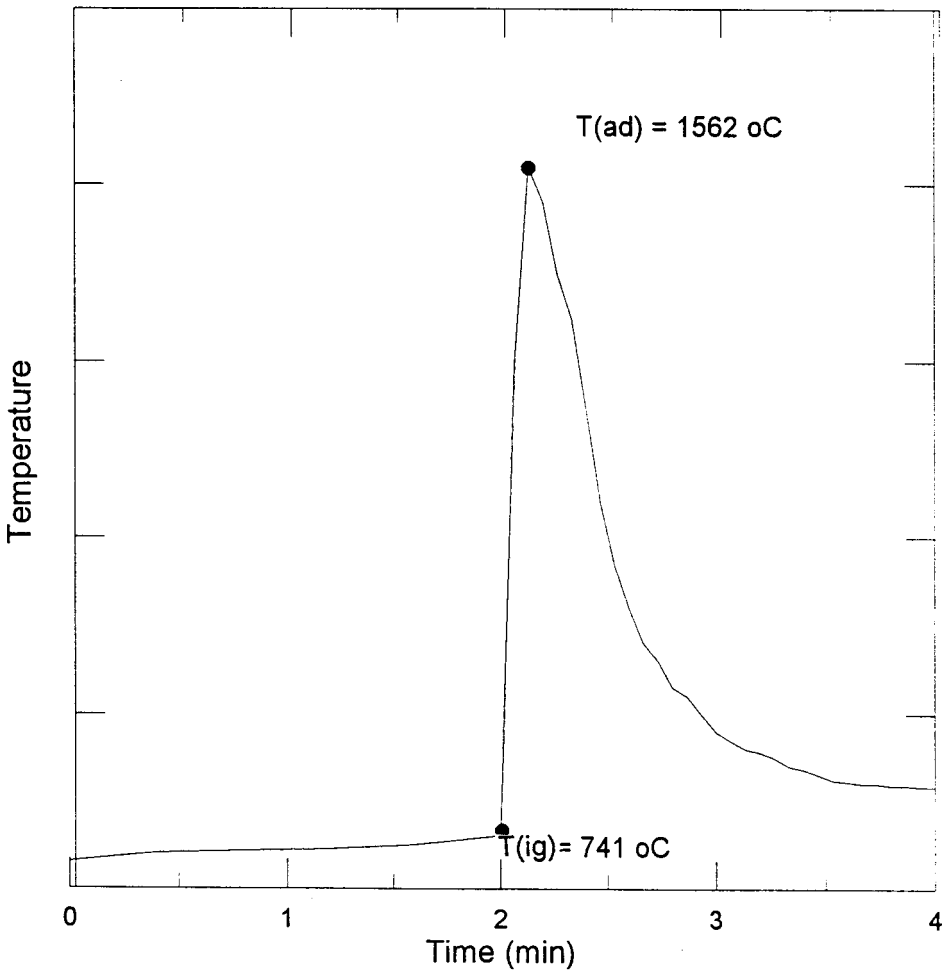

Figure 3-9: Thermogram of combustion synthesis of 10vol% SiC-$MoSi_2$ chemically ignited by Ti/Al/B mixture.

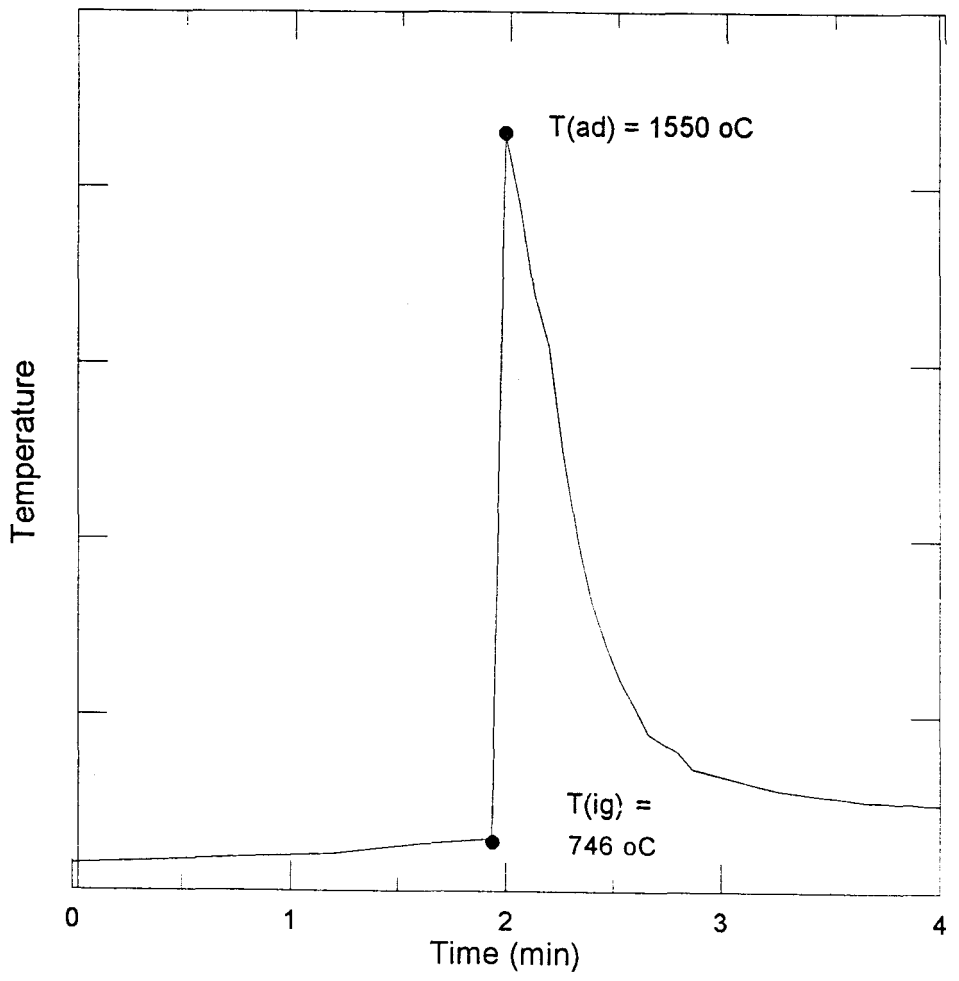

Figure 3-10: Thermogram of combustion synthesis of 20vol% SiC-$MoSi_2$ chemically ignited by Ti/Al/B mixture.

as shown in Figure 3-11 and Figure 3-12. The smaller scale of Figure 3-12 was used to confirm the presence of SiC that was too small to be detected in Figure 3-11. For the monolithic material, only $MoSi_2$ was present, while the composites contained both $MoSi_2$ and SiC. The SiC peak height increased with the SiC content in the composites. No significant quantities of other impurities were observed in these x-ray diffraction (XRD) patterns.

A scanning electron microscope[9] (SEM) was used to examine the fracture surface to determine the extent of homogeneity and porosity in the synthesized materials as shown in Figure 3-13, 3-14 and 3-15. In the monolithic material, the only distinct features observed were equiaxed and homogeneous $MoSi_2$ grains with a diameter of 5-10 μm. For the composites, two distinct features were observed: fine SiC grains of few microns diameter which surrounded larger $MoSi_2$ grains of 5-10 μm diameter.

3.4 HOT PRESSING

The samples were hot pressed[10] to increase their density. The combustion synthesized specimens were first coated with a colloidal solution of boron nitride in ethanol to prevent the diffusion of carbon from the graphite die into the samples. A graphite die

---

[9]SEM, Model 515, Phillips, Netherlands.
[10]50 Ton Hot Press, Electrofuel Mfg. Co., Toronto, Canada.

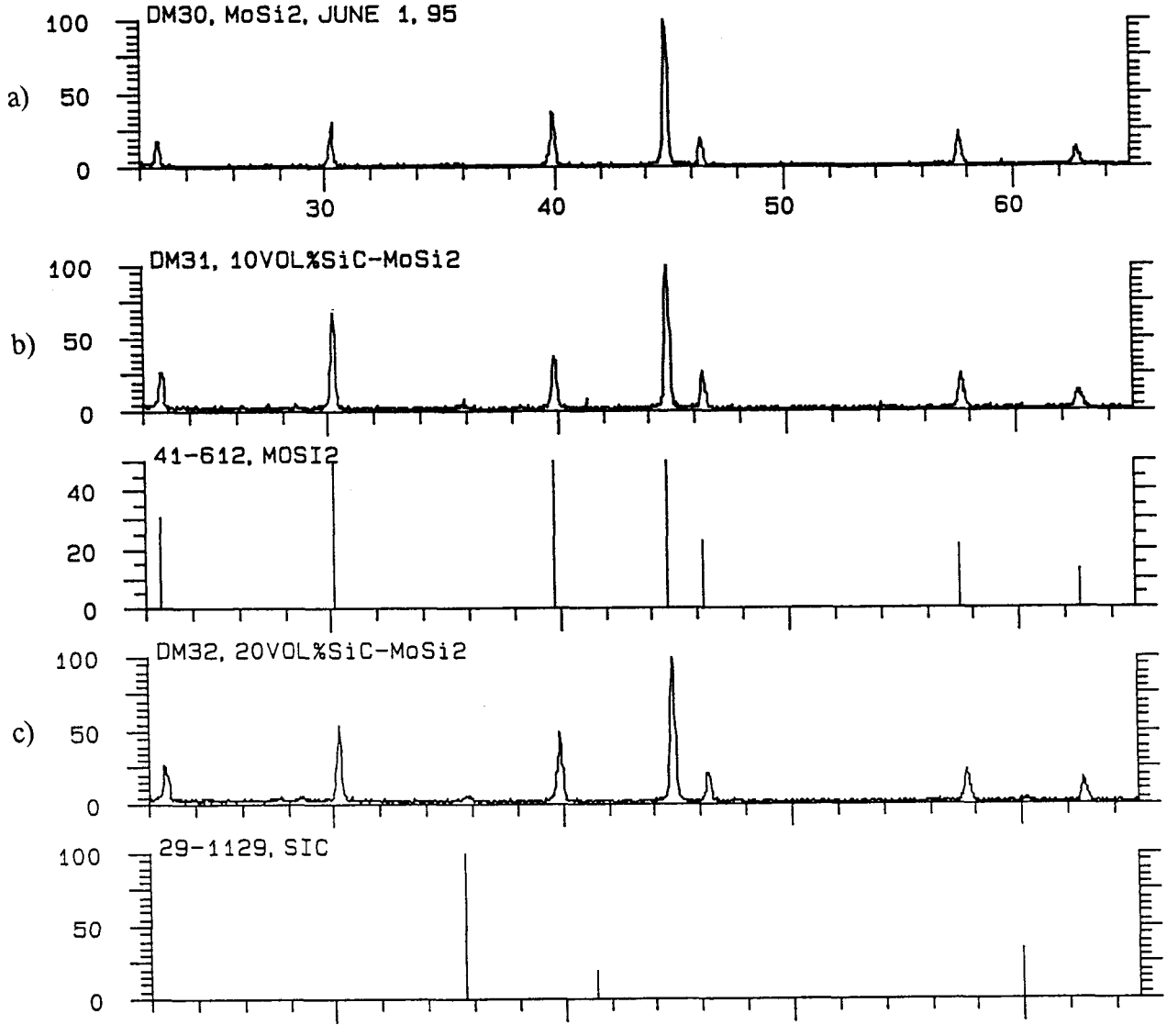

Figure 3-11: X-ray analysis of combustion synthesized a)$MoSi_2$, b)10 vol% SiC-$MoSi_2$, c) 20 vol% SiC-$MoSi_2$.

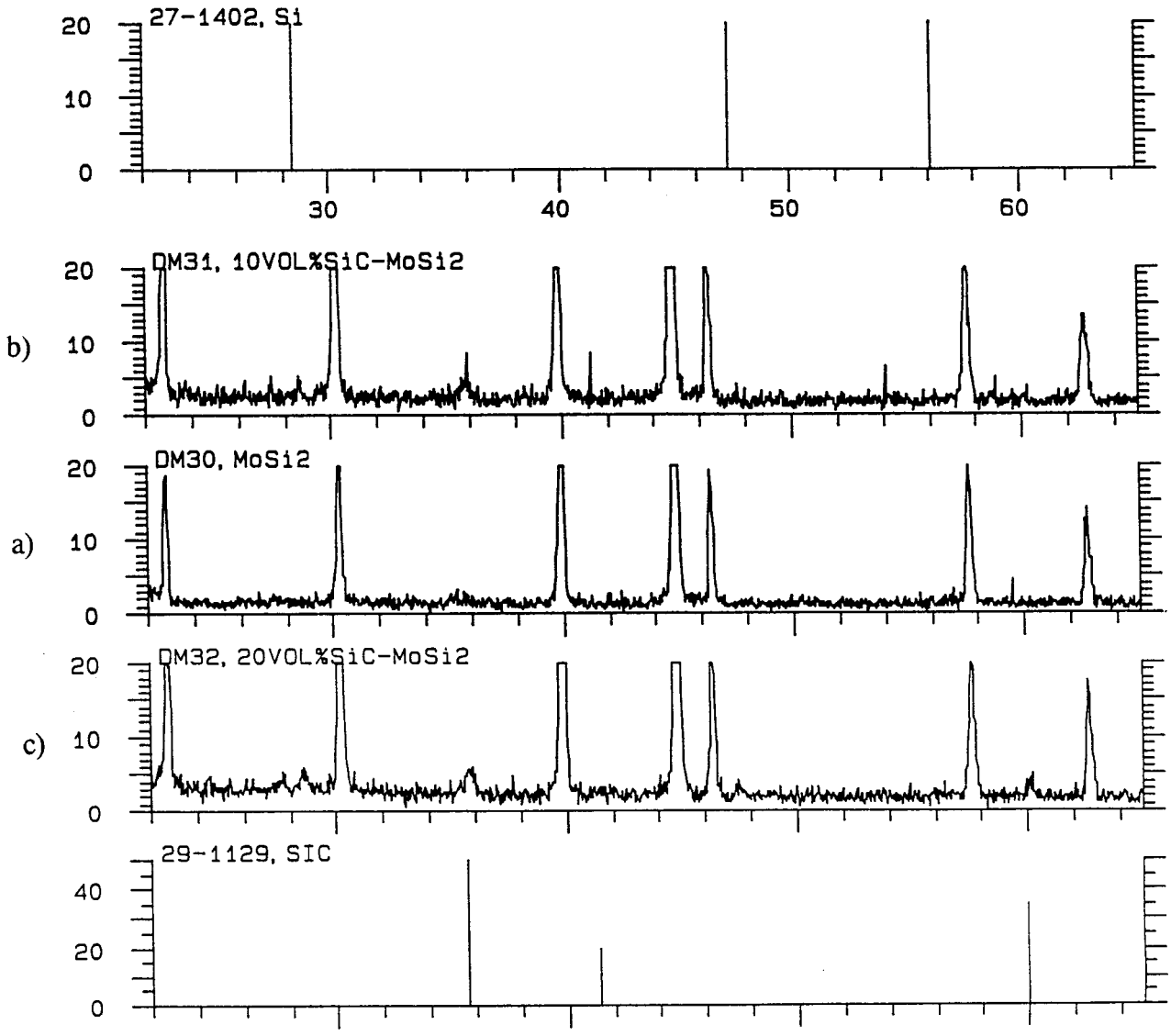

Figure 3-12: X-ray analysis of combustion synthesized a)$MoSi_2$, b)10 vol% SiC-$MoSi_2$, c) 20 vol% SiC-$MoSi_2$ (smaller scale of Figure 3-11).

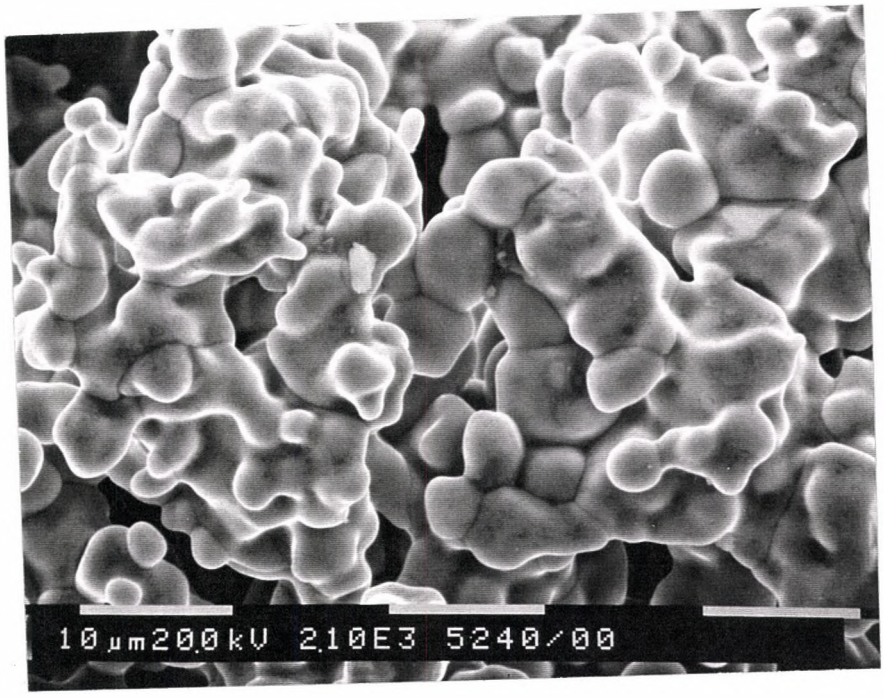

Figure 3-13: SEM micrograph of the fracture surfaces of $MoSi_2$ (secondary electron mode).

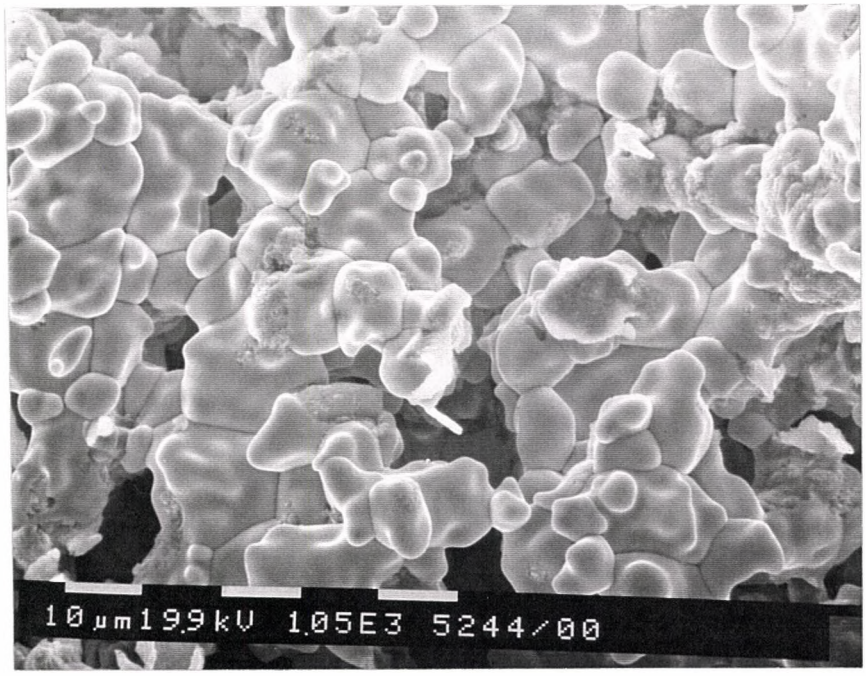

Figure 3-14: SEM micrograph of the fracture surfaces of 10 vol% SiC-$MoSi_2$ (secondary electron mode).

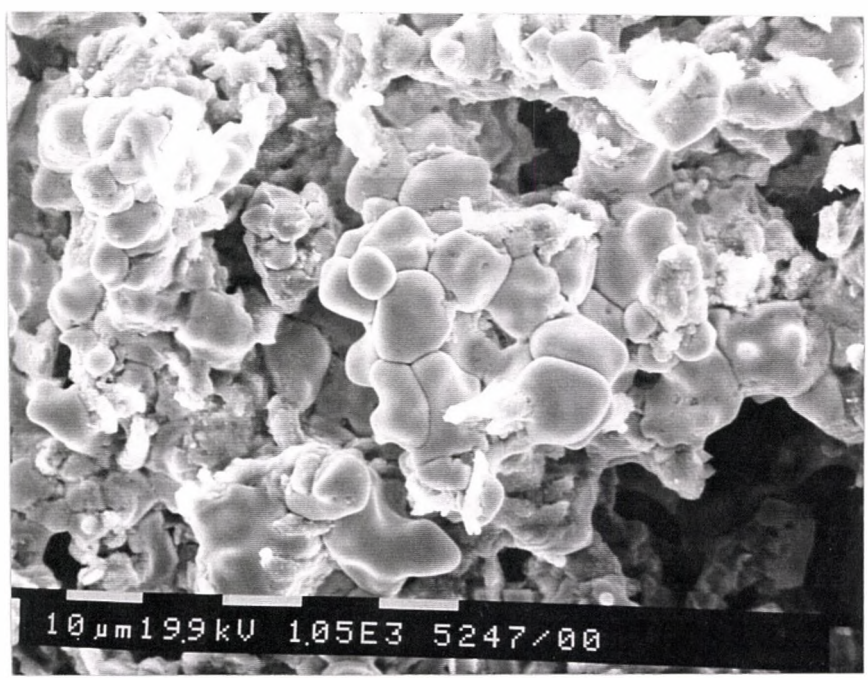

Figure 3-15: SEM micrograph of the fracture surfaces of 20 vol% SiC-$MoSi_2$ (secondary electron mode).

(1.5 inch inner diameter, 6.0 inch outer diameter and 5.0 inch height) was used in the hot pressing process. The hot pressing cycle involved a 1.5 hour ramp to a temperature of 1650°C, a 15 min soak at this temperature to ensure the homogenous distribution of the temperature, and then pressing at this temperature for another 1.5 hour at a pressure of 90 MPa. All hot pressing was conducted under a pressure of $1x10^{-4}$ atm.

Various temperatures and applied pressures were tried to obtain an optimal density of the samples. However, 1650°C was the maximum temperature of the furnace in the hot press and at an applied pressure greater than 90 MPa, the 1.5 inch graphite plungers shattered.

3.5 THE CHARACTERIZATION OF HOT-PRESSED MATERIALS

The hot-pressed samples were first ground using a 125-micron diamond embedded LECO polishing wheel, followed by grinding with a 45-micron wheel. A near mirror surface was obtained by polishing with 6-micron and 1-micron diamond paste on cloth-covered wheels, and a final polish of 0.3-micron alumina powder. Visually, the polished samples had a highly reflective silver color. All of the specimens were ultrasonically cleaned in acetone and methanol before any further characterization.

The densities were measured using the Archimedes water displacement method as

shown in Table 3-3. The hot-pressing increased the densities of the samples to the acceptable level of 97.5%-98.5% of TD. X-ray analyses of these samples to study the effect of the hot pressing on the compositions of the materials are shown in Figure 3-16 and 3-17.

The XRD patterns were qualitatively similar to those before hot-pressing, showing that hot pressing has no significant effect on the compositions of the samples, either chemically or by diffusion of carbon from the dies.

The samples were etched with a mixture of 15 vol% hydrofluoric acid, 10 vol% nitric acid and 75% distilled water and examined by SEM. The compositional phases of the samples were further analyzed by energy dispersive x-ray spectroscopy (EDX) on the SEM. To quantify the x-ray spectrum from the EDX, a single crystal of $MoSi_2$ containing some regions of Mo_5Si_3 was obtained[11]. The x-ray spectra of the $MoSi_2$ and Mo_5Si_3 single crystal, as shown in Figure 3-18, were compared to those produced from the samples. The grain sizes were determined by the circular intercept method (Hilliard 1964; Underwood 1970; ASTM E 112-88[12]) directly from the SEM micrographs of the etched cross-section taken parallel to the hot press direction.

Figure 3-19 shows the SEM micrograph of the polished surface of the hot-pressed $MoSi_2$, which shows three compositional phases, specifically, the matrix, the bright and

---

[11]Single crystal grown by P.H. Boldt of McMaster University.

[12]ASTM Designation E112-88, Standard Test Methods for Determining Average Grain Size.

	$MoSi_2$	10 vol% SiC-$MoSi_2$	20 vol% SiC-$MoSi_2$
Relative Density of Hot Pressed Material	97.0%	97.8%	98.3%
Grain Size of Matrix (microns)	21.5	14.0	12.6
Grain Size of Reinforcement (microns)	-	1-3	3-5

Table 3-3: Relative density and grain size of the hot-pressed materials.

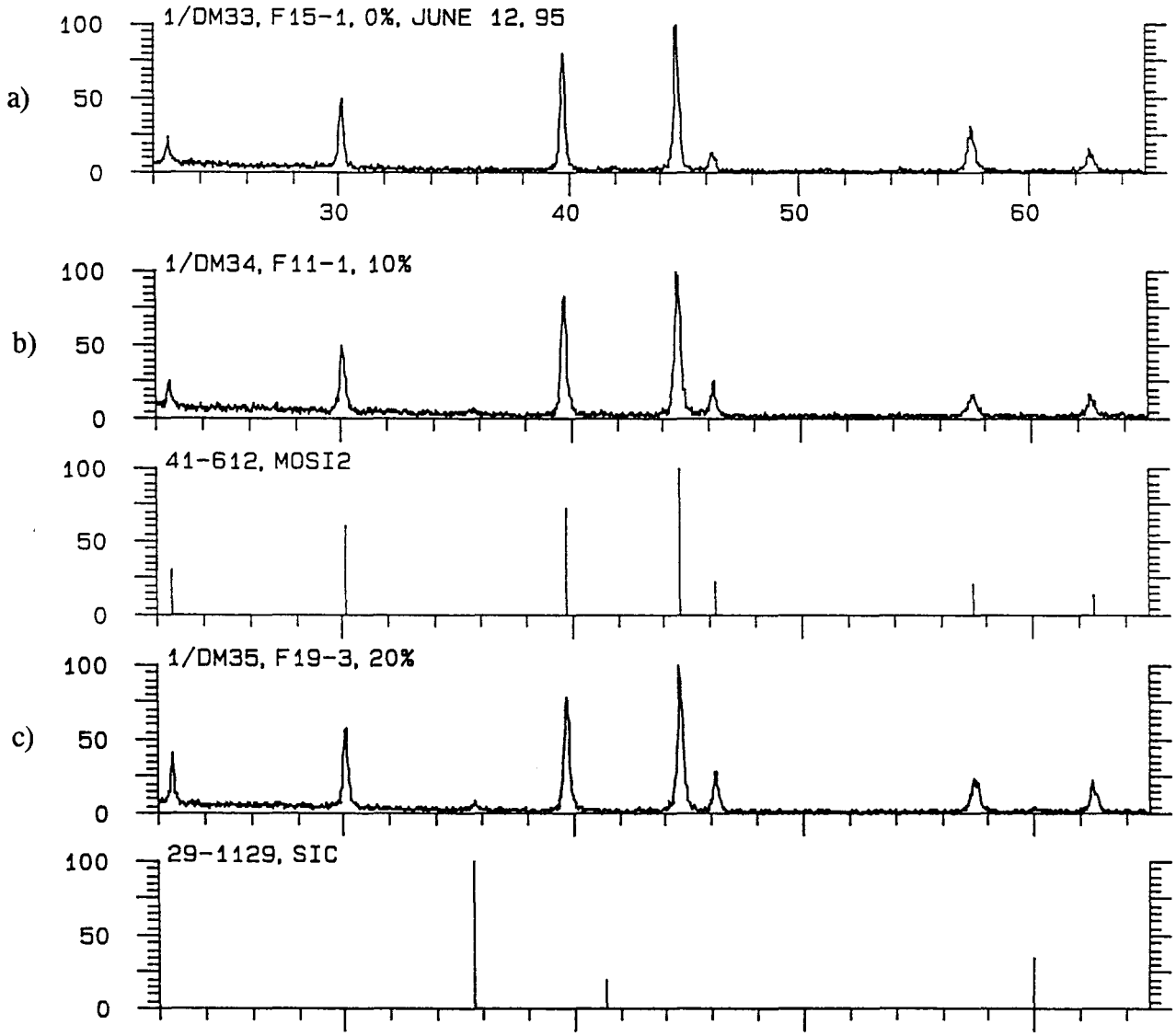

Figure 3-16: X-ray analysis of hot pressed a) $MoSi_2$, b) 10 vol% SiC-$MoSi_2$, c) 20 vol% SiC-$MoSi_2$.

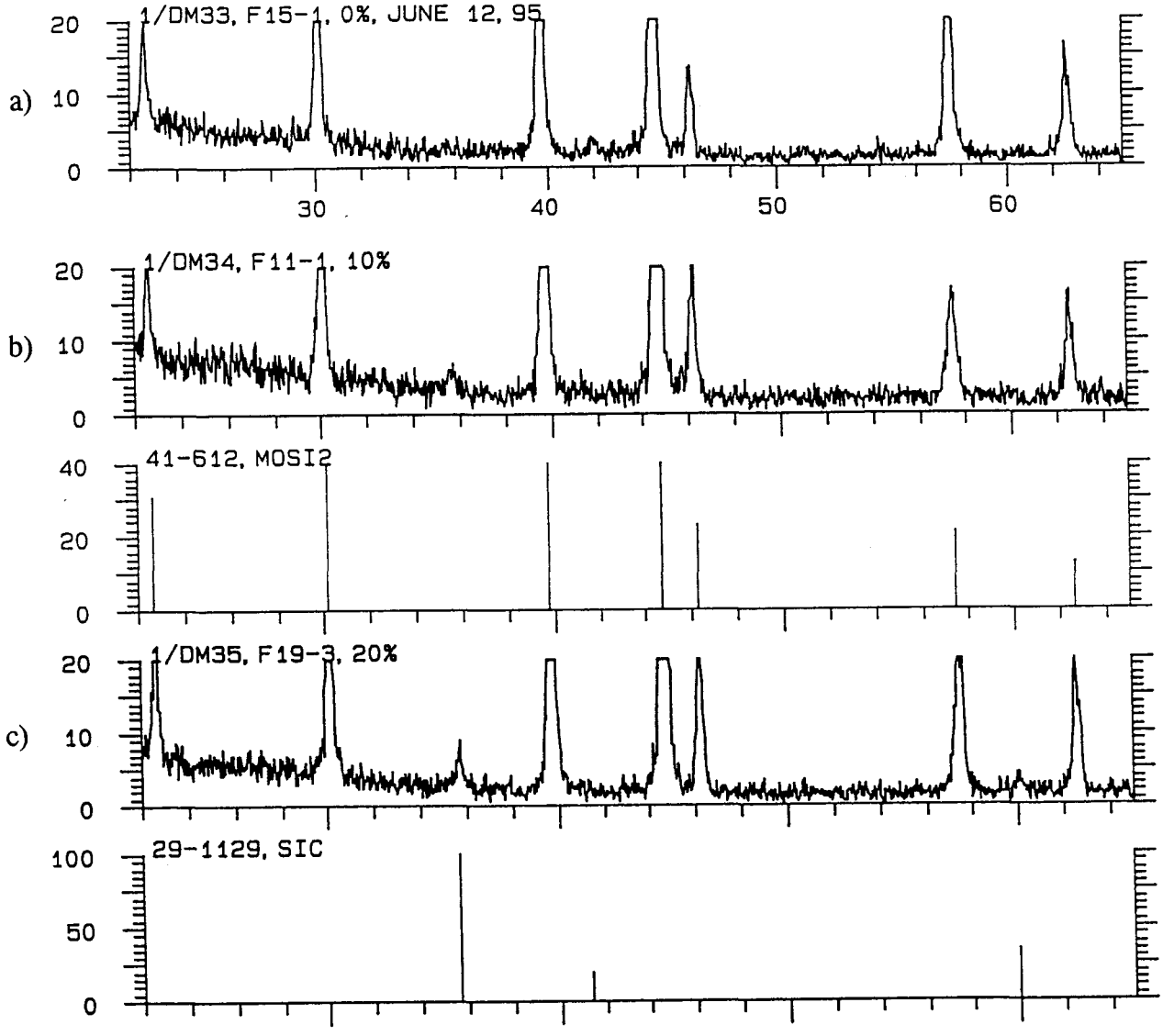

Figure 3-17: X-ray analysis of hot pressed a) $MoSi_2$, b) 10 vol% SiC-$MoSi_2$, c) 20 vol% SiC-$MoSi_2$ (smaller scale of Figure 3-16).

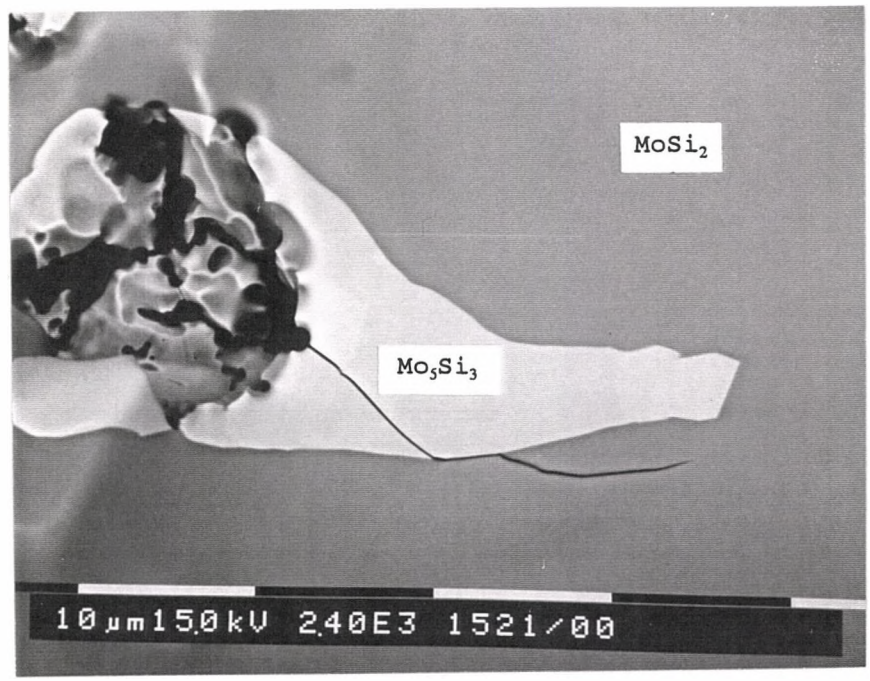

a)

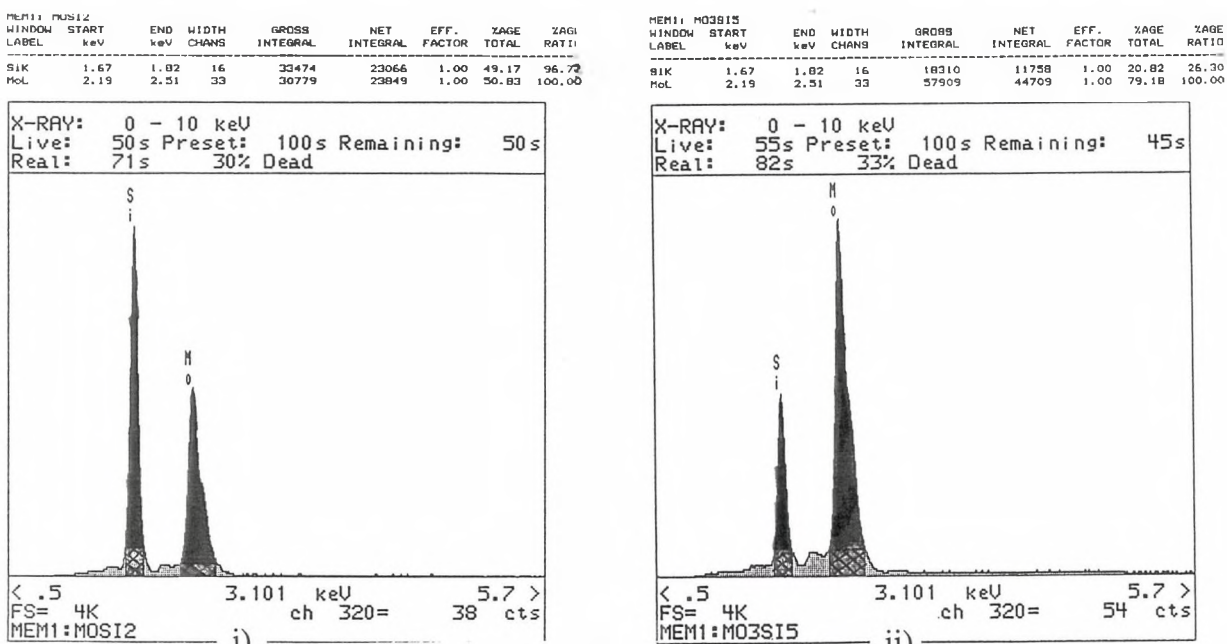

b)

Figure 3-18: a) SEM micrograph of the single crystals of $MoSi_2$ and Mo_5Si_3 (backscattered electron mode) and b) EDX pattern of the i) $MoSi_2$ single crystal, ii) Mo_5Si_3 single crystal.

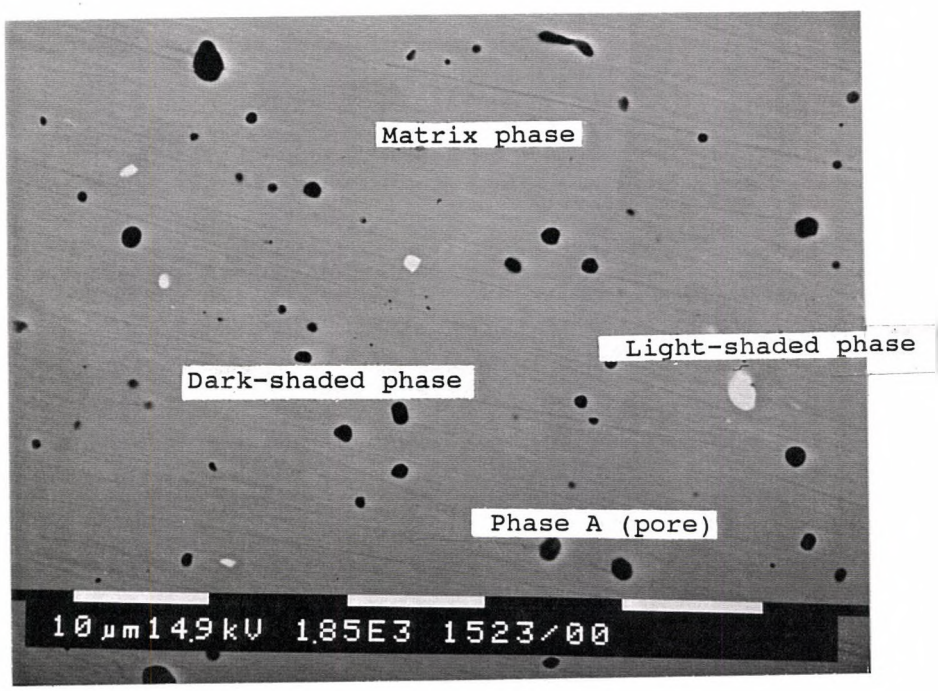

Figure 3-19: a) SEM micrograph of the polished surface of the hot pressed $MoSi_2$ (backscattered electron mode)

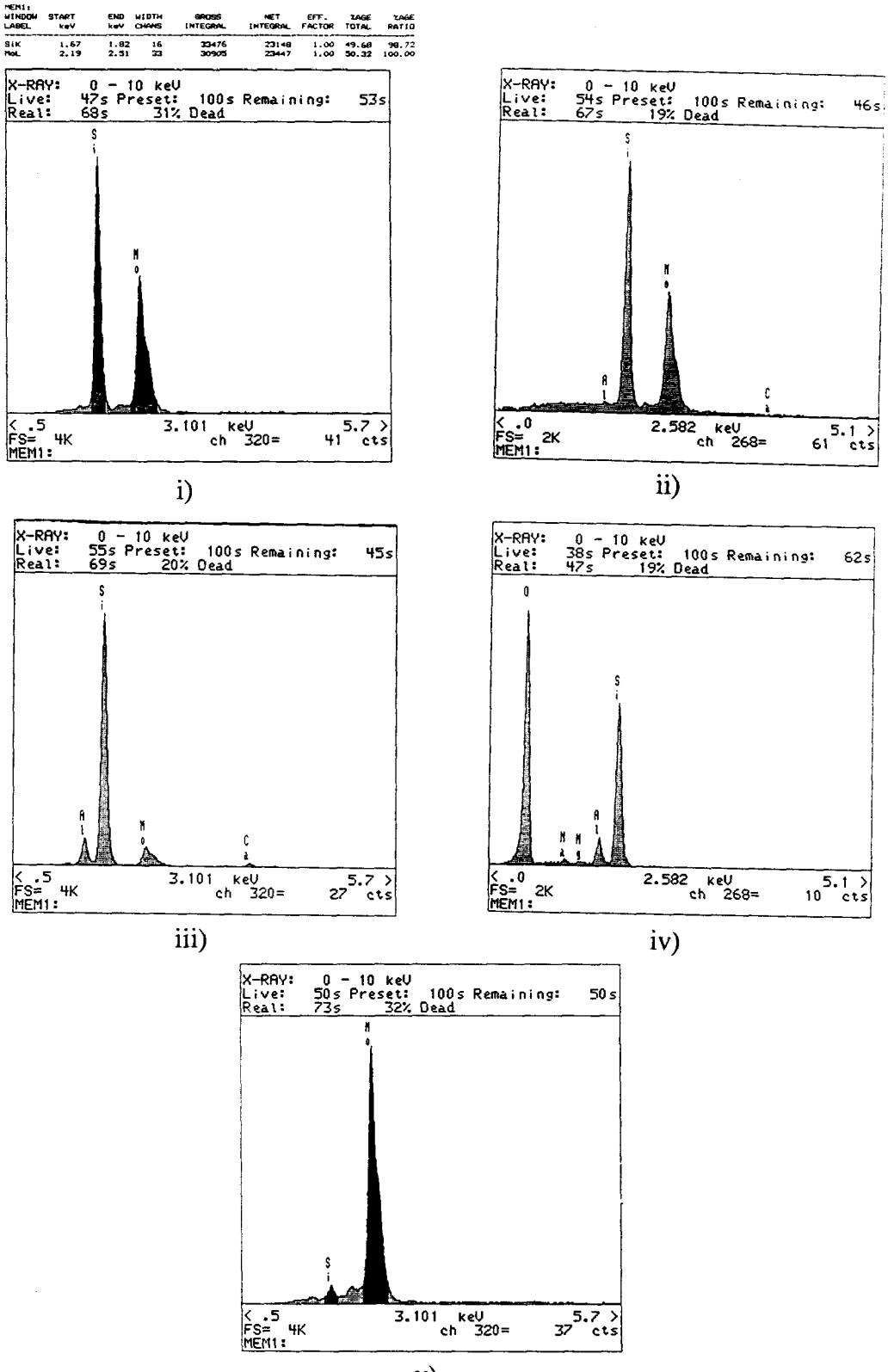

Figure 3-19: b) EDX spectrum of i) the matrix phase (without light elements detector), ii) the matrix phase (with light elements detector), iii) the dark phase (without light elements detector), iv) the dark phase (with light elements detector), and v) the bright phase (without light elements detector) .

the dark region. It was suspected that the dark region may be pores, since the specimens were not fully densified. Therefore, topographic information was acquired by picking up the secondary electrons signals which is shown in Figure 3-20. It was observed that some of the dark region were "illuminated". This phenomenon occurred because of the edging effect of the secondary electron signals, which is caused by an increase in the diffraction of the electron along the edge of the pores. It was concluded that the dark region with the "rings of illumination" were pores and the brighter the "illumination", the "deeper" the pores.

The unilluminated dark region was found to be a phase. Qualitative analysis of this region showed the presence of sodium, magnesium, aluminum, silicon, oxygen and calcium as shown in Figure 3-19. These were likely to have come from the impurities during processing and sample preparation. Additional EDX analyses were performed on the elemental molybdenum and silicon powders to determine the source of the oxygen. Elemental oxygen was not found in the molybdenum powder but it was present in the silicon powder (Figure 3-21). Oxygen was likely present in the form of SiO_2.

The matrix phase matched the EDX pattern of the standard $MoSi_2$ single crystal. Qualitative analysis of the bright region showed the presence of molybdenum and silicon, which could be unreacted Mo and Si powders. The presence of oxygen in the bright region was not investigated since oxides cause the backscattered electron image to be dark, not bright, due to their non-conductivity.

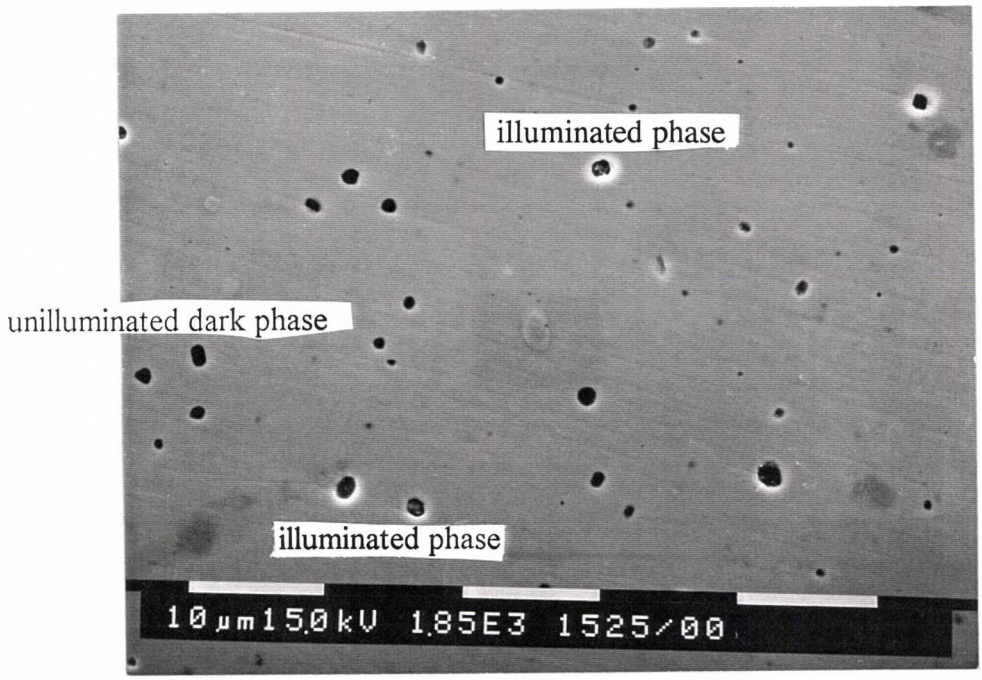

Figure 3-20: SEM micrograph of the polished surface of the hot pressed $MoSi_2$ (secondary electron mode).

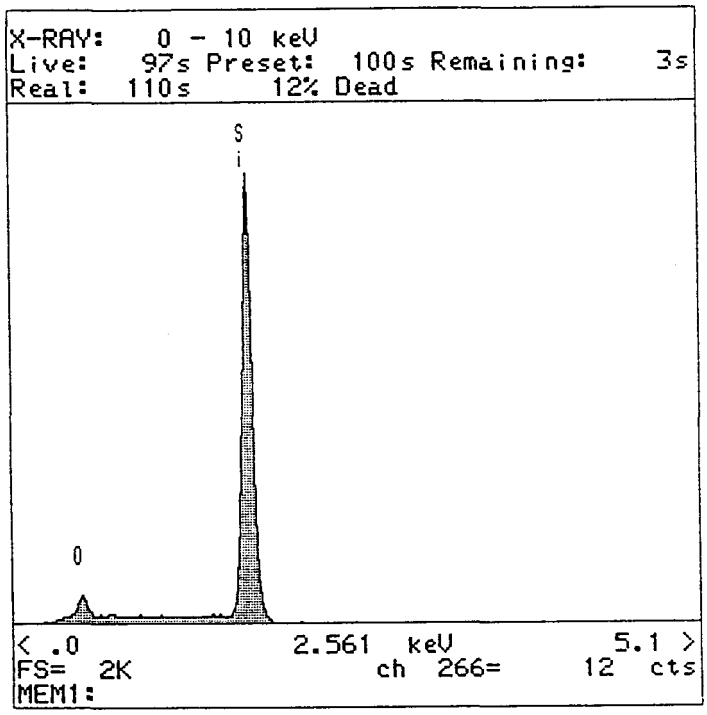

Figure 3-21:EDX spectrum of the silicon powder.

Three different compositional phases in the SEM micrograph of the polished surface of the 10 vol% SiC-$MoSi_2$ composites were identified and analyzed by EDX as shown in Figure 3-22. They were $MoSi_2$ (the matrix phase), Mo_5Si_3 (the bright phase) and SiC (the dark phase). Some of the dark phase could also be SiO_2 and porosity, since pores, SiC and SiO_2 were non-conductors and would appear to be dark in the back-scattered electron mode. The dark phase in the composites also has been reported to be $Mo_{\leq 5}Si_3C_{\leq 1}$, a Nowotny phase (Parthe *et al.* 1965), whose exact composition has not yet been determined. However, in this case, there was no indication of Mo present in the EDX spectrum; therefore, it can be concluded that this phase was not formed.

Figure 3-23 shows the etched surface of $MoSi_2$ and 10 vol% SiC-$MoSi_2$. The grain sizes of both $MoSi_2$ and SiC were measured and are summarized in Table 3.3. The SiC was distributed uniformly and homogeneously along the grain boundaries of the matrix within the composites.

The observations and the results of the polished and etched surfaces of the 20 vol% SiC-$MoSi_2$ as shown in Figure 3-24 were similar to those found in the 10 vol% SiC-$MoSi_2$, except that there was an increased amount of SiC present in these specimens, as expected. Instead of forming finer grains around the $MoSi_2$ grains as with the 10 vol% SiC-$MoSi_2$, the SiC appeared to have clustered together and formed strings of reinforcement.

In conclusion to this section, monolithic and composites of $MoSi_2$ with 10 vol%

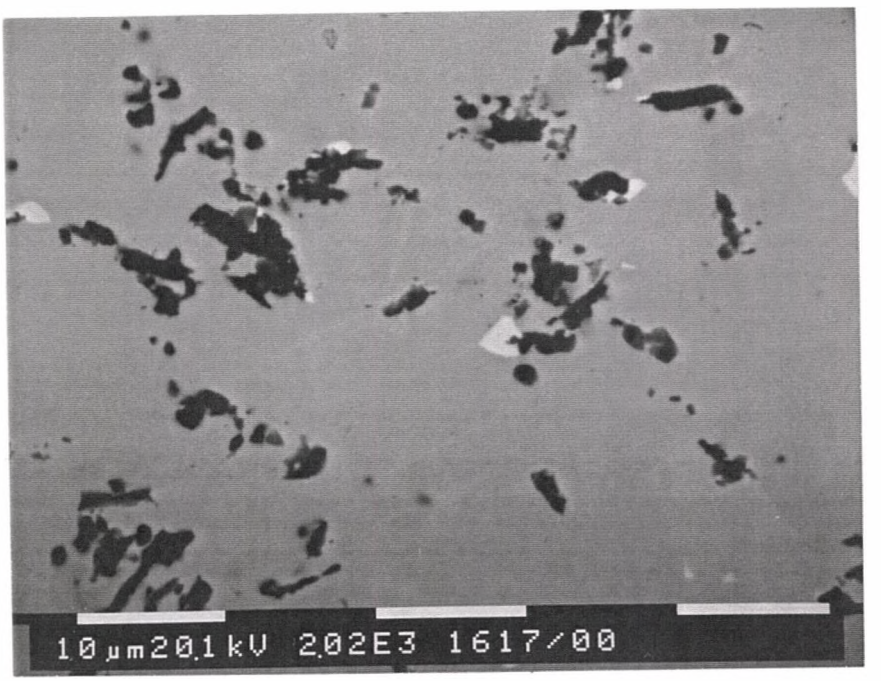

a)

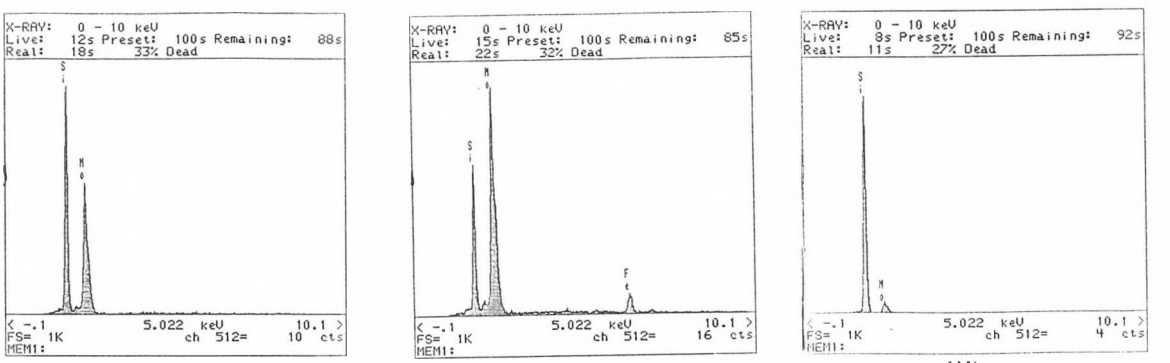

i) ii) iii)

b)

Figure 3-22: a) SEM micrograph of the polished surfaces of the 10 vol% SiC-$MoSi_2$ (backscattered electron mode) and b) EDX spectrum of i) the matrix phase, ii) the bright phase, iii) the dark phase.

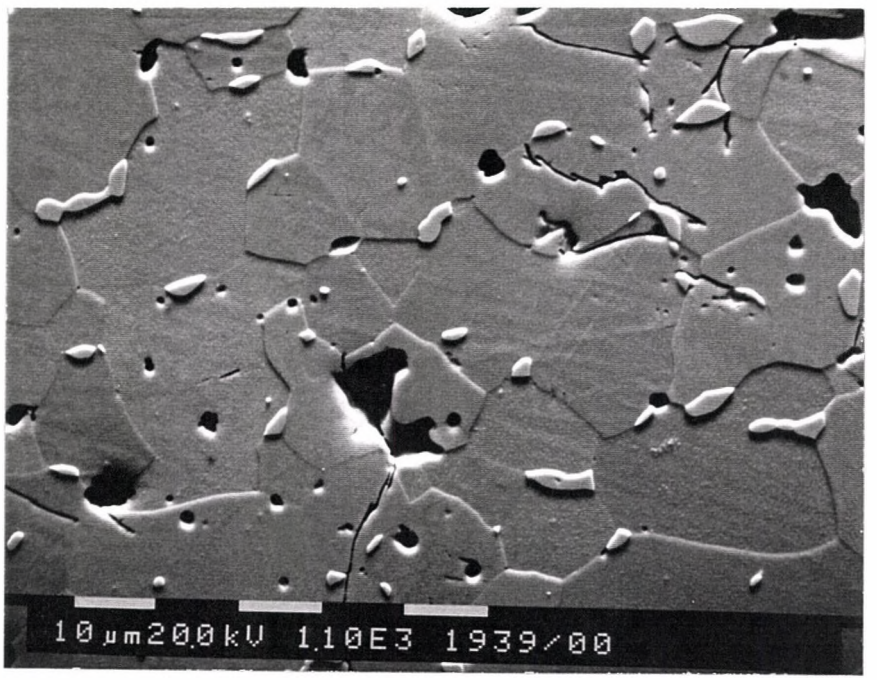

a)

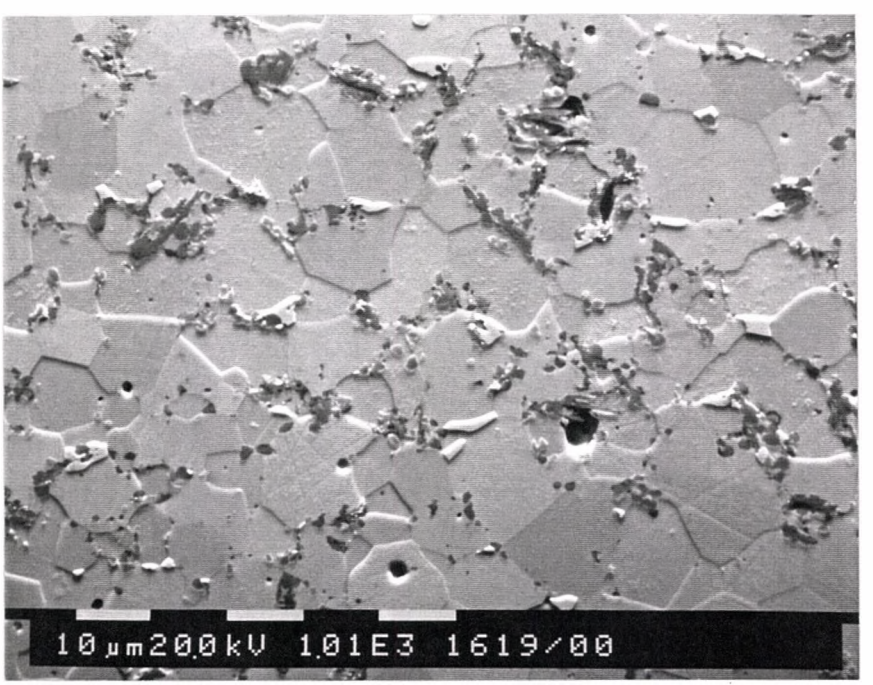

b)

Figure 3-23: SEM micrograph of the etched surface of a)$MoSi_2$ and b)10 vol% SiC-$MoSi_2$ (combination of secondary electron and backscattered electron modes).

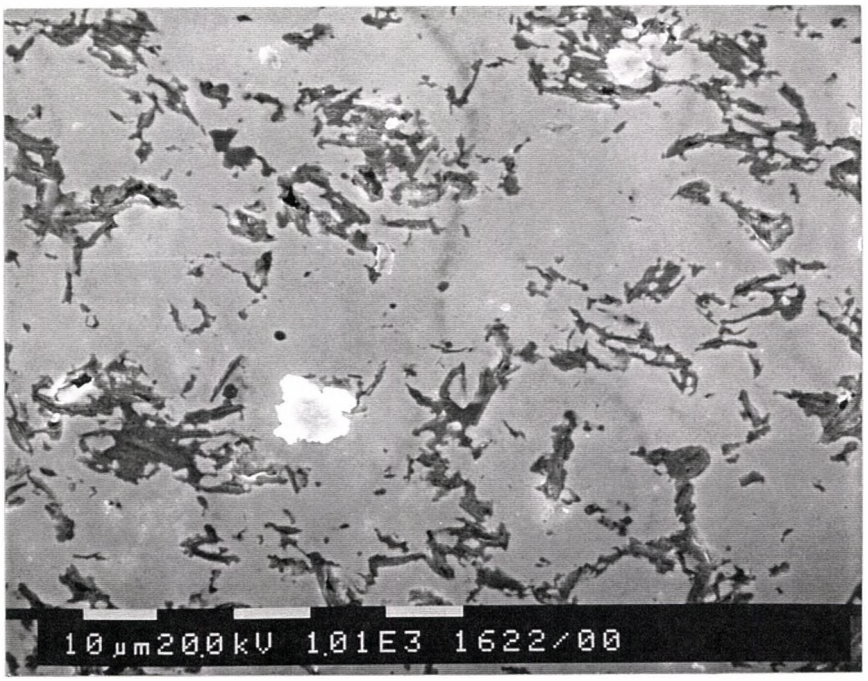

a)

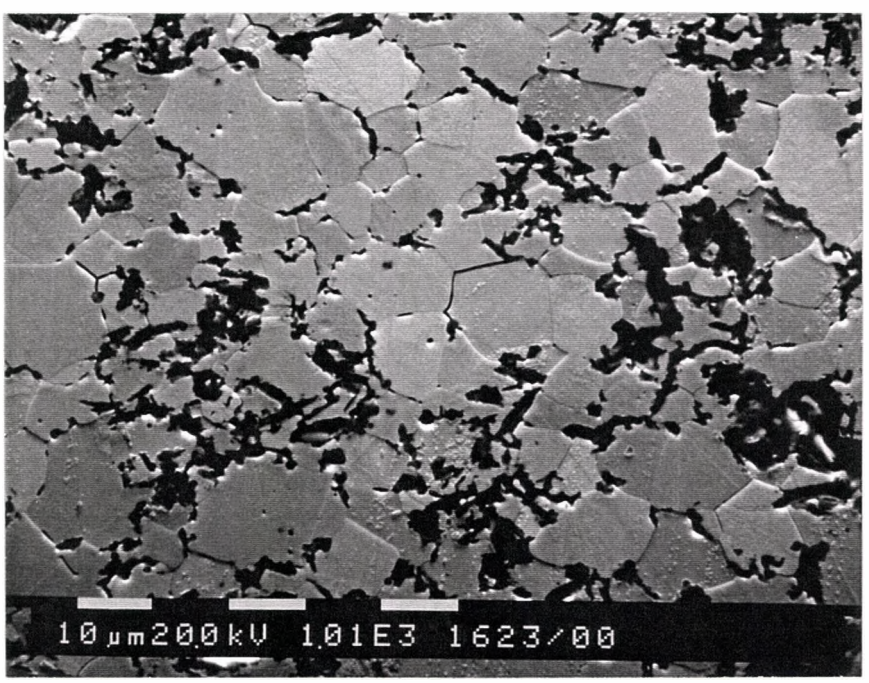

b)

Figure 3-24: SEM micrograph of a) the polished surface and b) etched surface of the 20 vol% SiC-$MoSi_2$ (using combination of secondary electron and backscattered electron modes).

SiC and 20 vol% SiC have been fabricated successfully with 2-3% porosity and with uniform and homogeneous dispersion of SiC reinforcements, through the combustion synthesis process, followed by hot pressing.

3.6 DISCUSSION

Modelling of the combustion synthesis of $MoSi_2$ system has proven to be extremely difficult because of the reactive nature of the experiments, the unavailability of the thermophysical constants (such as activation energy for diffusion) and the unknown constants in the kinetic equations (Section 1.3.3). Furthermore, these equations are based on assumptions from either the diffusion kinetic theory or the chemical reaction kinetic theory. Neither of them takes into consideration the phase changes which occur in the Mo-Si reaction where Si melts to initiate the reaction. Moreover, during combustion synthesis of the Mo-Si system, both diffusion and chemical reactions play important roles in the reaction mechanism in combustion synthesis.

Preliminary experiments on combustion synthesis of $MoSi_2$ showed that in addition to $MoSi_2$, trace amounts of Mo_5Si_3 were found as shown in Figure 3-25. The inner walls of the polyethylene container used for ball-milling was covered with residual powder. Since silicon powder ($\sim 2\ \mu m$) was finer than the molybdenum powder ($\sim 6\ \mu m$), it could easily stick to the walls of the container during the ball-milling process. This loss of silicon

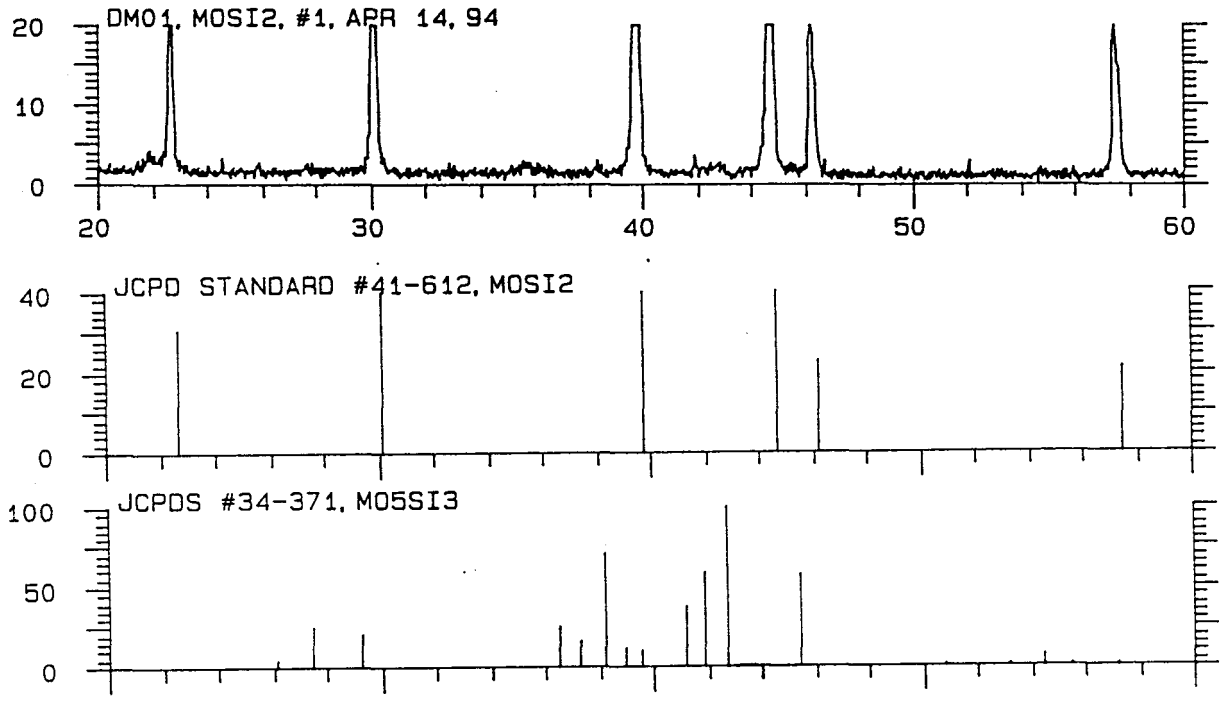

Figure 3-25: X-ray analysis of $MoSi_2$ produced in the preliminary experiment.

would lead to a Mo-rich mixture whose end product would be Mo_5Si_3 instead of $MoSi_2$, as shown in the binary phase diagram of Mo-Si in Figure 3-26 (Gokhale and Abbaschian 1989). On subsequent mixing, the same bottle was used and the problem of silicon loss was solved since the wall has already been covered by the fine powder.

As mentioned in Section 3.3, swelling and/or cracking was observed at the surface of the combustion synthesis processed samples. Some samples totally disintegrated and were discarded. The swelling and/or cracking occurred because the stoichiometric molar volume of molybdenum + silicon differs from that of $MoSi_2$ by a factor of 2.57 (Patibandla and Hillig 1993). This increase in molar volume will result in a decrease of open porosity and, if there is not enough porosity available, swelling and/or disintegration of the compact is expected. Some circumferential cracks were also observed along the wall of the cold-pressed powders. These cracks were due to the inhomogeneous distribution of pressure when the compact was uniaxially pressed and then released from the die. The cracks could also contribute to the disintegration of the combusted product. To minimize this problem, the applied pressure was maintained for a few minutes before the green compact was ejected.

The adiabatic temperatures for combustion synthesis of $MoSi_2$, 10 vol% and 20 vol% SiC-$MoSi_2$ reactions were 1591°C, 1562°C, and 1550°C respectively. Figure 2-2 shows the theoretical adiabatic temperature of these compositions, calculated by Subrahmanyam (1993), which were approximately 2000°C, 1900°C and 1800°C respectively, assuming that the initial temperature was the ignition temperature of Al/Ti/B mixture. The deviation is due to the non-idealized adiabatic condition of the experiments. However, the results follow the trend

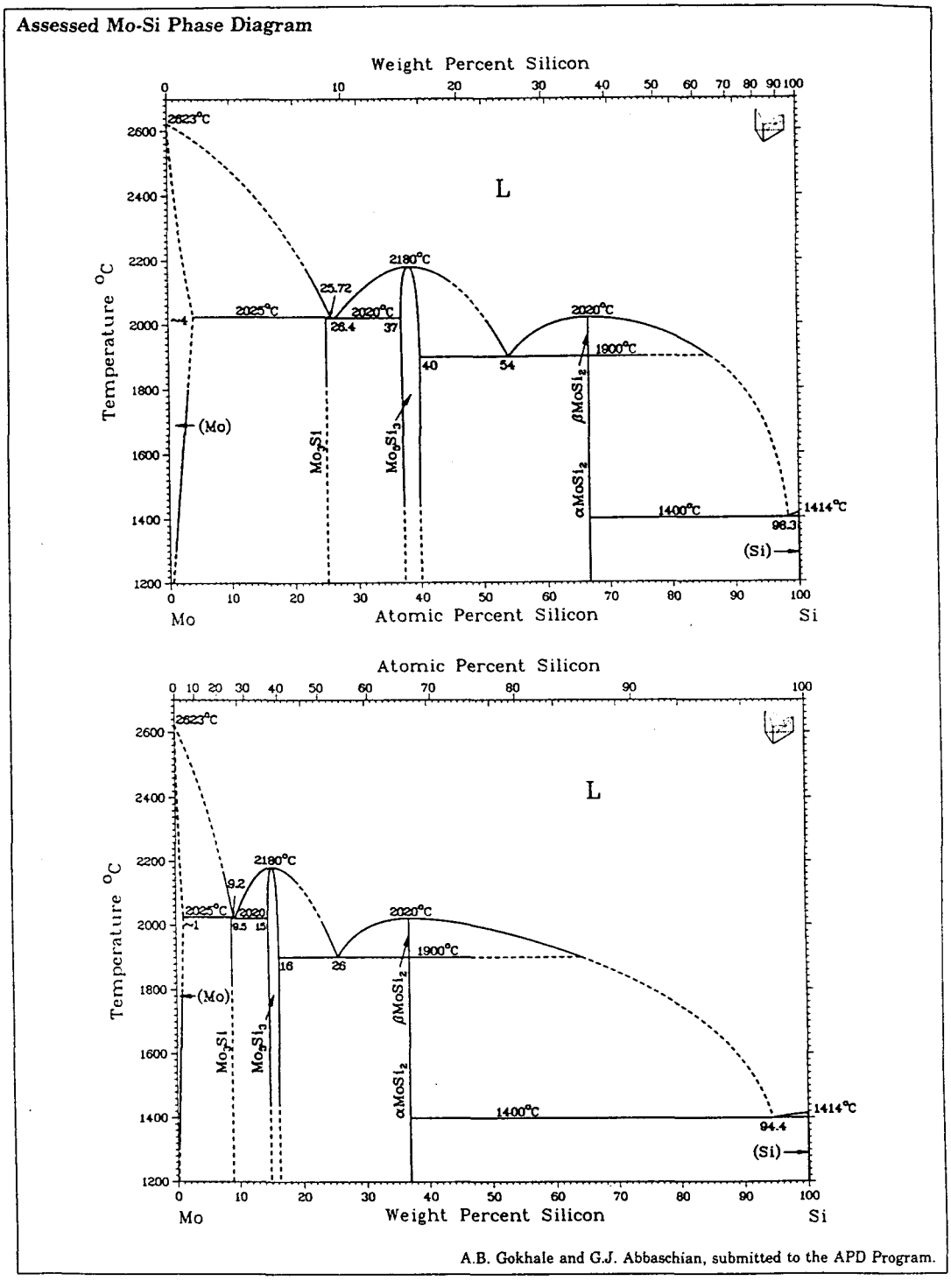

Figure 3-26: Equilibrium phase diagram of Mo-Si (Gokhale and Abbaschian 1986).

of decreasing adiabatic temperature with increasing amount of SiC. This trend is expected since the adiabatic temperature of the SiC reaction is lower than that of the $MoSi_2$ as shown in Figure 2-2.

The ignition temperature of $MoSi_2$ was measured to be about 1400°C. This temperature is very close to the melting point of silicon, which is 1410°C (DeHoff 1993). From this result, it can be concluded that the melting of silicon triggers the combustion synthesis of both $MoSi_2$ and SiC-$MoSi_2$ composites. Once silicon melts, it diffuses into the molybdenum lattice and reacts to form equilibrium phases of Mo_5Si_3 and then $MoSi_2$. Silicon, being the faster diffuser in Mo_5Si_3 and $MoSi_2$ (Baglin *et al.* 1979; Sibieude and Benezech 1989; Murarka 1983), will continue to diffuse across the $MoSi_2$ and Mo_5Si_3 layers to form more $MoSi_2$ until the Mo particles are totally reacted. Therefore, the final $MoSi_2$ should have the grain size of the Mo particles, if there is no grain growth. This whole process will take approximately 0.1-0.4 second[13], using the following approximations (Porter and Eastering 1989), and the diffusion coefficient (Ivanov *et al.* 1967) is expressed as,

$$\bar{s}=\sqrt{(D_y^x)t} \qquad (9)$$

[13] 0.1 second was calculated by using equations (9) & (10), while 0.4 second was calculated by using equations (9) & (11).

$$D^{Si}_{Mo_5Si_3} = 2.2\times10^{8}\exp\left(\frac{-63{,}000}{T}\right) \qquad \textbf{(10)}$$

$$D^{Si}_{MoSi_2} = 0.8\exp\left(\frac{-28{,}800}{T}\right) \qquad \textbf{(11)}$$

where $\bar{s}$ is the mean diffusion distance (m) [half particle size of Mo powder ~ 3 μm], t is the time (s), D_y^x is the diffusion coefficient of x in y ($cm^2 \cdot s^{-1}$), and T is the temperature (K) [adiabatic temperature = 1900 K].

This two-step reaction mechanism was observed for most silicide reactions, including the diffusion experiment of Si in Mo (Brewer *et al.* 1980), in high energy ball-milling of Mo and Si (Ma *et al.* 1993), and vapor infiltration of Si vapor into a Mo compact (Patibandla and Hillig 1993) as shown in Figure 3-27. If there is an insufficient amount of silicon available, the end product will be $MoSi_2 + Mo_5Si_3$, as observed in the preliminary results. On the other hand, if the reaction is half completed, the end product will be $MoSi_2$, Mo_5Si_3 and unreacted silicon. This end product was observed in the samples when the propagation wave was extinguished half-way through the experiment as illustrated in Figure 3-28. However, these results do not agree with results obtained by Deevi (1991, 1994). As mentioned in Section 2.1, in half-reacted samples, he found only $MoSi_2$ in the reacted portion, molybdenum and silicon powder in the unreacted portion and no intermediate Mo_5Si_3 phase. This led him to conclude that $MoSi_2$ combustion was a one step process. He concluded that other factors, such as particle size, heating rate and preheating temperature would determine whether any

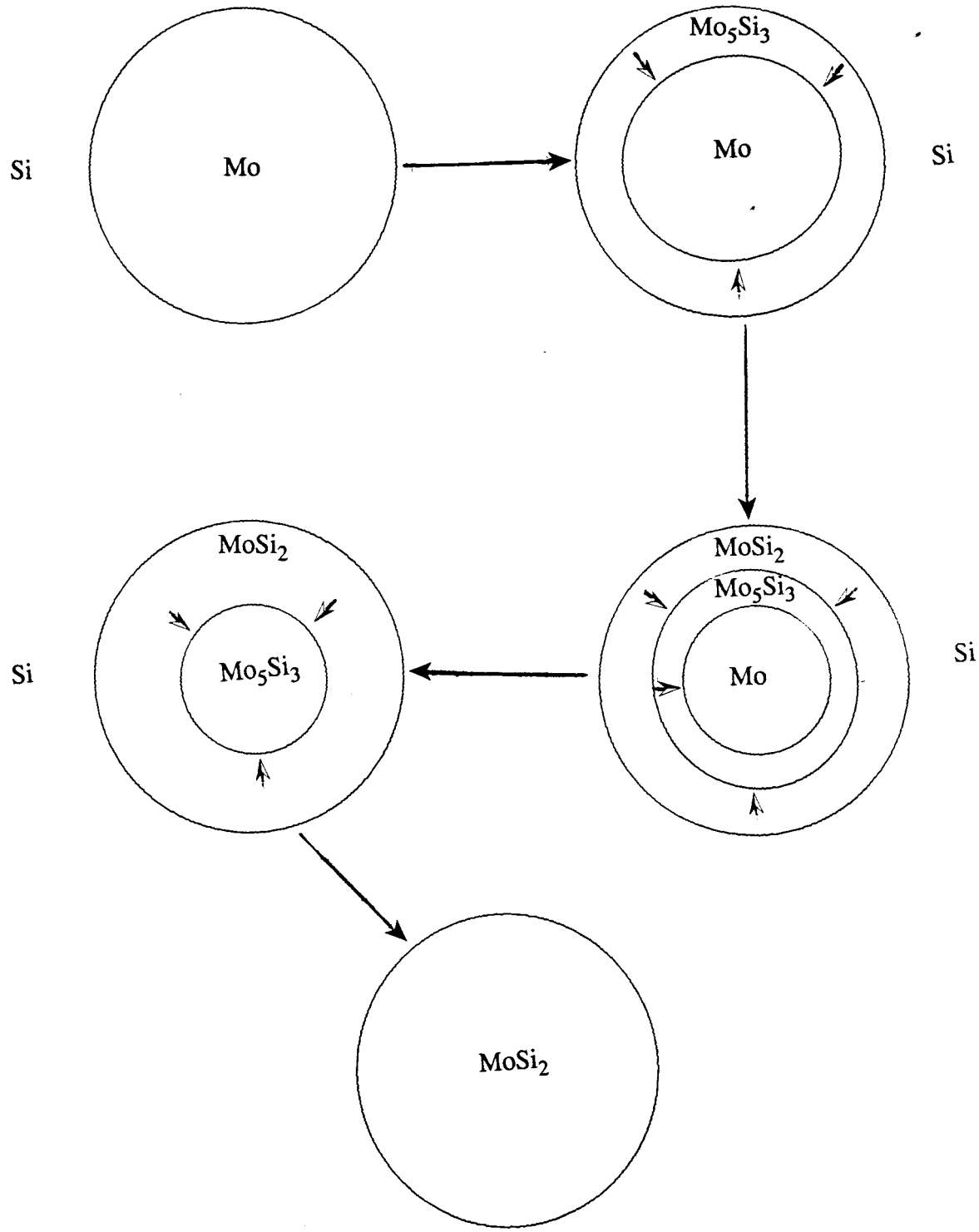

Figure 3-27: Schematic diagram of the reactive diffusional process of Mo + 2Si= $MoSi_2$.

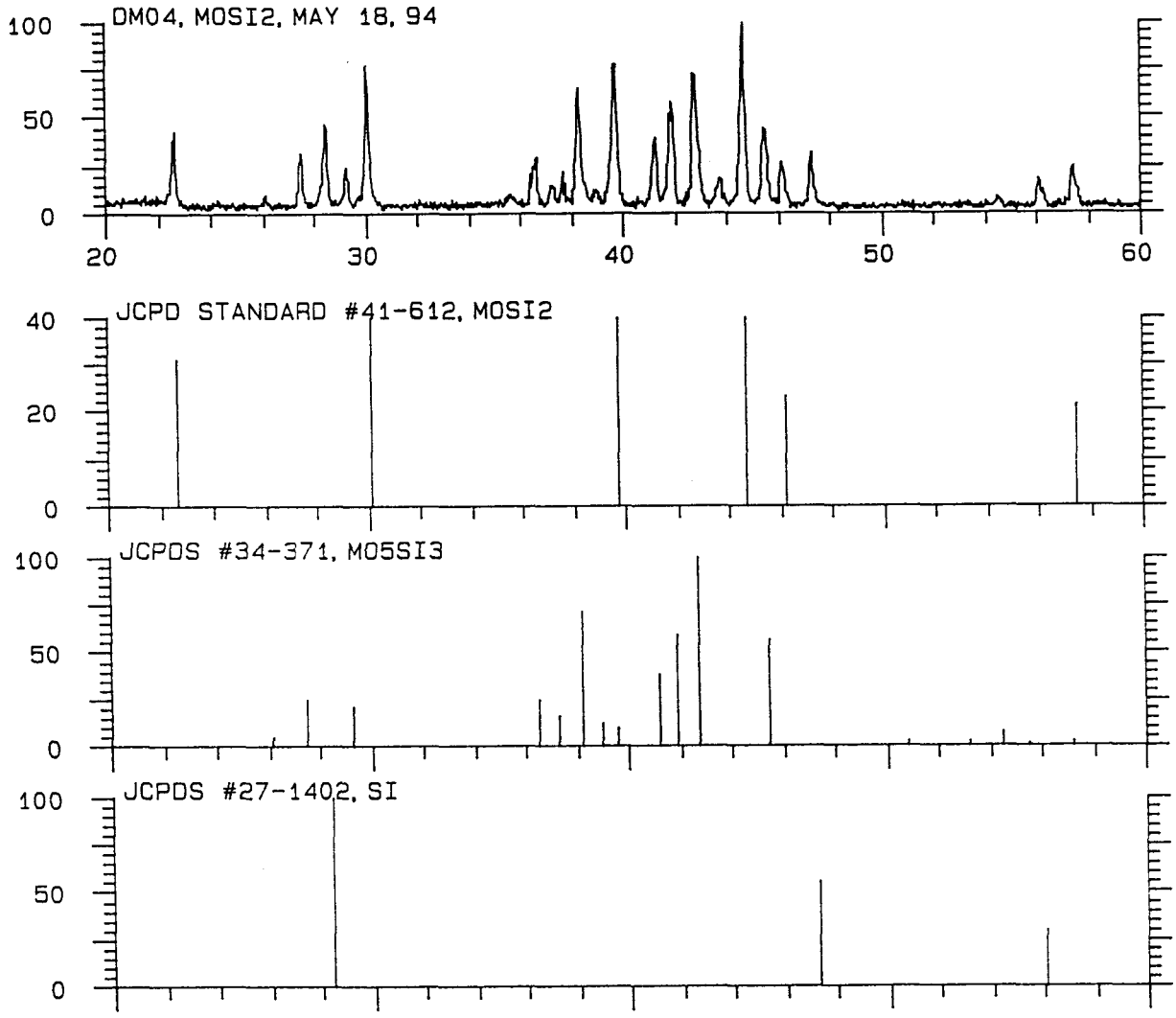

Figure 3-28: X-ray analysis of $MoSi_2$ produced from half completed reaction.

diffusional reaction had occurred prior to the melting of silicon and whether the product would be a single phase or multiphase. These factors explain the difference in results obtained in this study and that of other researchers. The only obvious difference between this study and Deevi's is the heating rate of the experiments. The heating rate used in this study was 10°C/min and Deevi's was 50 °C/min. The higher heating rate and high temperature gradient result in a higher activation energy for the diffusion of silicon which enables the Mo + Si = $MoSi_2$ reaction to be completed in a one step process.

Careful analysis of the SEM micrographs as shown in Figure 3-15 of the combustion synthesized $MoSi_2$ showed that some grains did indeed coalesce to form grains of a larger size than the expected sizes from the original powders. From the reactive diffusional mechanism mentioned above, the grain size of $MoSi_2$ should have been approximately the size of the molybdenum powder, whose average size was ~ 6 μm. This observation does not support the conclusion made by Subrahmanyam *et al.* (1994) that partial melting of $MoSi_2$ occurred and the grains coalesced to form larger ones, since the adiabatic temperature (~1600°C) obtained in this study was much than the melting temperature of $MoSi_2$ (~2000°C). The reason for the presence of larger grain was likely due to the solid state grain growth.

As for the composites, the grain size distribution of the SiC particulates was very uniform and there were more fine $MoSi_2$ grains compared to those in the monolithic materials. It was thought that liquid silicon also diffused into the carbon lattice and reacted to form SiC, since its grain size and the graphite powder size (~ 3 μm) were of the same order of magnitude. However, partial melting of SiC could not occur as the melting point of SiC (m.p.

= 2545 °C) was much higher than the adiabatic temperature of the reaction, and hence it remained as fine particles. As the amount of SiC increased, the adiabatic temperatures decreased, less grain growth of $MoSi_2$ was possible, and more smaller particles of $MoSi_2$ were observed. Some large particle formation was also observed.

Unlike the Mo-Si system where equilibrium conditions between silicon and molybdenum resulted in the formation of compounds with well defined compositions corresponding to Mo_3Si, Mo_5Si_3 and $MoSi_2$, there is only one equilibrium SiC phase, hence the Si-C reaction is a one-step diffusional reaction process. Equilibrium phase diagrams of Mo-Si and Si-C are shown in Figure 3-26 and 3-29, respectively.

Upon examining the combustion synthesized samples (before hot-pressing) with the backscattered electron mode of the SEM, which can differentiate the compositional phases, the presence of SiO_2 was not obvious, resulting in a minimum impurity content as shown in Figure 3-13. The SiO_2 content can be minimized further if the combustion process was performed in an ultra high vacuum furnace. However, SiO_2 was observed in a representative amount of the hot-pressed specimens in Figure 3-30. The amount of SiO_2 in the composites was expected to be lower since graphite would act as a deoxidant to produce SiC (Subrahmanyam and Moham Rao 1995).

The presence of glassy SiO_2 is common in the $MoSi_2$ system, and is even considered to be an "intrinsic" property of $MoSi_2$ (Cotton 1991). Despite the silica impurities, the combustion synthesis process can still produce a higher purity of $MoSi_2$ and its composites than those produced by densification, mechanical alloying and arc-melting of the commercially

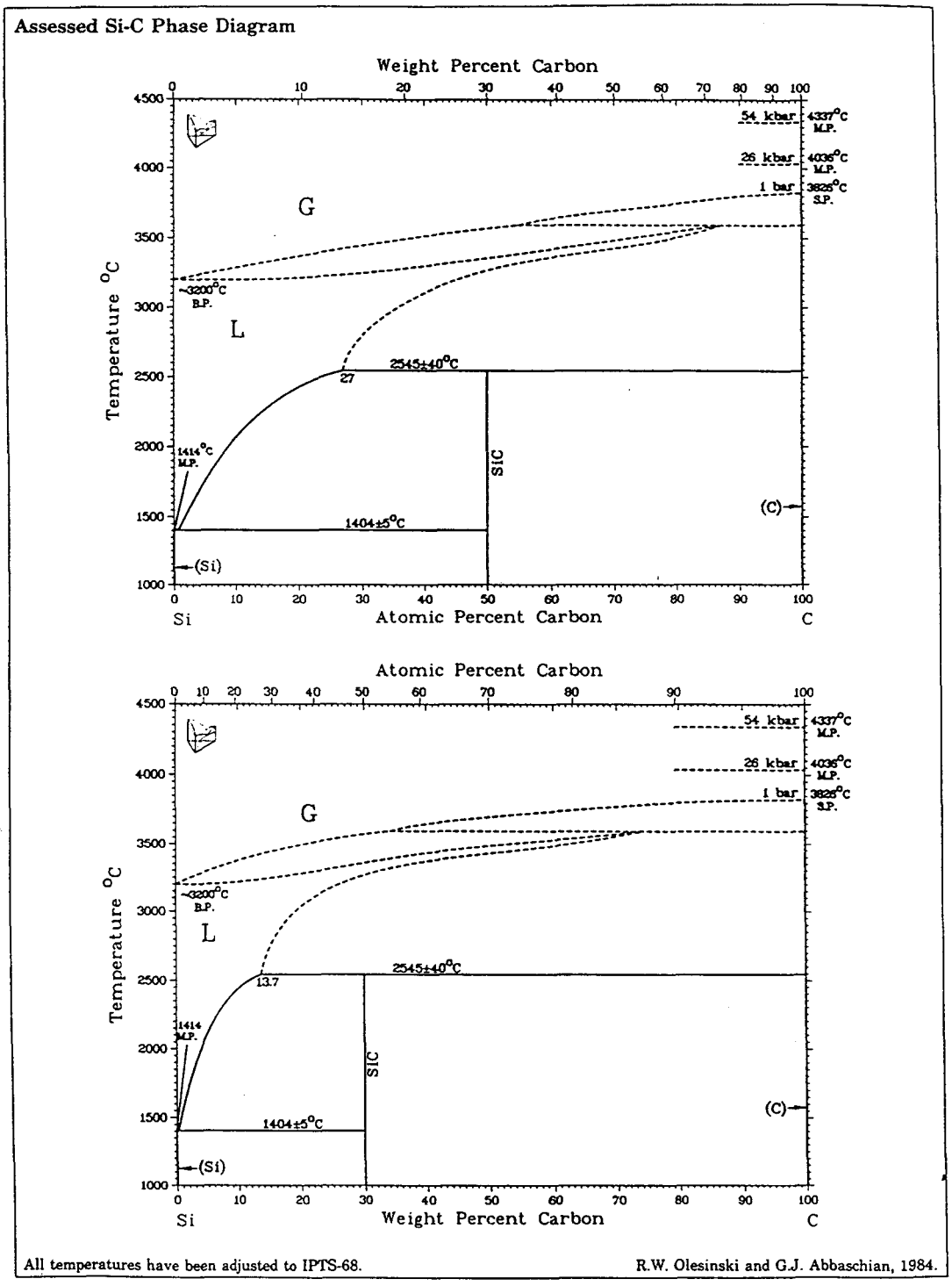

Figure 3-29: Equilibrium phase diagram of Si-C (Olesinski *et al.* 1984).

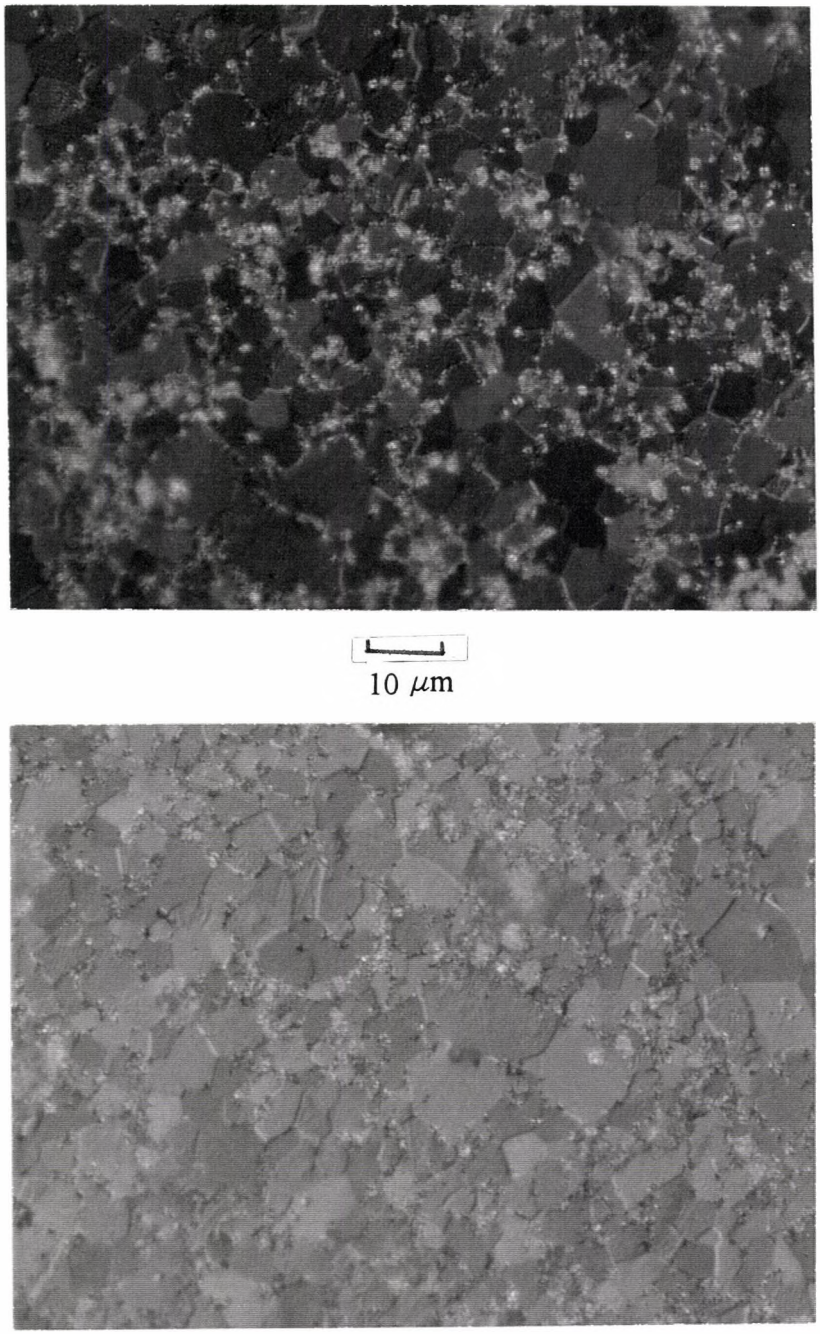

Figure 3-30: Polished surface of hot-pressed $MoSi_2$ under the optical microscope using polarized light, showing the presence of SiO_2.

available $MoSi_2$ powders (Deevi 1991, 1994). This advantage is possible because a much higher purity of the elemental powders can be obtained commercially, while the purity and powder sizes of $MoSi_2$ compounds are limited. These impurities can be detrimental on the mechanical properties of the composites as they will react with the reinforcement (Yang and Jeng 1991; Gac and Petrovic 1985)

The hot-pressing was able to increase the densities of the samples to the acceptable level of 97.5%-98.5% of TD. Grain growth in the sample during the hot-pressing was minimal. The density can be further improved by increasing the hot-pressing temperature, but at the expense of grain growth and increased content of SiO_2. The alternative method is hot isostatic pressing (HIP), but Chen (1995) reported that HIPing made little improvement in increasing the density of $MoSi_2$ and SiC-reinforced $MoSi_2$.

Some samples broke into pieces when they were removed from the hot-pressing die. This is likely due to the relatively fast cool down rate to ambient temperature. $MoSi_2$ has a non-cubic anisotropic crystal structure which results in a highly directional coefficient of thermal expansion (CTE) value; therefore, fast cooling will not permit accommodation of the thermal stresses within the microstructure, but will result in cracking.

$MoSi_2$ is usually produced by reacting the powdered elements at relatively low temperatures, typically 1200°C for many hours. The hard sintered compacts were broken up and milled to produce powdered $MoSi_2$ for subsequent processing (Weherman 1967). Therefore, the combustion synthesis process can be an alternative processing technique which

offers many advantages such as providing a product with reduced oxygen contamination (Bloshenko *et al.* 1985) and more sinterable than conventionally produced materials (Kayuk *et al.* 1978). It also has attractive industrial applications, since the temperature of the surroundings can be ambient while the time required at high temperatures is minimal.

With careful preparation, intermediate phases such as Mo_5Si_3 will not be present in $MoSi_2$ and its composites. This is encouraging because Mo_5Si_3 is not self-healing due to the low silicon contents and it will not react to form SiO_2 at high temperatures. Without this protective layer, Mo_5Si_3 is not a good high temperature oxidation resistant material (Henne and Weber 1986). Therefore, combustion synthesized $MoSi_2$ can be produced and used without loss of thermal, electrical, and self-healing properties for various applications.

IV. MECHANICAL PROPERTIES

4.1 HARDNESS

4.1.1 EXPERIMENTAL METHODS

Vickers hardness[14] tests were performed on the densified $MoSi_2$ and SiC-$MoSi_2$ composites to measure their room temperature hardness. The tests were based upon the ASTM standard E92-82[15]. The diamond pyramid hardness is determined by forcing a square-based pyramidal diamond indenter with an apex angle of 136° into the specimen under load and measuring the diagonals of the resulting indentions as shown in Figure 4-1. The diamond pyramid hardness is defined as the load per unit area of surface contact in kilograms per square millimeter, as calculated from the average diagonal, as follows :

$$D.P.H. = \frac{2P\sin(\alpha/2)}{d^2} \qquad (12)$$

where D.P.H. is the diamond pyramid hardness ($kg.mm^{-2}$), d is the mean diagonal of

[14]Vickers Hardness Indenter, Zwick 3212, East Windsor, CT, USA.
[15]ASTM Standard E92-82, American Society for Testing and Materials, PA, USA.

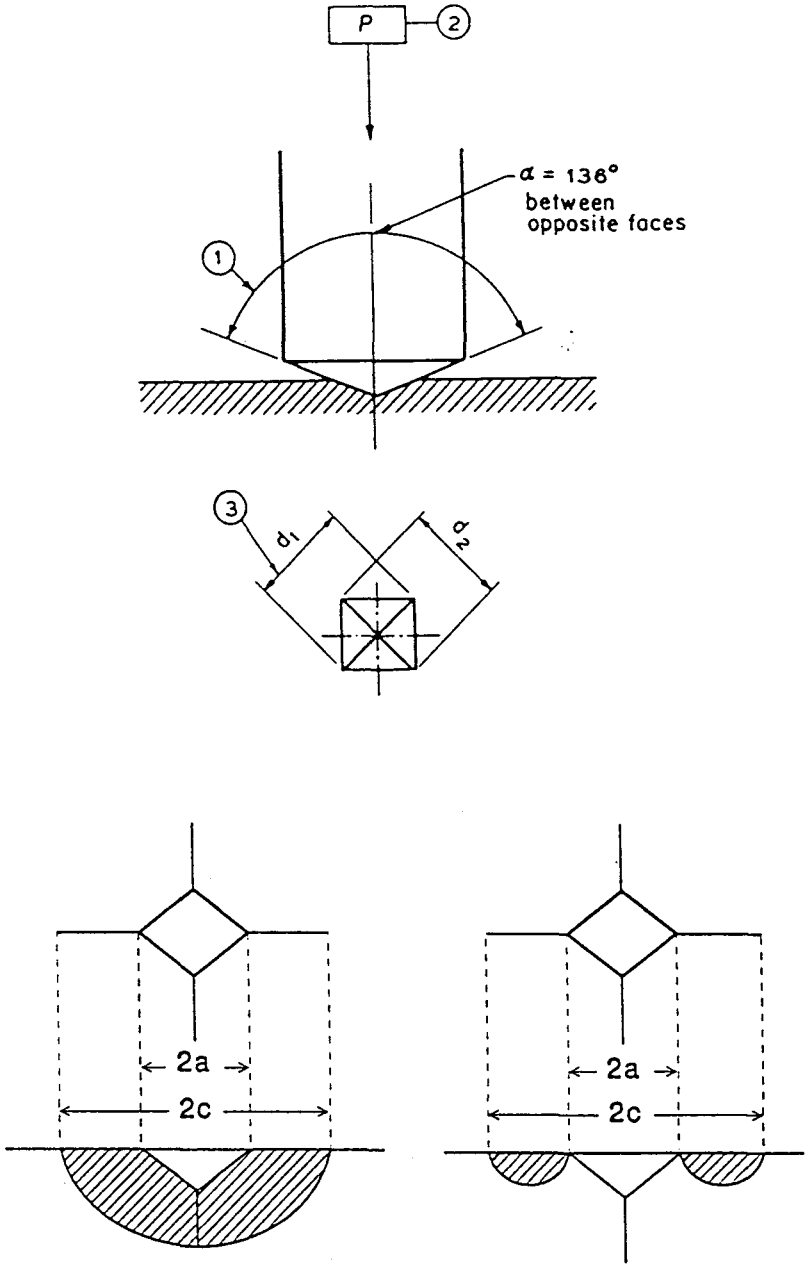

Figure 4-1: Vickers Hardness Test (ASTM E92-82).

impression (mm), $\dot{\alpha}$ is the face angle of diamond (136°), and P is the load (kg).

Besides the D.P.H. number, Vickers hardness (H_V) can also be calculated from the diagonal of the indentation. This number is calculated by the following relation (McColm 1990),

$$H_V = \frac{P}{2a^2} \qquad (13)$$

where H_V is the Vickers hardness number (GPa), P is the load (N), and 'a' is the mean diagonal of impression (m). Both expressions are used in the literature, so subsequently, both values will be calculated in this study for purposes of comparison.

The standard does not require any specification on the dimensions of the test specimens. However, the thickness must be sufficient to aviod bulging or marking on the opposite end of the specimens due to the load. Thus, rectangular test bars were cut from the polished, hot-pressed pellets with a diamond saw. The bars had the dimensions of 20 mm (length) x 3 mm (width) x 3 mm (thickness).

Five indentations with a 28.4 N (2.9-kgf) load were made uniformly along the length of the polished specimens on the surfaces parallel to the hot-pressed direction. An initial indentation study indicated there was no difference between indentation fractures placed parallel and perpendicular to the hot-pressed direction. A 30 s load cycle was used and individual indentations were separated 2-5 mm apart to prevent neighboring indent-crack interaction. Immediately after the indentation, the diagonals of the indentation were measured

with an optical microscope at 10x magnification equipped with a scaled eye-piece and polarizing filters.

4.1.2 RESULTS AND DISCUSSION

Figure 4-2 shows the SEM micrographs of the typical Vickers indentations. Table 4-1a shows the results in term of both Vickers hardness (GPa) and diamond pyramid hardness number (kg/mm^2). The results are also plotted in Figure 4-3. The hardness of the materials increased from 10.1 ± 0.1 GPa (959 ± 13 kg/mm^2) to 11.7 ± 0.6 GPa (1102 ± 52 kg/mm^2) to 12.7 ± 0.4 GPa (1199 ± 36 kg/mm^2) with the 10 vol% and 20 vol% SiC reinforcement, respectively. These represent a 16% and 26% improvement.

The results are compared with literature values in Table 4-1b. For the monolithic materials, the hardness is slightly higher than those obtained in the literature (all of these specimens were produced by the hot pressing method). For the composites, the hardness values are in close agreement, i.e. within 5% of the data of Jayashankar *et al.* (1994) and Bhattacharye *et al.* (1991). However, the hardness of the whisker-reinforced composites (Chen *et al.* 1995) was greater, which is expected because of the more effective load transfer between the matrix and whiskers which will be explained below. It is important to note that in the current study only a 2.9-kgf load was used, while in the literature, various loads were used and the results averaged out. Regardless, the results obtained here agree well with that

Figure 4-2: SEM micrographs of typical Vickers indentations.

Materials	Number of Indentations	Mean Vickers Hardness (GPa)	(kg/mm^2)	Standard Deviation (GPa)	(kg/mm^2)
$MoSi_2$	5	10.1	(959)	0.1	(13)
10 vol%SiC-$MoSi_2$	5	11.7	(1102)	0.6	(52)
20 vol%SiC-$MoSi_2$	5	12.7	(1199)	0.4	(36)

a)

Materials	This Study (GPa)	Chen *et al.* (1995) (GPa)	Bhattacharye *et al.* (1991) (GPa)	Wade *et al.* (1992) (GPa)	Wade *et al.* (1992) (GPa)	Jayashankar *et al.* (1994) (GPa)
$MoSi_2$	10.1	9.9	9.3	8.7	8.92-9.87	8.56
20vol% SiC-$MoSi_2$	12.7 (p)	13.5-14.7(w)	12.5-16 (p)			12.5 (p)

b)

(p) --- particulate reinforcement
(w) --- whisker reinforcement

Table 4-1:a) Vickers hardness test results for $MoSi_2$, 10 vol% and 20 vol% SiC-$MoSi_2$ and b) Comparison of Vickers hardness results to those obtained in the literature.

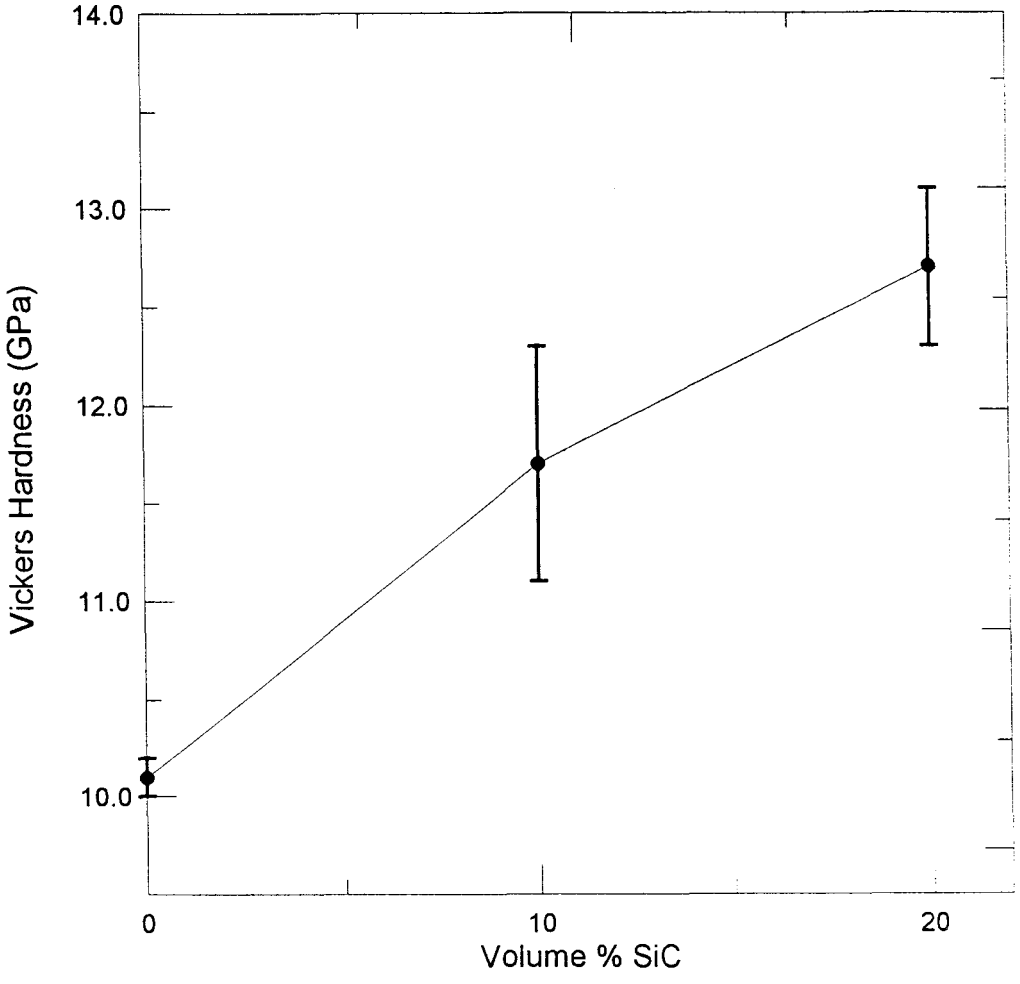

Figure 4-3: Vicker hardness test results for $MoSi_2$, 10 vol% and 20 vol% SiC-$MoSi_2$.

of previous workers.

The increase in hardness is probably due to the hardness of SiC-reinforcement and the effective load transfer from the matrix to the reinforcement, due to the strong interface, with no interfacial reaction at high processing temperature (Yang and Jeng 1991; Vasudévan and Petrovic 1992). Because of its higher elastic modulus, SiC is able to increase the hardness of the composites. The elastic modulus of SiC is 450 GPa (Ashby and Jones 1980) compared to 440 GPa for $MoSi_2$ (Nakamura 1994).

4.2 FLEXURAL STRENGTH

4.2.1 EXPERIMENTAL METHODS

For ambient temperatures, the flexural strength testing standard is based upon MIL-STD 1942(A) (1983) and ASTM C1161-90. In this study, a four-point-¼-point flexure test rig was used to measure the room temperature fracture strength of the specimens in bending. The specimen was symmetrically loaded at two locations that are situated one quarter of the overall span away from the outer two support bearings as shown in Figure 4-4. In order to relieve frictional constraints at the loading pins, it is recommended by the standard that the bearing cylinders be allowed to rotate, which was made possible by using a fully articulating four-point fixture, in which the load bearing cylinders were held in place only by low stiffness

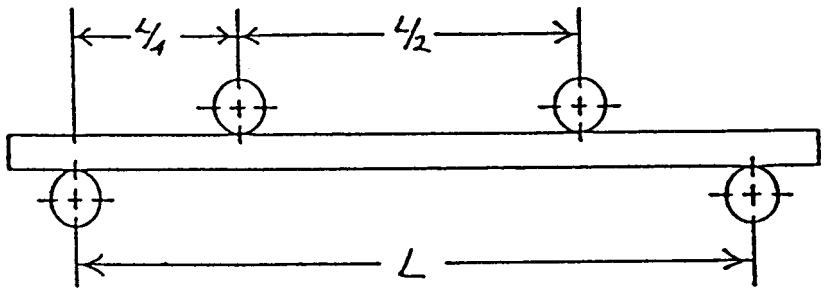

Specimen Size

Configuration	Width (b), mm	Depth (d), mm	Length (L), mm
A	2.0	1.5	25
B	4.0	3.0	45
C	8.0	6.0	90

Figure 4-4: The four-point-¼ point fixture configuration (ASTM C1161-90).

rubber bands pictured in Figure 4-5 (Bloyce 1993).

To minimize the fracture-initiating defects such as machining flaws, the samples were prepared professionally[16] to adhere to the standards as shown in Figure 4-6. These included the surface finish, the size, the tolerance of the specimen chamfers and the parallelism. However, the test specimens did not conform to the exact configuration recommended in the standard which is shown as configuration A in Figure 4-4. All specimens were 25 mm long, 3 mm wide and 2 mm thick. The relation between the strain rate and the crosshead rate (ASTM C1161-90) is,

$$\dot{e} = \frac{6ds}{L^2} \qquad \textbf{(14)}$$

where $\dot{e}$ = strain rate (s^{-1}), d = specimen thickness (mm), s = crosshead speed ($mm.s^{-1}$), and L = outer span (20 mm). The ASTM standard recommended the strain rate of $1.0x10^{-4}\ s^{-1}$; therefore, the crosshead speed employed was 0.0033 mm/s.

The strength in four-point-¼ point flexure is computed based on simple beam theory with assumptions that the material is isotropic and homogeneous and the material is linearly elastic. The formulation is,

---

[16]Bomas Machine Specialties Inc., MA, USA.

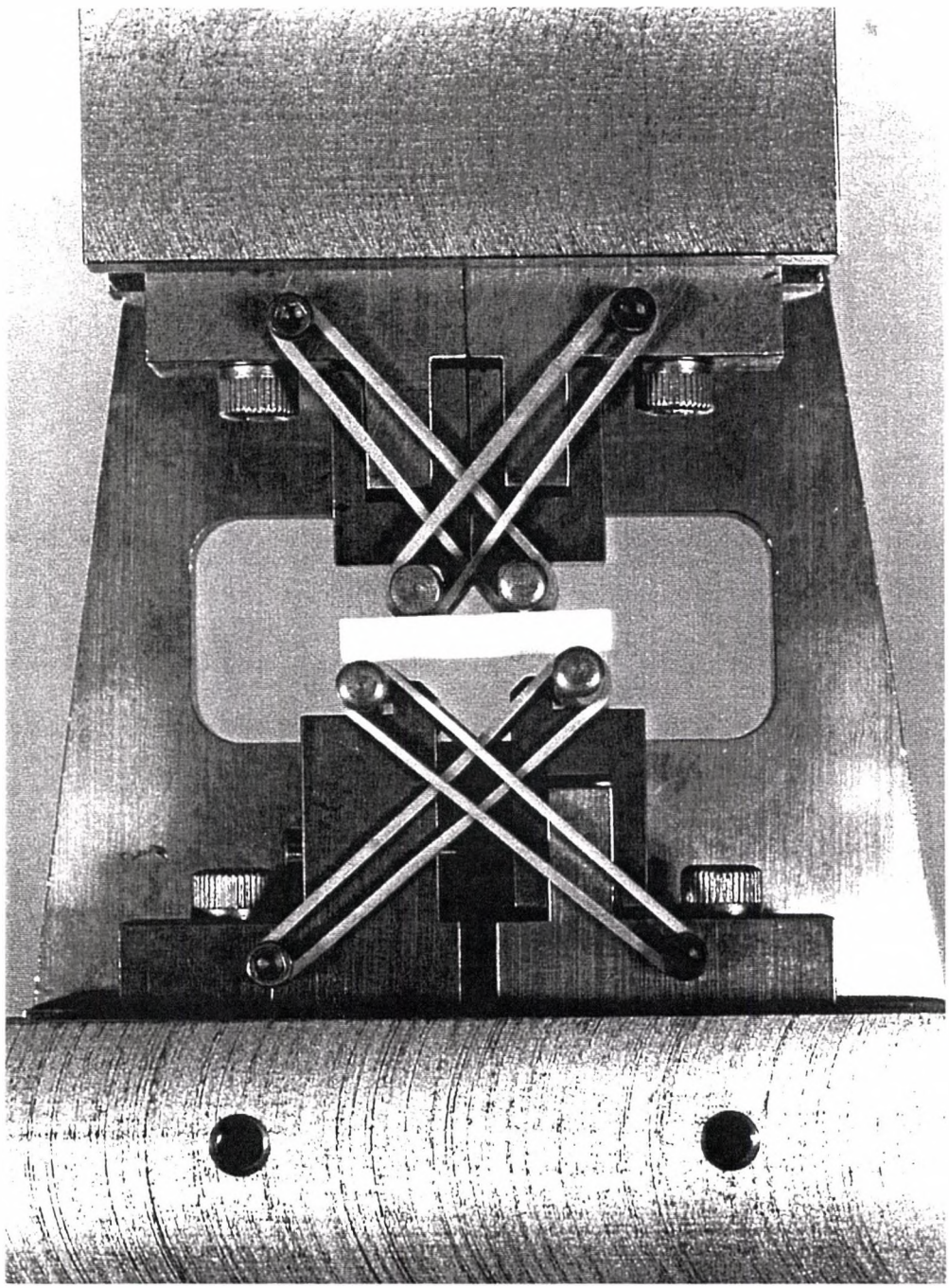

Figure 4-5: Fully articulated four point-¼ point fixture test rig (Bloyce 1993).

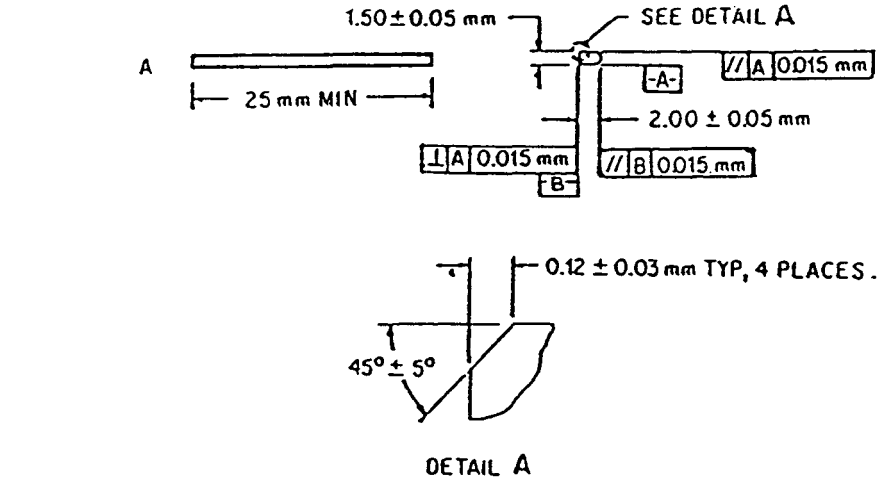

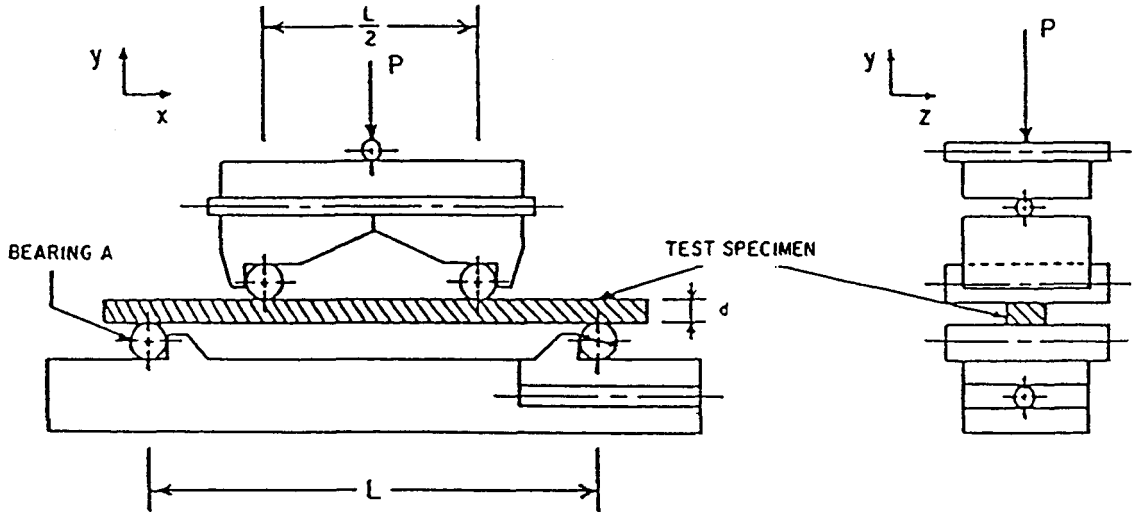

Figure 4-6: ASTM C1161-90 standard specimen dimensions and rig set-up for a four-point bend test (Bloyce 1990).

$$S = \frac{3PL}{4bd^2} \qquad (15)$$

where P is the breakload (N), L is the outer span (mm), b is the specimen width (mm), and d is the specimen thickness (mm).

The specimens were tested with the tensile surface perpendicular to the hot-press direction. After carefully placing each specimen into the test fixture to ensure alignment of the specimen in the fixture, a compressive load was applied to the fixture through a ball bearing by means of a testing machine[17].

4.2.2 RESULTS AND DISCUSSION

The results of the four-point bend test are shown in Table 4-2a and are plotted in Figure 4-7. With the reinforcement, the strength was increased from 195±39 MPa to 237±39 MPa with 10 vol% and to 299 ± 43 MPa with a 20 vol% SiC reinforcement. The fracture strength has improved by 22% and 53% respectively.

Table 4-2b shows some of the four-point bend test results obtained from the references. The fracture strength of $MoSi_2$ obtained in this study was higher than those

---

[17]Lloyds 6000R, Omnitronix Ltd., Mississauga, Ontario.

Materials	Number of Specimens	Mean Flexural Stress (MPa)	Standard Deviation (MPa)
$MoSi_2$	31	195	39
10 vol%SiC-$MoSi_2$	26	237	39
20 vol%SiC-$MoSi_2$	32	299	43

a)

Materials	This Study (MPa)	Tuffe *et al.* (1993) (MPa)	Gibbs *et al.* (1987) (MPa)	Yang *et al.* (1990) (MPa)	Gac *et al.* (1985) (MPa)	Jayashankar *et al.* (1994) (MPa)
$MoSi_2$	195	140	173	224	140-160	185
20vol% SiC-$MoSi_2$	299 (p)		331(w)	263 (w)	310 (w)	

b)

(p) --- particulate reinforcement
(w) --- whisker reinforcement

Table 4-2: a) Four-point bend test results for $MoSi_2$, 10 vol% and 20 vol% SiC-$MoSi_2$ and b) Comparison of four-point bend test results to those obtained in the literature.

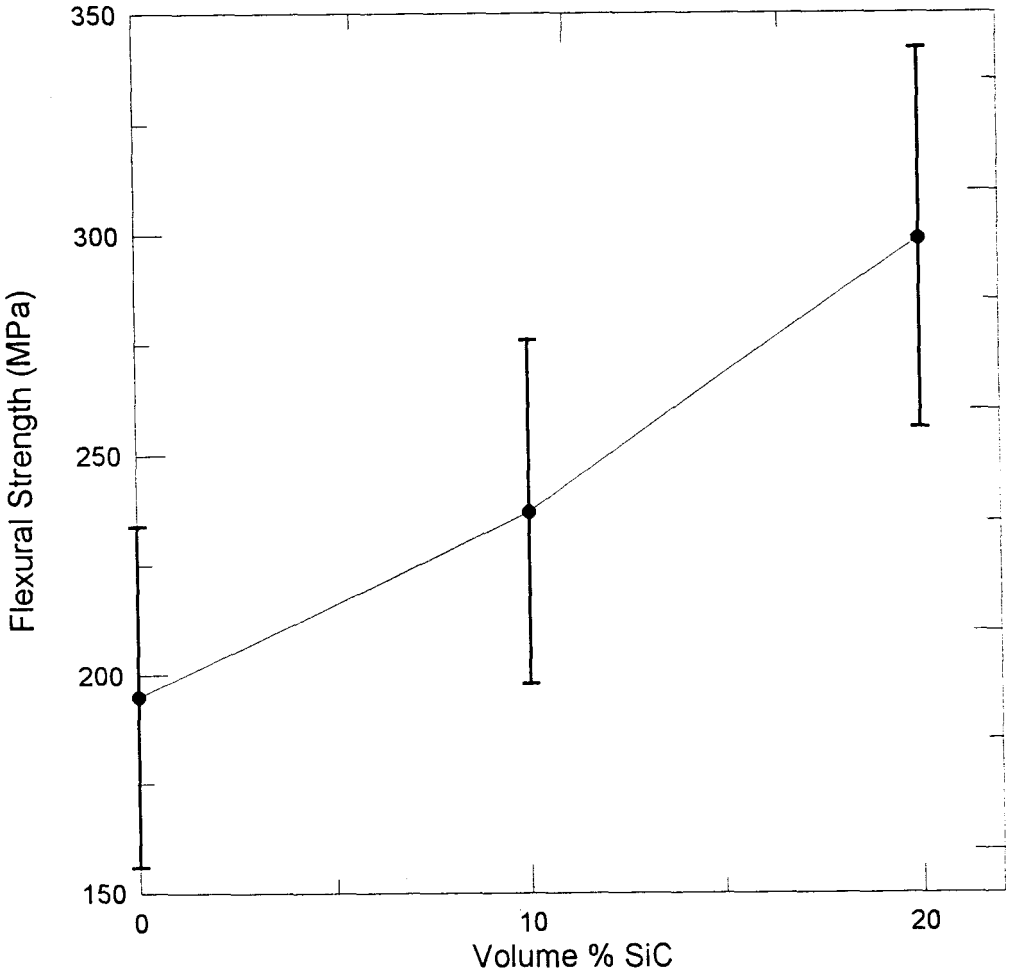

Figure 4-7: Four-point bend test results for $MoSi_2$, 10 vol% and 20 vol% SiC-$MoSi_2$.

reported in the literature, except by Yang *et al.* (1990). As for the composites, the strength was reasonably close to those reported by other workers, which is very encouraging, considering that the results from the composites were compared to whisker-reinforced composites. Furthermore, the measured composites fracture strength of 299 MPa approaches the acceptable use regime for structural applications (Gac and Petrovic 1985). The results obtained are believed to be accurate and reliable because ASTM standards were followed closely, in contrast to some experiments from the literature.

The flexural strength of the brittle materials is dependent on both its inherent resistance to fracture and the presence of defects. Therefore, analyses of the fracture surface and fractography were done on the specimens to determine the flaws that were responsible for fracture. SEM micrographs of the typical fracture surfaces of the $MoSi_2$ and SiC-$MoSi_2$ composites are shown in Figure 4-8. The flaw size can be estimated from the fracture strength and the fracture toughness obtained in this study, using the following equations (Broek 1982; Knott 1973):

1) edge defects:

$$K_{IC}=\sigma_f\sqrt{\pi a}\left(\sec\frac{\pi a}{W}\right)^{1/2} \qquad \textbf{(16)}$$

2) internal defects:

$$K_{IC}=Y\sigma_f\sqrt{\pi a} \qquad \textbf{(17)}$$

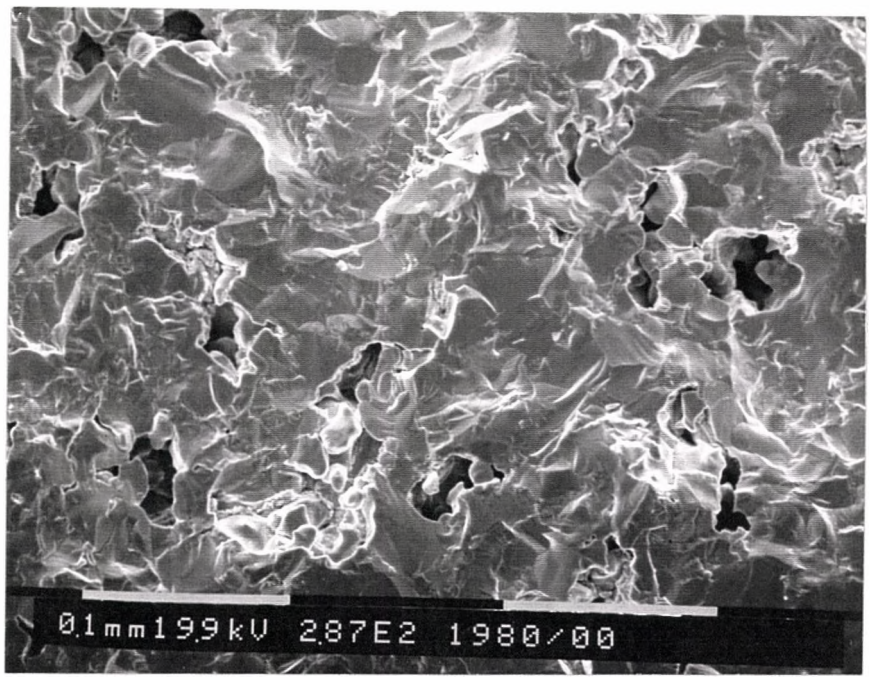

a)

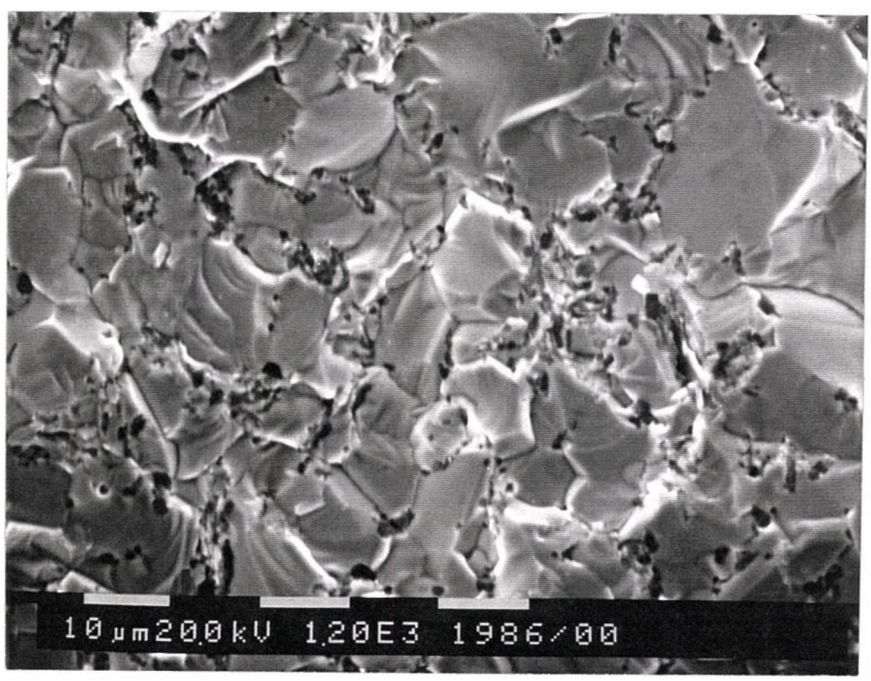

b)

Figure 4-8: SEM micrograph of typical fracture surface of a) $MoSi_2$ and b) SiC-$MoSi_2$ composites.

$$Y = 1.99 - 0.41\frac{a}{W} + 18.7\left(\frac{a}{W}\right)^2 - 38.48\left(\frac{a}{W}\right)^3 + 53.85\left(\frac{a}{W}\right)^4 \quad \textbf{(18)}$$

where K_{IC} is the fracture toughness (MPa.$m^{1/2}$), σ_f is the fracture stress (MPa), a is the defect size (m), and W is the width (m). The estimated flaw sizes were 50-60 μm as shown in Table 4-3. The flaw size of this order of magnitude were then located on the fracture surface using the SEM.

Figure 4-9 shows the machining flaws which were detected in only a few samples. On the fracture surface of $MoSi_2$, residual pores left from the incomplete densification process were common as shown in Figure 4-10. This was confirmed when monolithic materials were found to have lower densities compared to the composites after hot pressing as shown in Table 3-3. The reason was likely due to the inaccuracy and inconsistency of the applied load during the hot-pressing. These pores were the major strength limiting flaws in the monolithic materials.

Pore defects were not significant in the composites, but inhomogeneous grain size distribution was apparent in both the monolithic materials and the composite materials as shown in Figure 4-11. The unusually large grains in these materials may be responsible for initiating the fracture. $MoSi_2$ has a tetragonal crystal structure with a high c/a ratio of 2.45. Upon cooling from the densification process, it was subjected to a high anisotropic residual stress within the individual grains. Experimentally, the residual stress in hot-pressed polycrystalline $MoSi_2$ with an 80 μm grain size can be as high as 84 MPa (Berkowitz-Mattuck *et al.* 1970). This large stress will likely cause the materials to fail at a lower fracture stress.

Materials (Defect)	Fracture Strength (MPa)	Fracture Toughness ($MPa.m^{1/2}$)	Width (mm)	Flaw Size (microns)
$MoSi_2$ (edge)	195	2.79	3	65
$MoSi_2$ (internal)	195	2.79	3	62
10 vol% SiC-$MoSi_2$ (edge)	237	3.31	3	62
10 vol%SiC-$MoSi_2$ (internal)	237	3.31	3	50
20 vol%SiC-$MoSi_2$ (edge)	299	4.11	3	60
20 vol%SiC-$MoSi_2$ (internal)	299	4.11	3	48

Table 4-3: Estimation of the flaw sizes.

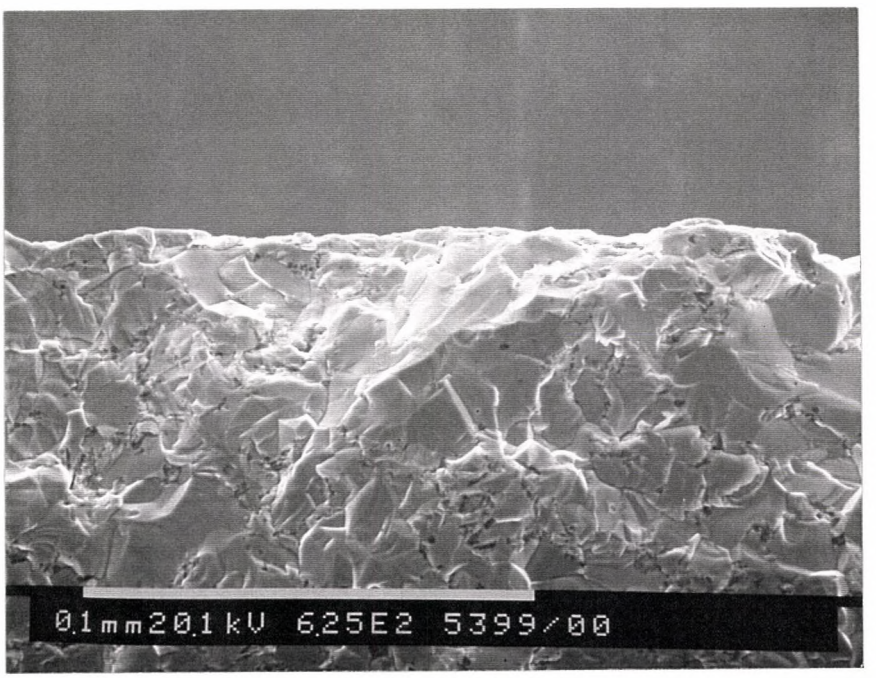

a)

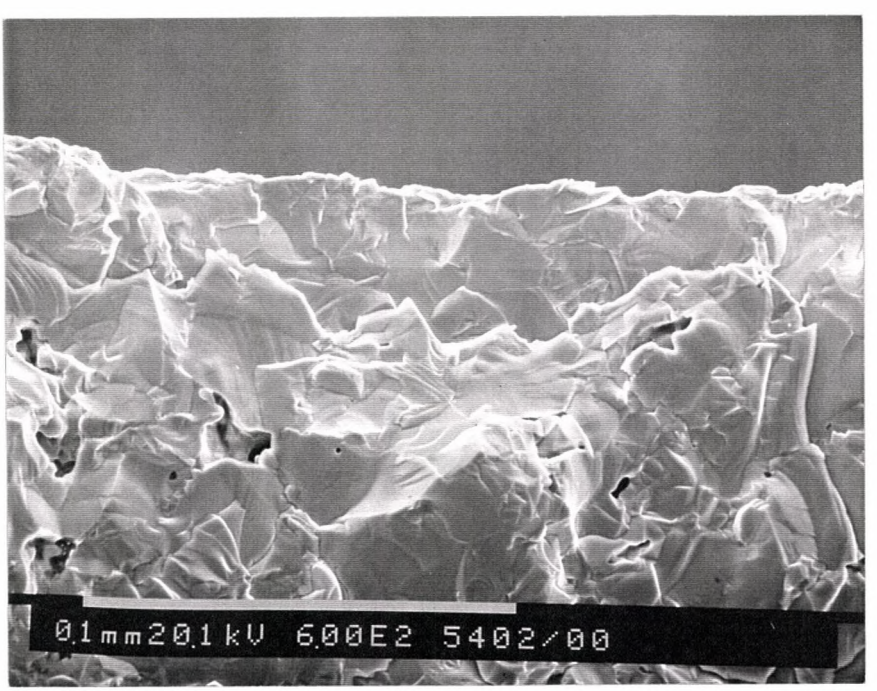

b)

Figure 4-9: SEM micrograph showing the fracture-initiating machining defect in a) $MoSi_2$ and b) SiC-$MoSi_2$ composite.

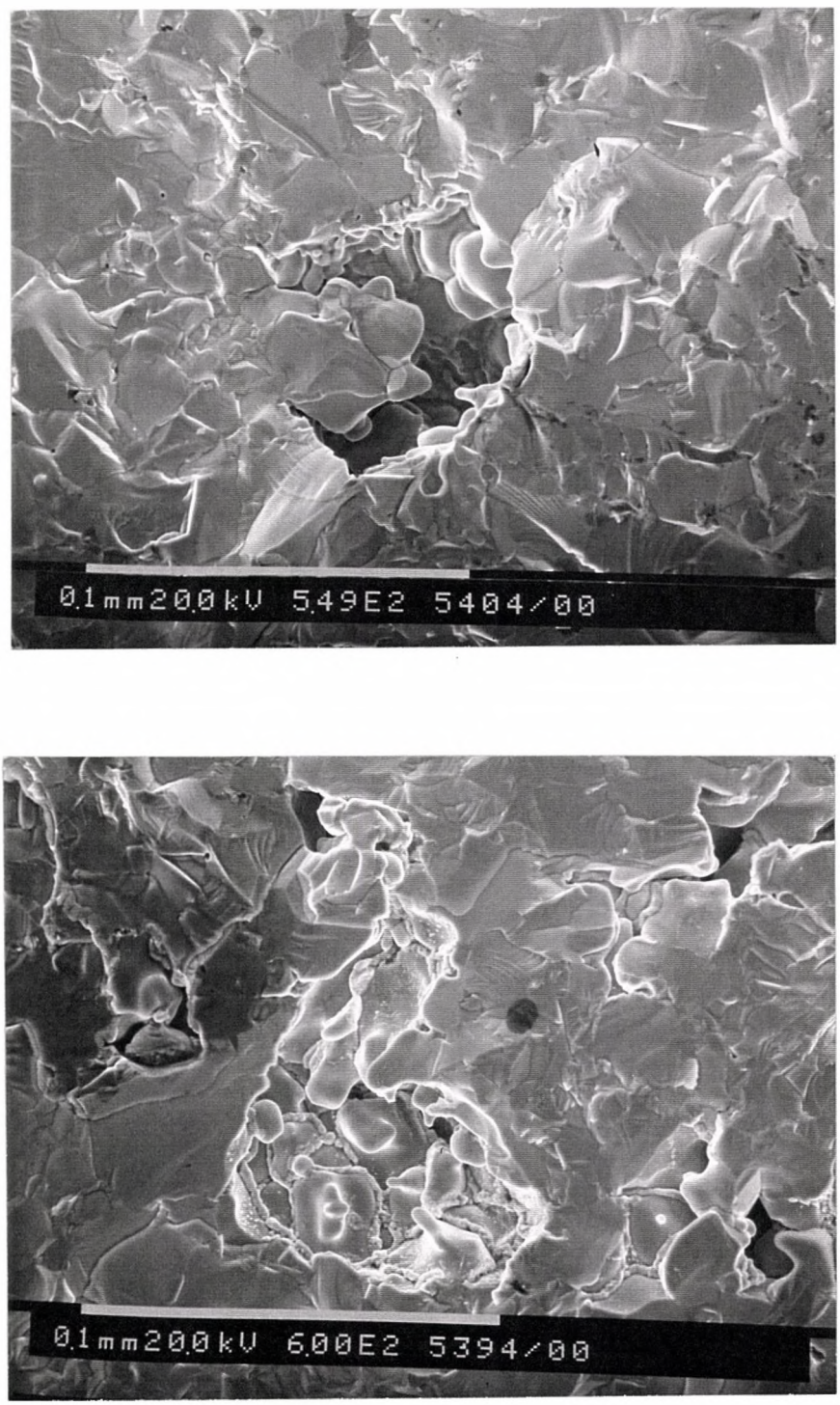

Figure 4-10: SEM micrograph showing the fracture-initiating pores defect in $MoSi_2$.

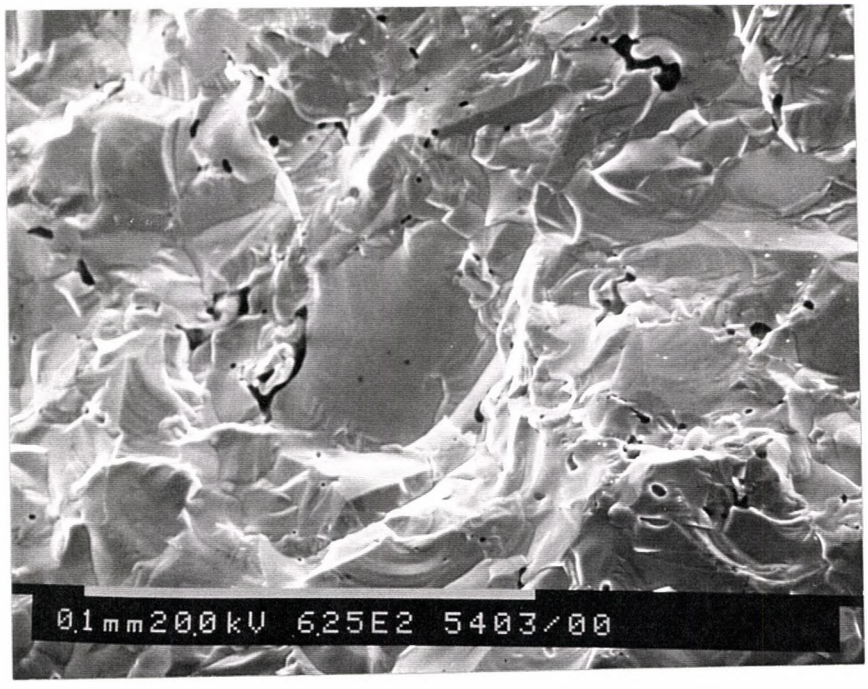

a)

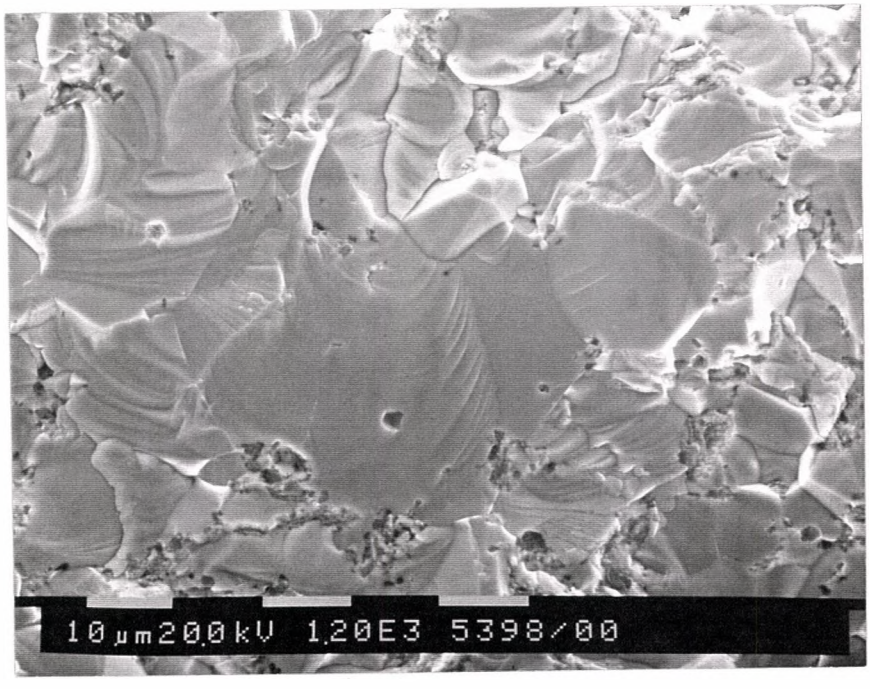

b)

Figure 4-11: SEM micrograph showing the unusual large grains in a) $MoSi_2$ and b) SiC-$MoSi_2$ composites.

This defect can originate from the agglomerate of the precursor powder and the grain growth during the combustion synthesis process mentioned earlier in Section 3.6.

The improved fracture strength of the composite is due to the effective load transfer to the reinforcement by the matrix, since there is a strong interface between them. Moreover, the SiC-reinforcement has a slightly higher elastic modulus than the $MoSi_2$-matrix. Unlike combustion synthesis, the conventional methods include hot pressing at high temperature for several hours. This treatment causes an interfacial reaction between the SiC-reinforcement and the impurities in the matrix which leads to a weak interface. Furthermore, these reinforcements tend to oxidize to form a layer of silica which degrades the room temperature mechanical properties. SiC-fibres and platelets are especially susceptible to this condition (Yang and Jeng 1991; Petrovic 1985), since both have large contact areas with the matrix.

The strength improvement in the composites can also be attributed to the absence of pore defects and the reduced amount of SiO_2. Thin layers of SiO_2 formed around each particle, which may isolate the $MoSi_2$ grains, resulting in a weak interface (Subrahmanyam 1994); thereby resulting in the ineffective rule-of-mixture strengthening. By in-situ formation of SiC, C will act as a deoxidant and react with Si to form SiC, minimizing the formation of SiO_2 at the grain boundary (Maloy *et al.* 1991). As well, with the formation of SiC, the grain growth in $MoSi_2$ is reduced, hence reducing the residual stress in the composites.

On the fracture surface, transgranular fracture was observed to be the dominant fracture mode for $MoSi_2$ grains. This mode was also observed by other researchers (Wade and Petrovic 1992a; Yang and Jeng 1991) on specimens produced by the hot-pressing

method. With a higher hot-pressing temperature, the density can be increased, but at the expense of increasing SiO_2 formation at the interface, which explains the dominance of intergranular fracture. Therefore, the fracture modes can be used to indicate if there is a high silica content in the materials. Since transgranular is the dominant fracture mode, less silica is formed in the combustion synthesized materials. Transgranular fracture occurs when the crystal cleavage planes are weaker than the grain boundaries. The weak cleavage planes of $MoSi_2$ due to the internal stresses on the anisotropic tetragonal unit cell results from the densification processing and low energy preferential cleavage plane. This plane runs parallel with the low energy plane, which is the result of double cross-packed silicon layers alternating with molybdenum layers.

The ASTM standard also recommended that the estimate of the strength distribution with at least 30 specimens be reported in the form of Weibull modulus plot. The number of specimens required by this test method has been established to ensure reasonable confidence limits on strength distribution parameters and to help discern multiple-flaw population distributions (ASTM C1161-90). The Weibull distribution function characterizes a set of strength data with respect to its variability (represented by the Weibull modulus, m) and its characteristic strength, σ_o.

The linearized form of the Weibull equation is :

$$\ln\ln\frac{1}{1-p} = m\ln\sigma - m\ln\sigma_o \qquad (19)$$

where P is the cumulative failure probability for a fracture stress σ_f.

In this case, P was estimated using,

$$P_i = \frac{i-0.5}{n} \qquad (20)$$

where i represents the rank number (i=1, for the weakest specimen) and n is the total number of specimens tested. This estimator results in the smallest bias on the derived value of the Weibull distribution (Steen *et al.* 1992).

The Weibull modulus, m, and characteristic strength, σ_o, were calculated from the plot in Figure 4-12 and tabulated in Table 4-4. The arithmetic mean strength value (σ at P=0.5), σ_{avg}, is usually reported in the literature, and hence, it was calculated here using the following equation (Kingery 1976a),

$$\sigma_{avg} = \sigma_o (1/2)^{1/m} \qquad (21)$$

Table 4-4 also includes the ratio of the average strength to the characteristic strength to indicate the spread of observed strength values of the materials (Kingery 1976).

The Weibull plots of the materials modelled the data well since the R^2-values were > 90% for all 3 plots and the data all show the low strength "tails". For a reliable material, ideally the Weibull modulus should be as high as possible. A typical value of the conventional

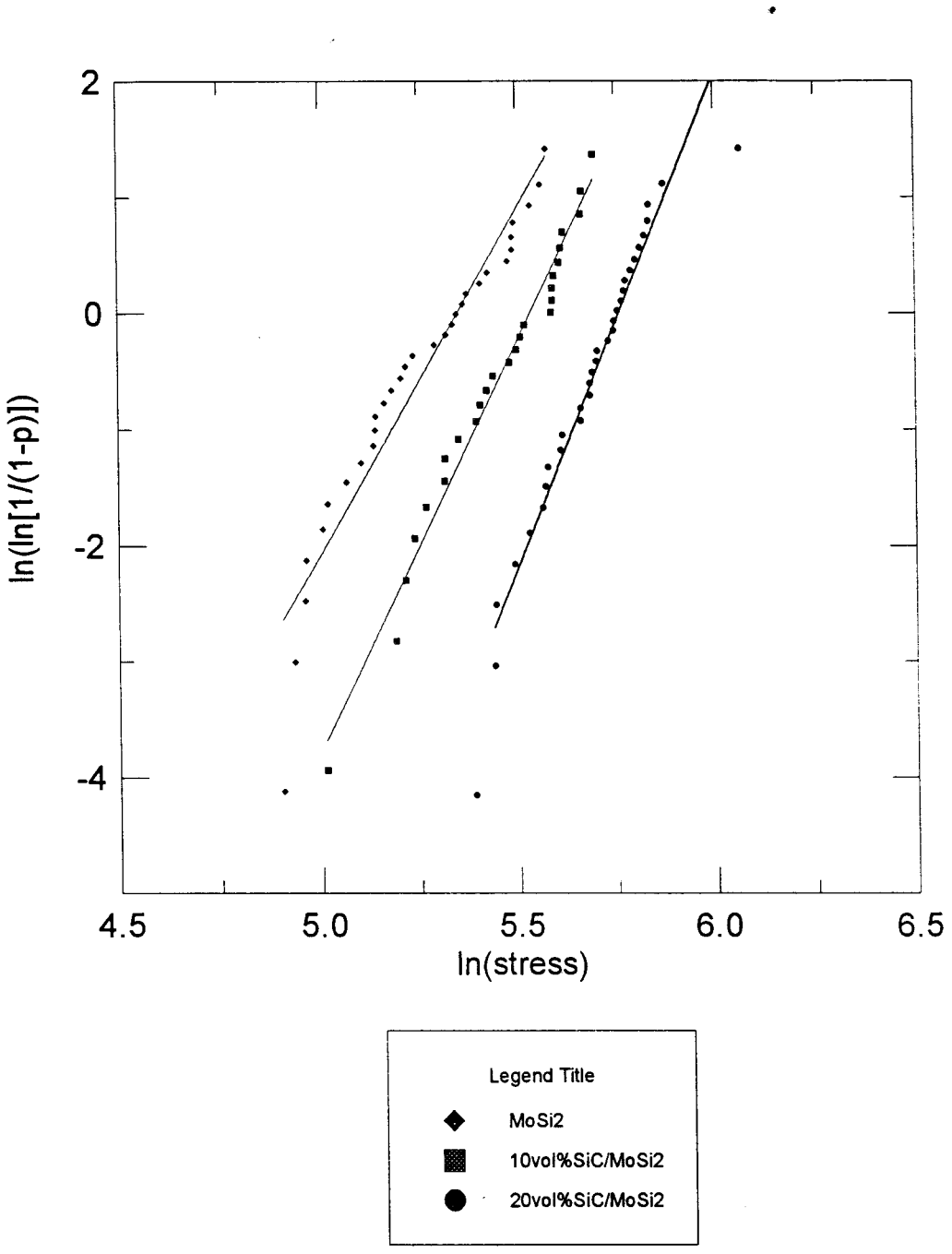

Figure 4-12: Weibull modulus plots for $MoSi_2$, 10 vol% and 20 vol% SiC-$MoSi_2$.

Materials	Number of Specimens	σ_o (MPa)	σ_m (MPa)	σ_o / σ_m	Weibull Modulus
$MoSi_2$	31	210	187	1.12	5.95 ± 1.20
10 vol%SiC-$MoSi_2$	26	253	229	1.10	7.05 ± 1.25
20 vol%SiC-$MoSi_2$	32	316	291	1.09	8.45 ± 1.22

Table 4-4: Results obtained from the Weibull's plot.

as-finished ceramics such as soda-lime and a vitreous-bonded polycrystalline alumina is approximately 10. The low Weibull modulus obtained in this case was most likely due to the flaws mentioned above. However, there was an increase of the modulus with an increase in the amount of reinforcement, which is encouraging. With a better control of the agglomerates in the original precursor powders, a more uniform, fine grained material can be produced which allows a stronger and more reliable product.

4.3 FRACTURE TOUGHNESS

4.3.1 EXPERIMENTAL METHODS (I)

Fracture toughness relates the fracture stresses of a material with the critical flaw size and associated geometry (Whitehead 1994). In the present study, the fracture toughness was acquired by the chevron-notched-bend-bar technique, although many different chevron-notch tests exist (Newman 1984). The loading arrangement and the geometry of the four-point-bend chevron-notched bar are shown in Figure 4-13 (Munz *et al.* 1981).

Using the energy balance analysis for crack propagation, Munz *et al.* (1981) obtained a relationship between the maximum load, P_{max}, and K_{IC} for the chevron-notched bend bar in the stable crack growth regime. The relationship involved a compliance function, Y^*, such that Y^* is minimized to Y^*_m when the load is maximized and,

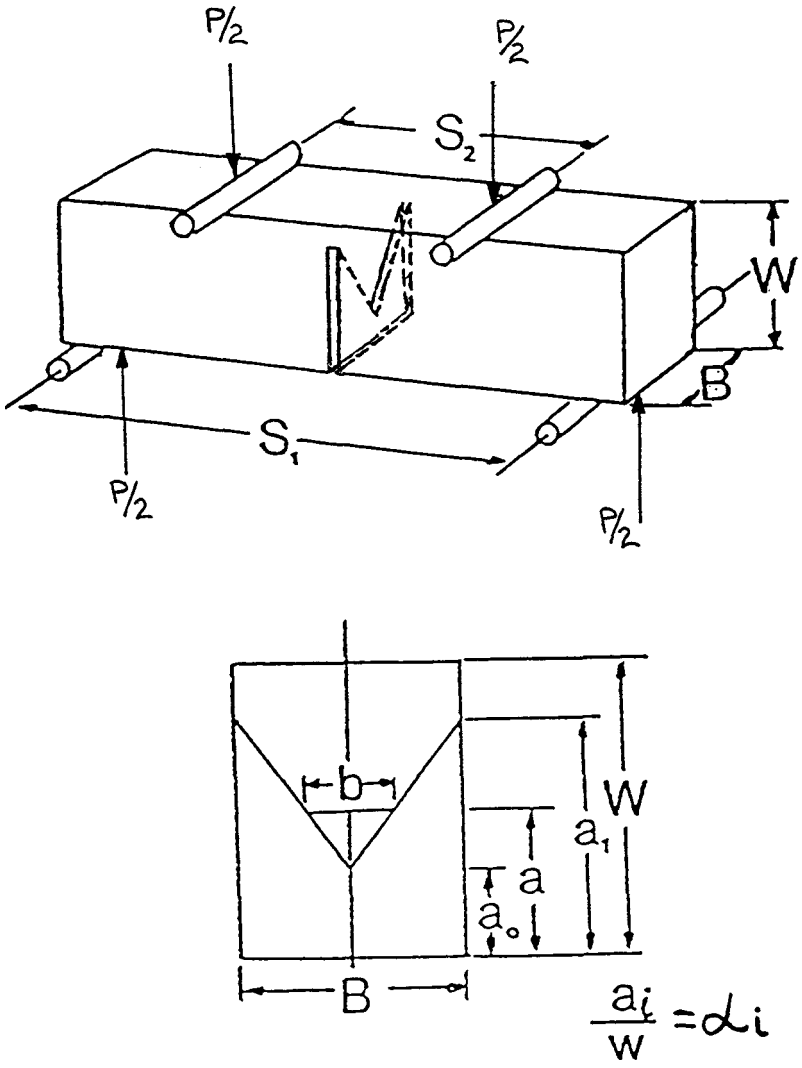

Figure 4-13: The loading arrangement and the geometry of the four-point-bend chevron-notched bar (Munz *et al.* 1981).

$$K_{IC} = \frac{P_{max}}{B\sqrt{W}} Y_m^* \qquad (22)$$

where P_{max} is the breaking load, B is the sample width and W is the sample height. Y^* was derived using a straight-through-crack assumption by Munz *et al.* (1981) or the slice model of Bluhm (1975). Y^*_m is obtained by curve-fitting, i.e.,

$$Y_m^* = (3.08 + 5.00\alpha_o + 8.33\alpha_o^2)\left(\frac{S_1 - S_2}{W}\right)\left(\frac{\alpha_1 - \alpha_o}{1 - \alpha_o}\right)\left[1 + 0.007\left(\frac{S_1 S_2}{W^2}\right)^{1/2}\right] \qquad (23)$$

where $\alpha_o = a_o/W$, $\alpha_1 = a_1/W$ and the other variables are as defined in Figure 4-13 (Munz *et al.* 1980). For the above equation to be valid, stable crack growth must precede final failure. That is, the region between the initial elastic region and the final failure must appear as non-linear on the load-displacement curve (Munz 1983). Munz *et al.* (1981) and Salem and Shannon (1987) have studied the influence of the notch geometry on K_{IC} and have generally agreed that the value of K_{IC} is independent of the chevron geometry (in the range $\alpha_o = 0.07$ to 0.37 and $\alpha_1 = 0.85$ to 1.0). The dimensions of the machined specimens[18] were 25 mm (length) x 2 mm (width) x 3 mm (thickness), with the notch geometry as follows: $a_o = 0.2$ mm and $a_1 = 2.0$ mm ($\alpha_o = 0.07$, $\alpha_1 = 0.67$). The surface finish of the specimens was obtained using 320 grit abrasive.

---

[18]Bomas Machine Specialties Inc., MA, USA.

The specimens were tested with the tensile surface perpendicular to the hot-press direction. Like the flexural testing mentioned earlier, each specimen was placed carefully into the test fixture to preclude possible damage and to ensure alignment of the specimen in the fixture. A compressive load was applied to the fixture through a ball bearing by means of the testing machine. Figure 4-14 shows a typical fractured chevron-notched specimen.

4.3.2 EXPERIMENTAL METHODS (II)

As a comparison, the toughness of the specimens was measured by the indentation test method proposed by Anstis *et al.* (1985). For this test, a Vickers hardness indentation was impressed on the specimens. The fracture toughness was then calculated from the crack lengths radiating from the corners of the impression by the following relationship,

$$K_{IC}=0.016\left(\frac{E}{H_V}\right)^{1/2}\frac{P}{C_o^{3/2}} \qquad (24)$$

where E is the Young's modulus (GPa), H_v is the Vickers hardness (GPa), P is the indentation load (N), and C_o is the crack length (m).

The Young's modulus, E, and Poisson's ratio, ν, for the materials were calculated

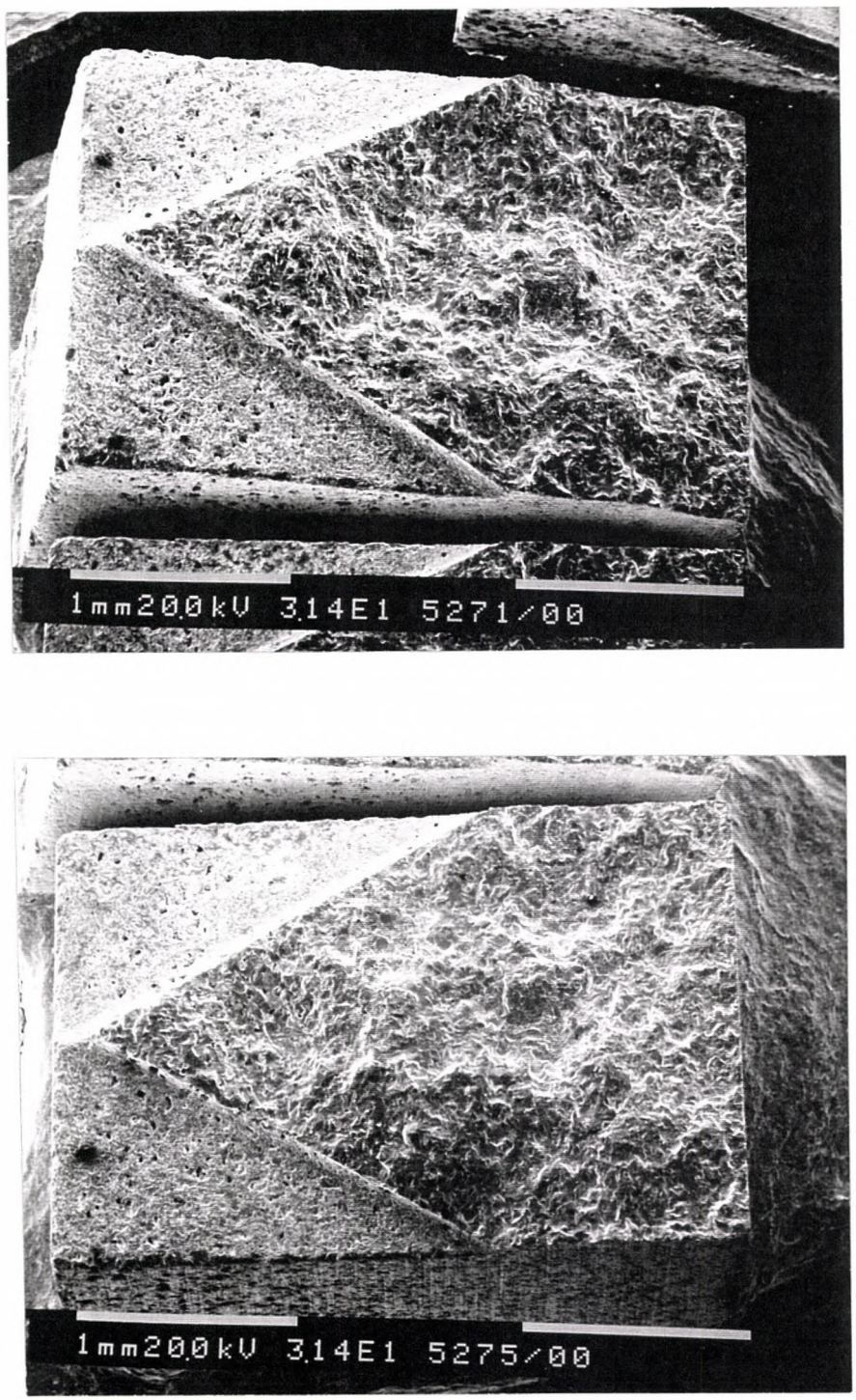

Figure 4-14: Fracture surfaces of the four-point-bend chevron-notched bar.

using ultrasonic wave velocities[19] (Schreiber *et al.* 1973). The longitudinal velocity, V_l, and the transversal wave velocity, V_t, in samples of dimension 5 mm (length) x 2 mm (width) x 3 mm (thickness) were measured along the plane parallel to the hot-pressed direction. The Young's modulus and Poisson's ratio were determined by the following relationship,

$$E=\frac{3(v_t^2 v_l^2-\frac{4}{3}v_t^4)\rho}{(v_l^2-v_t^2)} \qquad (25)$$

$$\nu=\frac{v_l^2-2v_t^2}{2(v_l^2-v_t^2)} \qquad (26)$$

where ρ is the density of the samples. Since the acoustic wave velocities are influenced by the porosity, Fisher *et al.* (1992) proposed to extrapolate the moduli to zero porosity by the following relationship,

$$E_o=\frac{E\rho}{2\rho-\rho_o} \qquad (27)$$

[19]Measurements done by Dr. N.D. Patel, McMaster University.

where E_o is the Young's modulus at zero porosity (GPa), ρ is the measured density ($g.cm^{-3}$), and ρ_o is the theoretical density ($g.cm^{-3}$). This value of Young's modulus was used to calculate the fracture toughness.

The experimental procedure was similar to that done for the hardness testing in Section 4-1, except that the load was increased to 294 N (30 kgf) to produce visible cracked lengths. Only one load was used, since the toughness has been shown to be load independent for $MoSi_2$ and SiC-$MoSi_2$ composites. That is, they do not exhibit R-curve behavior like SiC-reinforced alumina and silicon nitride (Wade and Petrovic 1992; Bhattacharya and Petrovic 1991). Immediately after the indentation, the crack length and diagonal of the indentation were measured with an optical microscope at a magnification of 10x. If more than four radial cracks were observed, which occurred often, the four longest orthogonal cracks were assumed to be the primary cracks. These were used for the calculation of H_v and fracture toughness measurements.

4.3.3 RESULTS AND DISCUSSION (I)

The fracture toughness data is summarized in Table 4-5a and plotted in Figure 4-15. There was an increase in fracture toughness from 2.79 ± 0.36 $MPa.m^{1/2}$ to 3.31± 0.41 $MPa.m^{1/2}$ with 10 vol% SiC and to 4.08± 0.30 $MPa.m^{1/2}$ with 20 vol% SiC. These represent a 20% and 46% incremental increase, respectively.

Materials	Number of Specimens	Mean Fracture Toughness ($MPa.m^{1/2}$)	Standard Deviation ($MPa.m^{1/2}$)
$MoSi_2$	6	2.79	0.36
10 vol%SiC-$MoSi_2$	6	3.31	0.41
20 vol%SiC-$MoSi_2$	6	4.08	0.30

a)

Materials	This Study ($MPa.m^{1/2}$)	Carter *et al.* (1989) ($MPa.m^{1/2}$)	Richardson *et al.* (1991) ($MPa.m^{1/2}$)	Gibbs *et al.* (1987) ($MPa.m^{1/2}$)
$MoSi_2$	2.79	5.32		4.38
20 vol%SiC-$MoSi_2$	4.08	6.59-8.2 (w)	7.5 (pl)	5.68 (w)

b)

(p) --- particulate reinforcement
(w) --- whisker reinforcement
(pl) --- platelet reinforcement

Table 4-5: a) Fracture toughness results for $MoSi_2$, 10 vol% and 20 vol% SiC-$MoSi_2$ (Chevron-notched) and b) Comparison of fracture toughness results to those obtained in the literature (Chevron-notched).

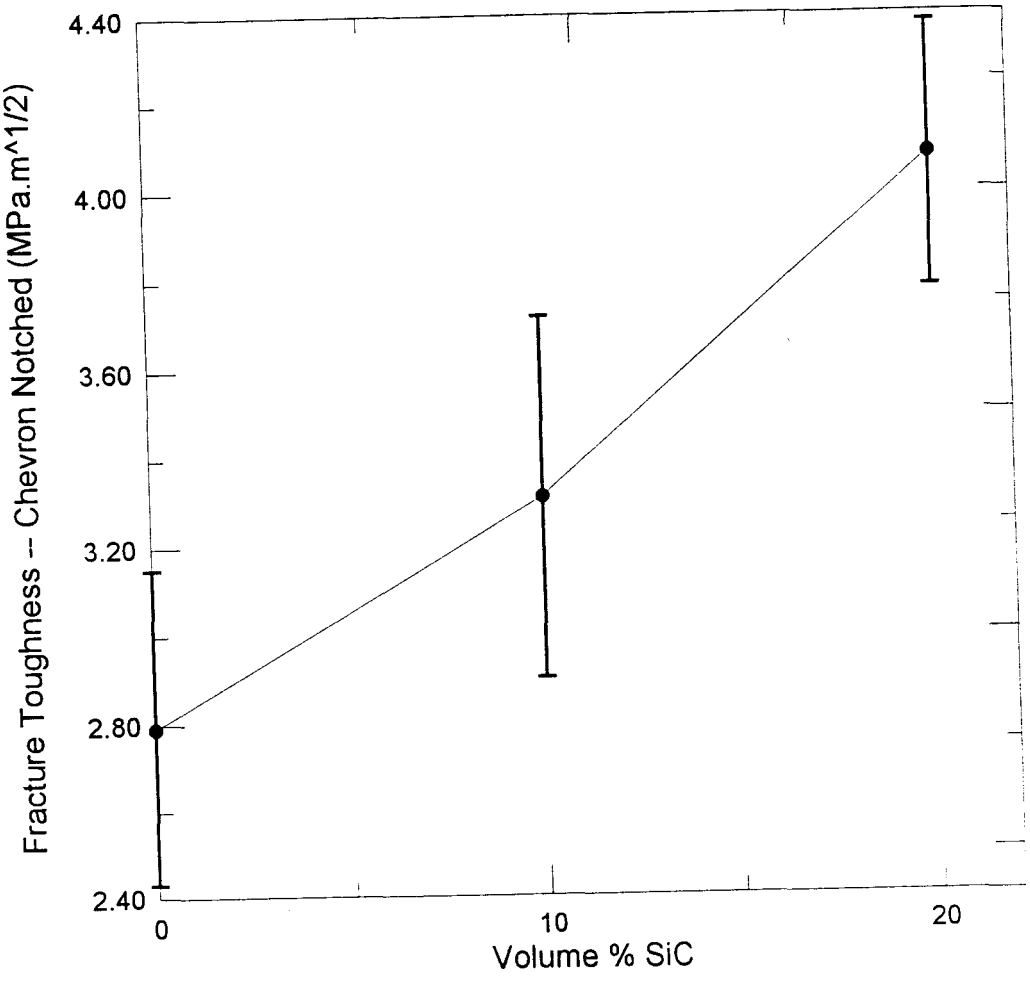

Figure 4-15: Chevron-notched fracture toughness results for $MoSi_2$, 10 vol% and 20 vol% SiC-$MoSi_2$.

These results were lower than those reported in the literature (Table 4-5b), especially for the 20 vol% reinforcement composites. Still, it was felt that the results obtained were reasonably representative. The discrepancy may be due to the testing conditions, which were not fully reported in the literature. These include the number of specimens tested, the density and the criterion of the transition from stable to unstable crack propagation. All these can increase or decrease the fracture toughness by a large margin. Another reason for the discrepancy could be the notch geometry used in this study, which did not fall into the recommended range of $\alpha_o = 0.07$ to 0.37 and $\alpha_1 = 0.85$ to 1.0. In this study, the value of α_o was 0.07 and α_1 was 0.67. The deviation was due to a geometry calculation error on the machining of the notch. However, the stress vs strain curve shows the smooth transition from the stable to unstable crack growth, thus adhering to the criterion and validating the results obtained as shown in Figure 4-16. Furthermore, six samples were tested for each compositions and they were all professionally notched. To complement these results, the fracture toughness was also measured by the indentation-crack method.

4.3.4 RESULTS AND DISCUSSION (II)

The fracture toughness data from the indentation fracture method is summarized in Table 4-6 and Figure 4-17. The results obtained were slightly higher than those from the chevron-notch method as shown in Figure 4-18. However, they did show improvement in

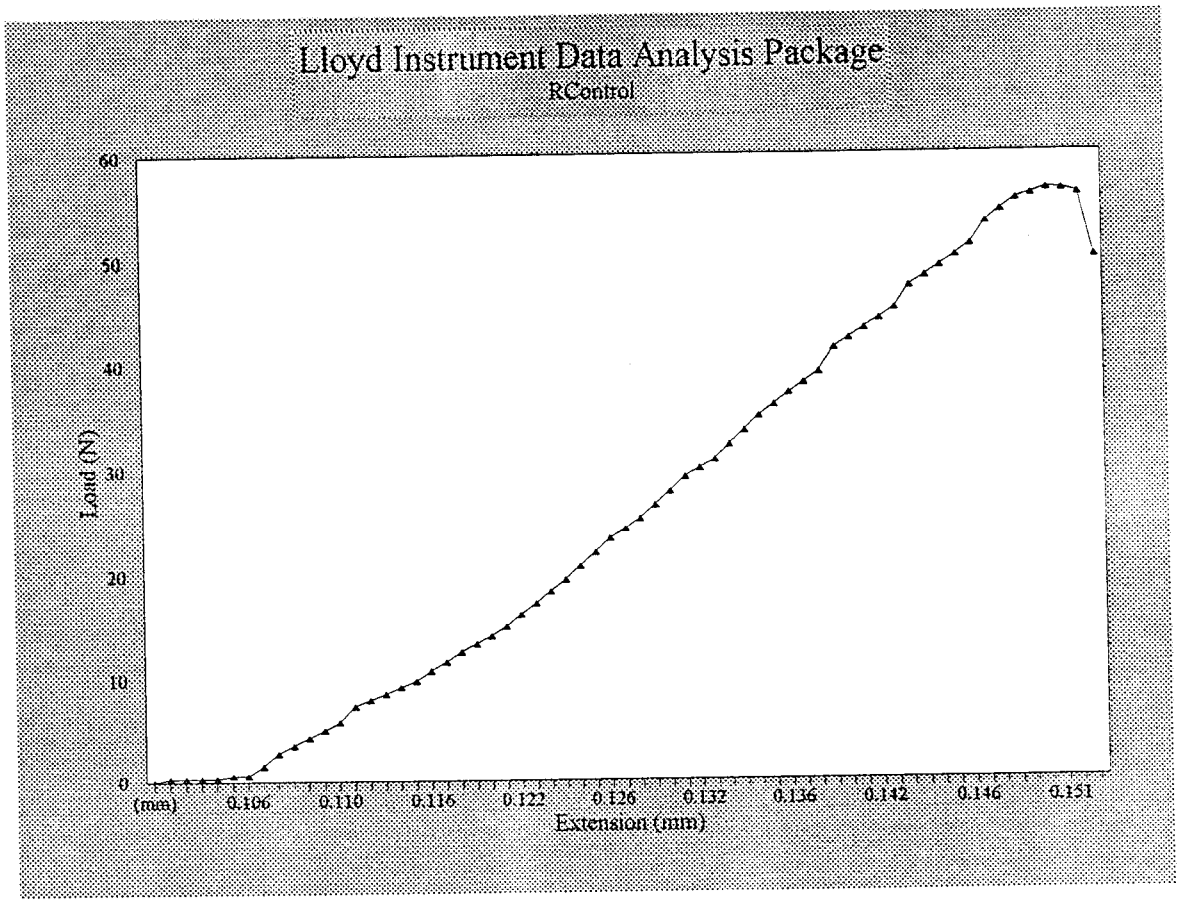

Figure 4-16: Typical load-displacement curve obtained during Chevron-notch testing.

Materials	Number of Indentations	E (GPa)	E_o (GPa)	ν	H_v (GPa)	Mean Fracture Toughness ($MPa.m^{1/2}$)
$MoSi_2$	5	396	404	0.14	10.1	2.35 ± 0.25
10 vol%SiC-$MoSi_2$	5	396	407	0.15	11.7	3.53 ± 0.46
20 vol%SiC-$MoSi_2$	5	413	422	0.14	12.7	4.98 ± 0.63

Materials	This Study ($MPa.m^{1/2}$)	Chen *et al.* (1995) ($MPa.m^{1/2}$)	Bhattacharye *et al.* (1991) ($MPa.m^{1/2}$)	Wade *et al.* (1992) ($MPa.m^{1/2}$)	Petrovic *et al.* (1990) ($MPa.m^{1/2}$)	Jayashankar *et al.* (1994) ($MPa.m^{1/2}$)
$MoSi_2$	2.35	2.4-2.7	2.85	2.3-3.6	2.5	2.5
20 vol%SiC-$MoSi_2$	4.98	3.7-4.8 (w)	4.5 (p)			3.5-4.25 (p)

(p) --- particulate reinforcement
(w) --- whisker reinforcement

Table 4-6: a) Fracture toughness results for $MoSi_2$, 10 vol% and 20 vol% SiC-$MoSi_2$ (indentation method) and b) Comparison of fracture toughness results to those obtained in the literature (indentation method).

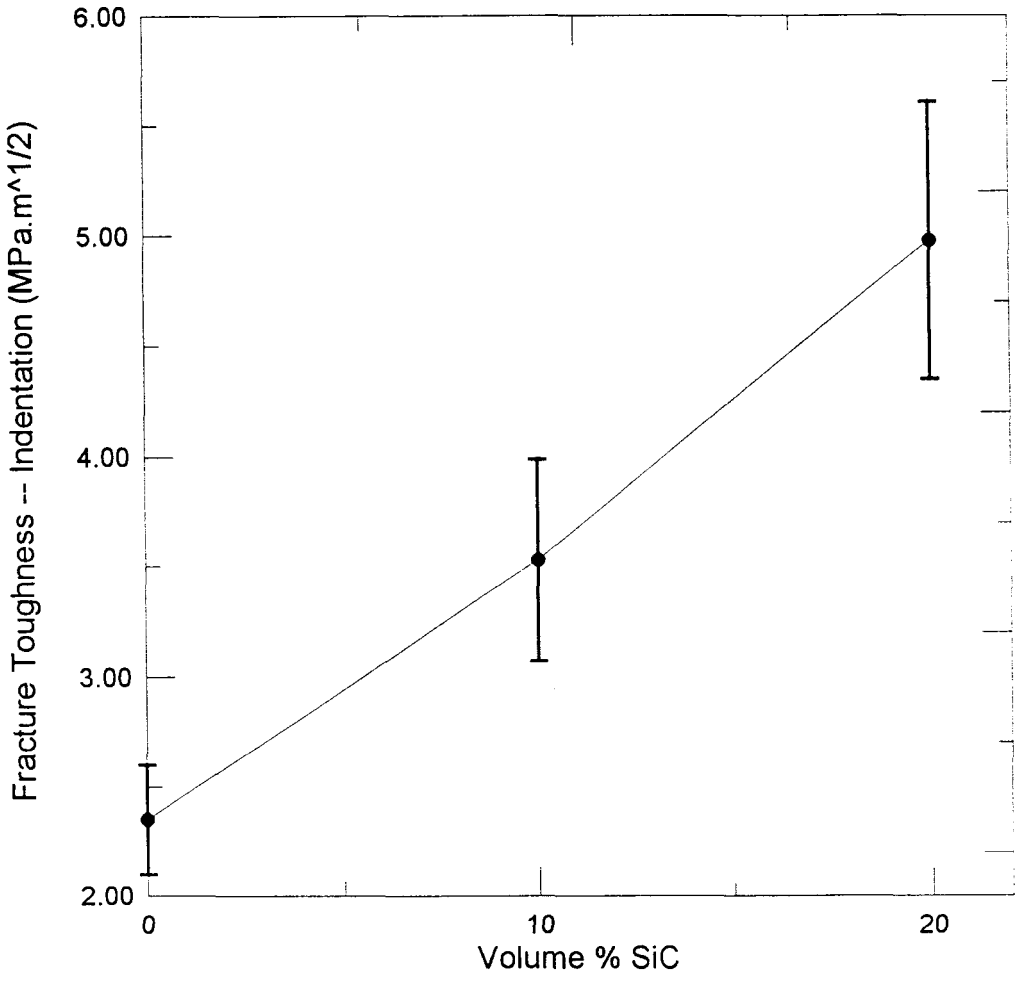

Figure 4-17: Fracture toughness results for $MoSi_2$, 10 vol% and 20 vol% SiC-$MoSi_2$.

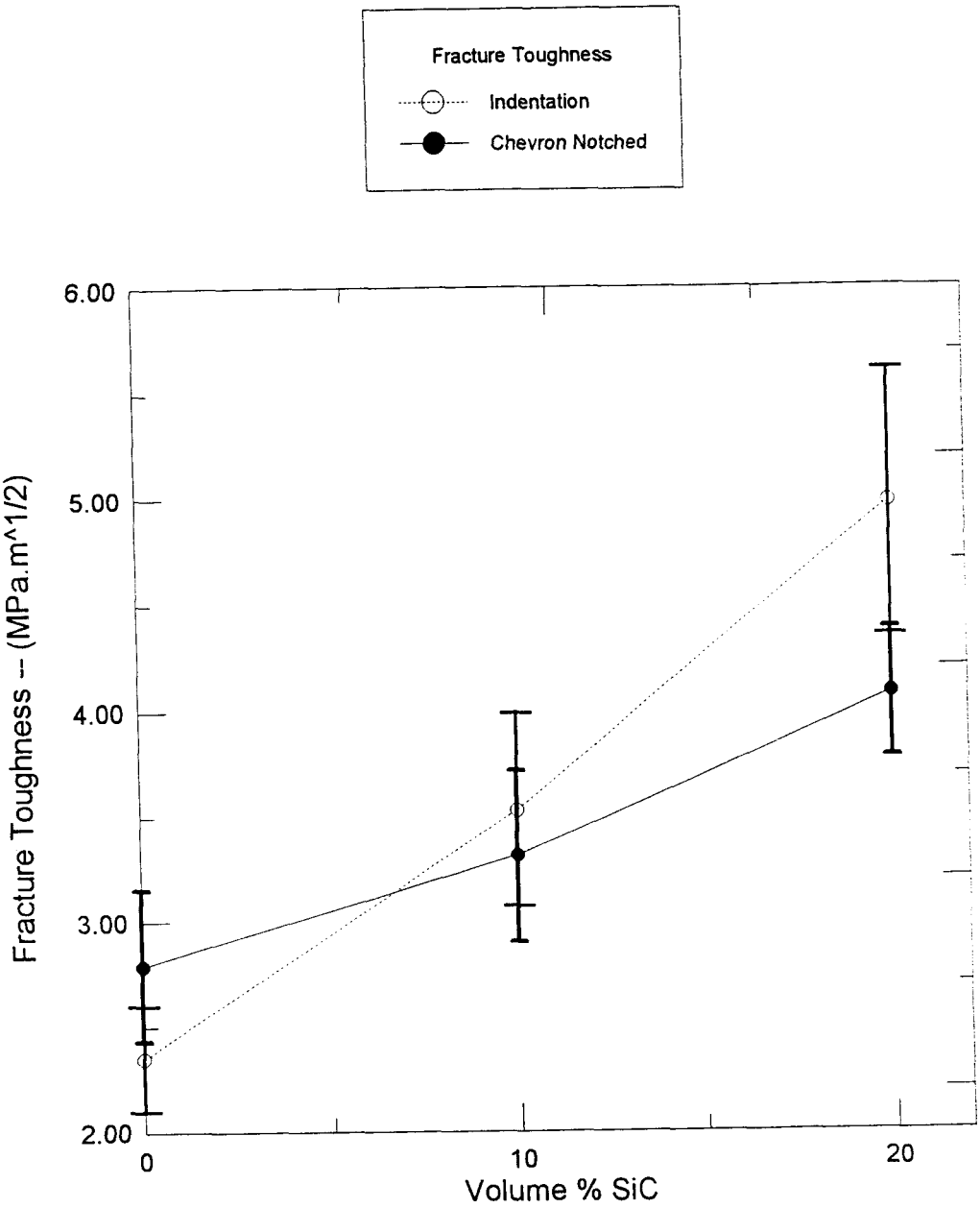

Figure 4-18: Comparison of fracture toughness results between two testing methods.

fracture toughness from 2.35± 0.25 MPa.$m^{1/2}$ to 3.53 ± 0.46 MPa.$m^{1/2}$ and to 4.98±0.63 MPa.$m^{1/2}$ with the introduction of SiC reinforcement.

The results from both fracture toughness methods were reasonably close, proving that the values obtained from the chevron-notch test were reliable. However, the indentation method results should be treated with caution because the indentations did not form fully idealized four-corner radial cracking. There were radial microcracks along the impression together with a few shallow lateral cracks which caused chipping as shown in Figure 4-2. These can introduce errors in the fracture toughness calculation. Furthermore, SiC appeared as a dark phase under the microscope hindering accurate crack measurements.

To characterize the toughening mechanisms, the primary radial cracks were examined in detail using the SEM. Figure 4-19 shows a crack path in $MoSi_2$. Microcracks can be seen along the length of the impression, and it is this local crack net-work that is considered as one of the toughening mechanisms. Crack deflection and crack bridging are the main toughening mechanisms in $MoSi_2$ grains. The crack deflection was not due to the interface debonding between grains, since the crack propagation seemed to adjust and skip (bridging) to follow the low-energy cleavage plane, which arose by the reasons mentioned in Section 4.2.2.

In 20 vol% SiC-$MoSi_2$, cracks were also observed to propagate through the low energy cleavage plane. Figure 4-20 and 4-21 show the crack deflection and bridging in the composite. In addition, the crack appeared to migrate toward the reinforcement where it cut through them, indicating that the interface between the matrix and reinforcement was strong. Since the coefficient of thermal expansion of $MoSi_2$ is about twice that of SiC, and there is

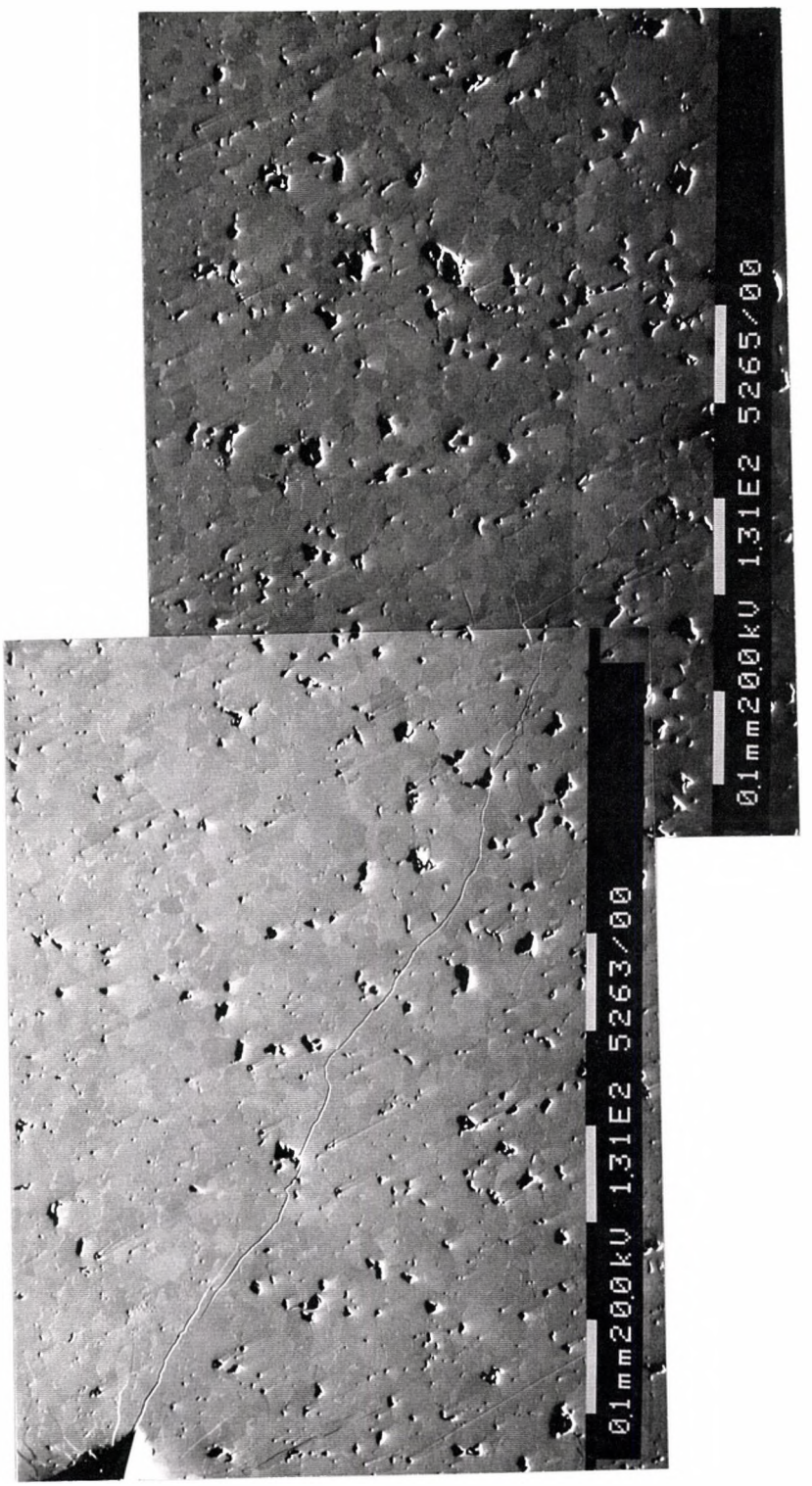

Figure 4-19: Crack propagation in $MoSi_2$.

Figure 4-20: Crack propagation in 20 vol% SiC-$MoSi_2$.

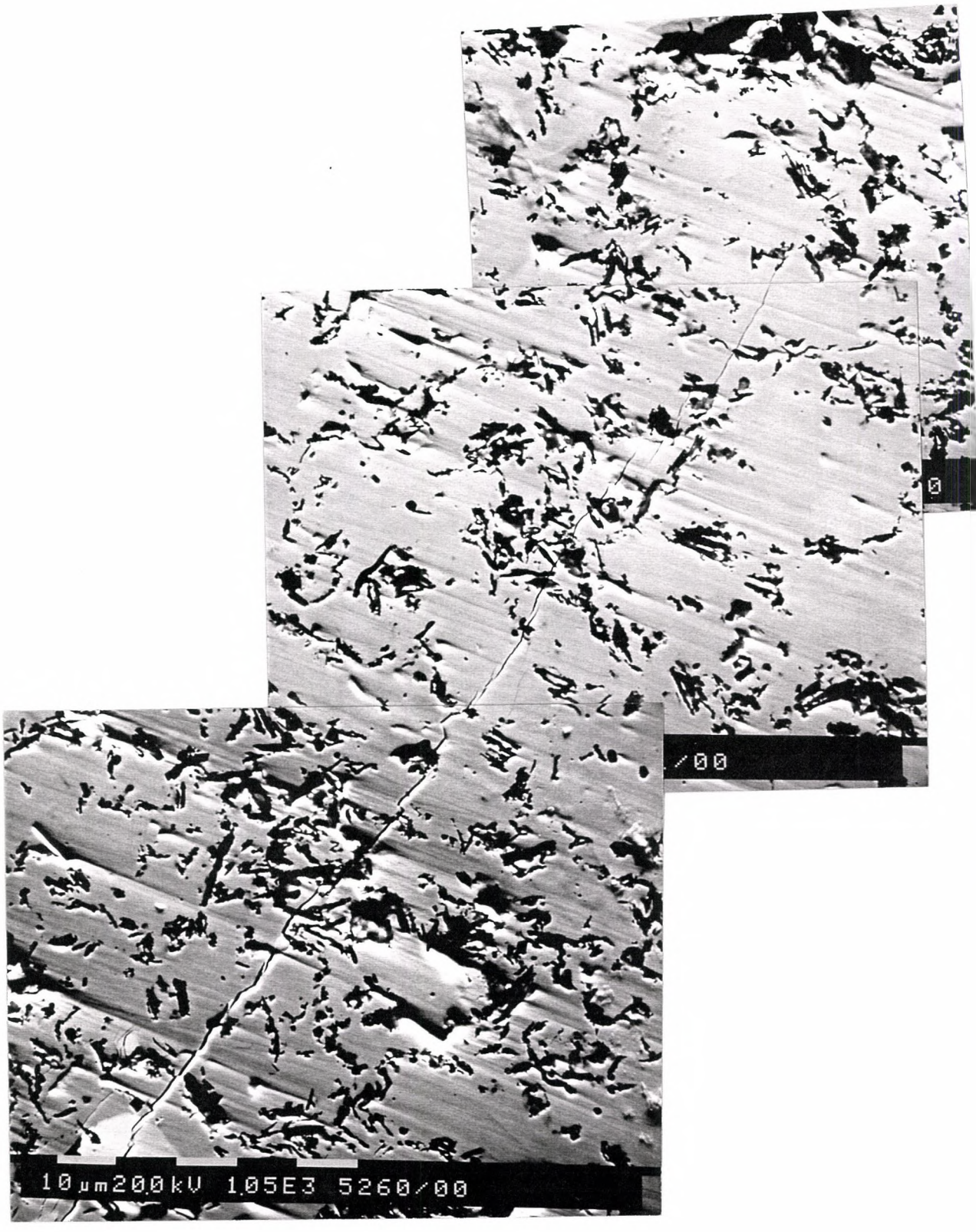

Figure 4-21: Crack propagation in 20 vol% SiC-$MoSi_2$.

a difference in the elastic modulus, the net stress field will cause SiC to be in compression and the matrix to be in tension. Therefore, the crack will be attracted to the reinforcement in order to relieve the compressive stress state of SiC, but, in this case, not enough energy was dissipated by the crack to stop the propagation.

Another toughening mechanism is the fine grain size of the composites. Rice *et al.* (1981a, b) have shown that there is a grain size dependence of the fracture energy (hence toughness) for anisotropic materials. For these materials there is a maximum fracture energy at some intermediate grain size. However, this behavior has not been studied for $MoSi_2$. Therefore, this mechanism due the grain size has yet to be determined.

To conclude this section, there are improvements in all of the room temperature properties with the introduction of the SiC-reinforcement. The increase in hardness and strength are due to the rule-of-mixture strengthening effect arising from the strong interface with low content of SiO_2. The increase in fracture toughness is due to the crack deflection along the direction of the weak cleavage plane in $MoSi_2$, and by the net stress field which leads the crack to the tougher reinforcement in order to dissipate its energy.

V. DISCUSSION AND FUTURE WORK

The objective of producing $MoSi_2$ and SiC- reinforced $MoSi_2$, using combustion synthesis was accomplished. It is worth emphasizing the simplicity, efficiency and effectiveness of this process, which can be used to produce materials with good mechanical properties. All the room temperature mechanical properties tested showed improvement with the introduction of the reinforcement. These results were all comparable to or better than the values obtained from the literature. Some of the results obtained from the particulate-reinforced composites in this work were reasonably close to the results of others obtained for fibre-reinforced composites, which are believed to give superior composites. Only the fracture toughness results in this thesis were lower than those reported elsewhere, but they appear to be valid, because ASTM standard procedures were followed closely. The main fracture mechanism was crack deflection resulting from the residual stress from the difference in coefficients of thermal expansion between the matrix and reinforcement. In addition, microcracks toughening mechanism was observed which is not reported by others. This result was expected, since there was a high stress field in the composites due to both residual and induced stresses.

It is important to note that all the processes reported in the literature involved hot-pressing of $MoSi_2$ powder at high temperatures for several hours. These methods will

promote interfacial reactions between the reinforcement and the matrix, which is detrimental to the room temperature mechanical properties. The reaction will degrade the reinforcement, hence it cannot act as a strengthening and/or toughening phase. With increased time and temperature of processing, grain growth is very likely, and a large net stress field will be introduced in the material. These will decrease both the fracture toughness and the hardness. With the combustion synthesis process, these negative effects can be avoided. The composites fabricated in this study had a strong interface, which lead to effective load transfer, hence improving the hardness and the flexural strength. Also, crack deflection as a toughening mechanism was possible due to the residual stress.

It is important to note that to improve both the room and the high-temperature mechanical properties, a compromise is required, since the conditions that improve the room-temperature mechanical properties may degrade the high temperature properties. For example, fine grain size materials are subjected to a lower net stress field, which improves the mechanical properties at low temperature. However, large grains are required to reduce the grain boundary sliding at high temperatures. For high creep resistance, a strong interface is required for load transfer, but toughening mechanisms like crack deflection by interface debonding and fiber pull out would not be possible. Therefore, suitable reinforcement geometry, interface chemistry, optimal processing conditions and microstructure of the composites needs to be studied further.

In future work, two areas can be identified for improving both the room and high-temperature properties. First, the overall efficiency of the combustion synthesis technique can

be increased if the precursor powder can be simultaneously reacted and densified in a one-step process, as with the hot pressing or HIPing process. The introduction of impurities during the intermediate processing should be reduced in this case. Both have been done successfully only recently by Yang (1995). However, due to proprietary reasons, the details of the procedure were not mentioned. However, their experiment did not involve in-situ forming of the reinforcement. The advantage of in-situ forming of the reinforcement is an area of further study. This one-step combustion synthesis was initially considered for this project, but due to the limitations of the equipment, such as the maximum attainable temperature, and inaccuracies and inconsistencies of the hot-press machine, this process was not attempted.

This study proved that the presence of a few large grains among the finer ones was a source of mechanical flaws. With better preparation of the precursor powder, agglomerates and impurities can be reduced in order to produce better mechanical properties and quality products. The precursor powders can be screened and/or milled to form a uniform distribution of finer powders, assisting in the reduction of large grains in the final products. There is a need for a better densification process such that the time, temperature and pressure can be controlled accurately leading to specimens with a high-density and no interfacial reactions. HIPing is one of the better alternatives, in which a high pressure can be applied at low temperature for a long time.

The second area of further study is the search for the optimal type, orientation and distribution of the reinforcement. High temperature mechanical properties should be performed on the combustion synthesized composites. The objective is to determine the

effect of a strong interface on the strength and fracture toughness at high temperatures and to confirm if the advantages of a strong interface offset those of a weak interface. The interfaces of in-situ formed composites should also be studied to gain an understanding of the reaction mechanism.

Attempts should be made to form other in-situ ceramic whiskers from their elemental powders. The in-situ XD™ process has been shown to produce composites with exceptionally high room temperature fracture toughness. Potential reinforcement materials include TiB_2 and TiC, which have been shown to improve room temperature fracture toughness, and can be produced in-situ by combustion synthesis. However, care should be taken with the combustion of systems with very high adiabatic temperatures, as the properties of the final product may be uncontrollable. The most important parameter is the porosity of the product, which has to be reduced by an effective and efficient densification process. By in-situ forming of whiskers, the handling of health hazard products is lowered, thus the cost can be reduced.

In conclusion, combustion synthesis is a relatively inexpensive and efficient process, with which proper specimen preparation of the elemental powders leads to products with good mechanical properties at room and high temperatures. This process has potential for the fabrication of net shape parts for elevated temperature application. At present, there is little research work published on $MoSi_2$ composites, indicating a need for further research and development before they can be fully realized as a major new class of high temperature structural materials.

REFERENCES

Aikin, R.M.; **1991**, Ceram. Eng. Sci. Proc., **12** [9-10], 1643-1655.

Aikin, R.M.; **1992**, Scripta Metallurgica et Materialia, **26**, 1025.

Adachi, S., Wada, T., Mihara, T., Miyamoto, Y., Koizumi, M. and Yamada, O., **1989**, J. Am. Ceram. Soc., **72**, 805.

Adachi, S., Wada, T., Mihara, T., Miyamoto, Y. and Koizumi, M.; **1990**, J. Am. Ceram. Soc., **73**, 1451.

Adler, T.A. and Houska, C.R.; **1978**, J. Am. Ceram. Soc., **61**, 182-183.

Alman, D.E. and Roebuck, B.; **1978**, Met. Techno., **5**, 92-99.

Alman, D.E., Shaw, K.G., Stoloff, N.S. and Rajan, K.; **1992**, Mater. Sci. Eng., **A155**, 85-89.

Alman, D.E., Hawk, J.A. and Petrovic, J.J.; **1995**, Scripta Metallurgica et Materialia, **32** [11], 1765-1770.

Anstis, G.R., Chantikul, P., Lawn, B.R. and Marshall, D.B.; **1985**, J. Am. Ceram. Soc., **64**, 533-38.

Armstrong, R. and Koszykowski, M.; **1990**, in Combustion and Plasma Synthesis of High Temperature Materials, edited by Munir, Z.A. and Holt, J.B., (VCH, NY), 88.

Ashby, M.F. and Jones, D.R.H.; **1980**, Engineering Material 1: An Introduction to Their Properties and Applications, (Pergamon Press, NY), 59.

ASTM C1161-90, Flexural Strength of Advanced Ceramics at Ambient Temperature, in Annual Book of ASTM Standards, Vol. **15.01**, 333-339.

ASTM E92-82, Standard Test Method for Vickers Hardness of Metallic Materials, in Annual Book of ASTM Standards, Vol. **15.01**, 207-215.

Baglin, J., Dempsey, J., Hammer, W., d'Heurle, F., Peterson, S. and Serrano, C.; **1979**, J. Electro. Mater., **8**, 641-661.

Barin, I., Knacke, K. and Kubachewski, O.; **1977**, Thermophysical Properties of Inorganic Substances, (Springer-Verlag), 442.

Barker, L.M.; **1977**, Eng. Frac. Mech., **9**, 361-369.

Barringer, E.A. and Bowen, H.K.; **1984**, Ceram. Eng. Sci. Proc., **5**, 285-297.

Bartlett, R.W., McCamont, J.W. and Gage, P.R.; **1965**, J. Am. Ceram. Soc., **48**, 551.

Baylin, A. and Matkowsky, B.J.; **1990**, in Combustion and Plasma Synthesis of High Temperature Materials, edited by Munir, Z.A. and Holt, J.B., (VCH, NY), 61.

Berkowitz-Mattuck, J.B., Rossetti, M. and Lee, D.W.; **1970**, Metall. Trans., **1**, 479-483.

Bhaduri, S.B.; **1992**, Scripta Metallurgica et Materialia, **27**, 1277-1281.

Bhattacharya, A.K.; **1991**, Ceram. Eng. Sci. Proc., **12** [9-10], 1697-1722.

Bhattacharya, A.K. and Petrovic, J.J.; **1991**, J. Am. Ceram. Soc., **74**, 2700-703.

Bloshenko, V.N., Bokii, V.V. and Borovinskaya, I.P.; **1985**, Combust. Explos. Shock Waves, **21**, 202

Bloyce, D.M.; **1993**, M. Eng. Thesis, Tape Casting and Mechanical Properties of SiC Platelet Reinforced Alumina, McMaster University, Hamilton, Ontario, Canada.

Bluhm, J.I.; **1975**, Eng. Frac. Mech., **7**, 593-604.

Boldt, P.H., Embury, J.D. and Weatherly, G.C.; **1992**, Mat. Eng. Sci., **A155**, 251-258.

Brewer, L., Lamoreaux, R.H., Ferro, R., Marazza, R. and Girgis, K.; **1980**, Atomic Energy Rev., 7.

Broek, D.; **1982**, Elementary Engineering Fracture Mechanics, (Martinus Nijhoff, Boston).

Buresch, F.E.; **1975**, in Fracture Mechanics of Ceramic, Vol. **4**, edited by Bradt, R.C., Hasselman, D.P.H. and Lange, F.F., (Plenum, NY), 835-847.

Carter, H. and Hurley, G.F.; **1987**, J. Am. Ceram. Soc., **70** [4], C79-C81.

Carter, D.H., Petrovic, J.J., Honnell, R.E. and Gibbs, W.S.; **1989**, Ceram. Eng. Sci. Proc., **12**, 1121-1129.

Campbell, I.E. and Sherwood, E.M.; **1967**, in High Temperature Materials and Technology (Wiley, NY), 401.

Chang, Y.A.; **1969**, J. Mater. Sci., **4**, 641.

Chantikul, P., Anstis, G.R., Lawn, B.R. and Marshall D.B.; **1981**, J. Am. Ceram. Soc., **64** [9], 539-543.

Chen, W., Pascheto, W., Pant, A., Sood, R.R., Holt, R.T and Berriche, R; **1994**, 'Characterization of SHS $MoSi_2$ and MoSi2/SiC/20w Composites' in Proceedings of the 19th Annual Conference on Composites and Advanced Ceramic Materials, Cocoa Beach, FL. to be published in Ceram. Eng. Sci. Proc..

Cook, J. and Gordon, J.E.; **1964**, Proc. Royal Soc. London, **A 282**, 508-520.

Cotton, J.D., Kim, Y.S. and Kaufman, M.J.; **1991**, Mat. Sci. Eng., **A144**, 287.

Davidge, R.W. and Green, T.J.; **1968**, J. Mater. Sci., **3**, 629.

Deevi, S.C.; **1991**, J. Mater. Sci., **26**, 3343-3353.

Deevi, S.C.; **1994**, J. Mater. Sci. Let., **13**, 868-871.

DeHoff, R.T., **1993**, in Thermodynamics in Materials Science, (McGraw-Hill, NY), 496.

Dunmead, S.D., Munir, Z.A. and Holt, J.B., **1992**, J. Am. Ceram. Soc., **75 [1]**, 175-179.

E.N. Sta. Bárbara - Paracuellos del Jarama, Zona Industrial, Ctra, de Belvis, Km. 1, 28860 Madrid, ESPAÑA (SPAIN)

Evans, A.G. and Wilshaw, T.R.; **1976**, Acta. Metall., **24**, 939-956.

Evans, A.G., **1972**, Phil. Mag., **26**, 1327-44.

Evans, A.G., Biswas, D.R. and Fulrath, R.M.; **1979**, J. Am. Ceram. Soc., **62**, 101-106.

Evans, A.G., Meyet, M.E., Fertig, K.W., Davis, B.I. and Baumgartner, H.R.; **1980**, J. Nond. Eval, **1**, 111-122.

Evans, A.G.; **1982**, J. Am. Ceram. Soc., **65**, 127-137.

Evans, A.G.; **1984**, in Science and Technology of Zirconia II, Advances in Ceramics, **12**, edited by Calussen, N., Rühle, M. and Heuer, A.H., (American Ceramics Society, OH), 193-212.

Evans, A.G. and Faber, K.T.; **1984**, J. Am. Ceram. Soc., **67**, 255-260.

Evans, A.G.; **1988**, Mater. Sci. Eng., **A105/6**, 65-67.

Evans, A.G., **1990**, J. Am. Ceram. Soc., **73** [2], 187-206.

Faber, K.T. and Evans, A.G.; **1983**, Acta Metall., **31**, 565-577.

Feng, A. and Munir, Z.A., **1995**, Metallurgical and Materials Tran. B, **Vol 26B**, 581.

Fisher, E.S., Manghnani, M.H., Wang, J. F. and Routbort, J.; **1992**, J. Am. Ceram. Soc., **75**, 908-14.

Fitzer, E., Rubisch, O., Schlichting, J. and Sewdas, I.; **1973**, Sci. Ceram., **XVIII**.

Frankhouser, W.F., Brendley, K.W., Kieszek, M.C. and Sullivan, S.T.; **1985**, in Gasless Combustion Synthesis of Refractory Compounds, (Noyes, New Jersey).

Freiman, S.W.; **1983**, in Fractrure Mechanics of Ceramics, Vol. **6**, edited by Bradt, R.C., Evans, A.G., Hasselman, D.P.H. and Lange, F.F., (Plenum Press, NY), 27-46.

Freiman, S.W.; **1988**, Am. Ceram. Soc. Bull., **67**, 392-402.

Fuller, E.R., Butler, E.P. and Carter, W.C.; **1991**, in Proceedings, Nato Advanced research Workshop: Toughening Mechanisms in quasi-Brittle Materials, NATO ASI Series E, Vol. **195**, edited by Shah, P., (Kluwer Academic, Dordrecht), 385-404.

Gac, F.D. and Petrovic, J.J.; **1985**, J. Am. Ceram. Soc., **68** [8], C200-201.

Gedevanishvili, S. and Munir, Z.A.; **1994**, Scripta Metallurgica et Materialia, **31** [6], 741-743.

Gibbs, W.S., Petrovic, J.J. and Honnell, R.E.; **1987**, Ceram. Eng. Sci. Proc., **8** [7-8], 645-648.

Gillis, P.P. and Gillman, J.J.; **1964**, J. Appl. Phys., **35** [3], 647-658.

Gokhale, A.B. and Abbaschian, G.J.; **1986**, in Binary Alloy Phase Diagrams, edited by Massalski, T.B., (American Society for Metals, Metals Park, Ohio), 1632.

Govindarajan, S., Monroe, K., Moore, J.J., Mishra, Olson, D.L. and Disam, J.; **1994**, in Processing and Fabrication of Advanced Materials III, edited by Ravi, V.A., Srivatsan, T.S. and Moore, J.J., (The Mineral, Metals & Materials Society, PA), 161- 179.

Graff, M.A.C.G., Maat, J.H.H. and Burggraaf, A.J.; **1983**, in Ceramic Powders, edited by Vincenzini, P., (Elsevier Scientific), 783-794.

Green, D.J.; **1981**, J. Am. Ceram. Soc., **64**, 138-41.

Green, D.J.; **1983**, in Fracture Mechanics of Ceramics, Vol. **5**, edited by Bradt, R.C., (Plenum Press, NY), 457-478.

Hanney, M.G. and Morrell, R.; **1982**, Proc. Br. Ceram. Soc., **13**, 277-290.

Hardt, A.P. and Phung, P.V.; **1973**, Combust. Flame, **21**, 77.

Hardwick, D.A., Martin, P.L. and Moores, R.J.; **1992**, Scripta Metallurgica et Materialia, **27**, 391-394.

He, M.Y. and Hutchinson, J.W.; **1989**, Int. J. Solids Structures, **25**, 1053-67.

Henne, R. and Weber, W.; **1986**, High Temp.-High Press., **18**, 223.

Hilliard, J.; **1964**, Metal Prog., **85**, 99-101.

Hlavacek, V., Puszynski, J., Degreve, J. and Kumar, S.; **1986**, Chem. Eng. Sci., **41**, 877.

Hlavacek, V., Dimitriou, P., Degreve, J. and Scholtz, J.; **1990**, in Combustion and Plasma Synthesis of High Temperature Materials, edited by Munir, Z.A. and Holt, J.B., (VCH, New York), 83.

Holt, J.B. and Munir, Z.A.; **1986**, J. Mater. Sci., **21**, 251.

Inglestrom, N. and Nordberg, N.; **1974**, Eng. Fract. Mechs., **6** [3], 597-607.

Inoue, S., Toyokura, N., Nakamura, T. and Ishikawa, H. ; **1981**, J. Electrochem. Soc., **12**, 2402-2410.

Ivanov, V.E., Nechiporenko, E.P., Zmii, V.I. and Kirvoruchko, V.M.; **1967**, in Diffusion Cladding of Metals, edited by Samsonov, G.V., Consultants Bureau, (Plenum, NY), 29.

Jang, J.S.C. and Koch, C.C.; **1990**, J. Mater. Res., **5**, 498.

Jayashankar, S. and Kaufman, M.J.; **1993**, J. Mater. Res., **8**, 1428-41.

Jayashankar, S, Riddle, S.E. and Kaufman, M.J.; **1994**, in Material Research Society Symposium Proceedings, **322**, edited by Briant, C.L., Petrovic, J.J., Bewley, B.P., Vasudevan, A.K. and Lipsitt, H.A., (Materials Research Society, PA), 33-40.

Jayashankar, S, Riddle, S.E. and Kaufman, M.J.; **1994**, in Material Research Society Symposium Proceedings, **322**, edited by Briant, C.L., Petrovic, J.J., Bewley, B.P., Vasudevan, A.K. and Lipsitt, H.A., (Materials Research Society, PA), 71-79.

Jeryan, R.A.; **1978**, in Ceramics for High-Performance Application II, edited by Lenoe, E.M., (Brool Hill), 35-51.

Kayuk, V.G., Kuzenkova, M.A., Dolykhanyan, S.K. and Sarkisyan, A.R.; **1978**, Sov. Powder Metall. Met. Ceram., **188**, 588.

Kecskes, L.J., Kohke, T. and Niler, A.; **1990**, J. Am. Ceram. Soc., **73**, 1274.

Kellett, B. And Lange, F.F.; **1984**, J. Am. Ceram., Soc., **67**, 369-371.

Khaikin, B.I. and Merzhanov, A.G.; **1966**, Combust. Explos. Shock Waves USSR, **2**, 22.

Khaikin, B.I. and Merzhanov, A.G.; **1966**, Ind. Eng. Chem. Res., **2**, 22.

Khaikin, B.I.; **1975**, Combustion Processes in Chemical Technology and Metallurgy, edited by Merzhanov, A.G., (Chernogolovka), 227.

Kingery, W.D., Bowen, H.K. and Uhlmann, D.R.; **1976a**, in Introduction to Ceramics, 2nd edn., (Wiley-Interscience, NY), 788.

Kingery, W.D., Bowen, H.K. and Uhlmann, D.R.; **1976b**, in Introduction to Ceramics, 2nd edn., (Wiley-Interscience, NY), 469-490.

Knott, J.F.; **1973**, in Fundamental of Fracture Machanics, (Butterworth, London), 94-113.

Knott, J.F.; **1973**, in Fundamental of Fracture Machanics, (Butterworth, London), 114-149.

Lakshmikantha, M.G. and Sekhar, J.A., **1993**, J. Mat. Sci., **28**, 6403.

Lange, F.F.; **1970**, Phil. Mag., **22**, 983-92.

Lange, F.F. and Metcalfe, M.; **1983**, J. Am. Ceram. Soc., **66**, 398-406.

Lange, F.F., Davis, B.I. and Aksay, I.A.; **1983**, J. Am. Ceram. Soc., **66**, 407-408.

Lange, F.F.; **1989**, J. Am. Ceram. Soc., **72** [1], 3-15.

Lawn, B.R. and Marshall, D.B.; **1979**, J. Am. Ceram. Soc., **62**, 347-350.

Lawn, B.R., Evans, A.G. and Marshall, D.B.; **1980**, J. Am. Ceram. Soc., **63**, 574-581.

Lawn, B.R.; **1993a**, Fracture of Brittle Solids, 2nd edition, (Cambridge University Press, UK), 222.

Lawn, B.R.; **1993b**, Fracture of Brittle Solids, 2nd edition, (Cambridge University Press, UK), 210.

Lawn, B.R.; **1993c**, Fracture of Brittle Solids, 2nd edition, (Cambridge University Press, UK), 224.

Lee, E.W., Cook, J., Khan, A., Mahapatra., R and Waldman, J.; **1991**, JOM, **43** [3], 54-57.

Lu, T.C., Yang, J., Suo, Z., Evans, A.G., R. Hecht and Mehrabian R.; **1991**, Acta Metall. Mater., **39**, 1883-1890.

Ma, E., Pagan, J., Cranford, G. and Atzmon, M.; **1993**, J. Mater. Res., **8**, 1836-44.

Maksimov, E.I. and Shkadinskii, K.G.; **1971**, Combust. Explos. Shock Waves USSR, 7, 392.

Maloy, S. A., Heuer, A.H., Lewandowski, J.J. and Mitchell, T.E.; **1992**, Acta Metall. Mater., **40** [11], 3159-3165.

Maloy, S. A., Heuer, A.H., Lewandowski, J.J. and Petrovic, J.J.; **1991**, J. Am. Ceram. Soc., **74** [10], 2704-2706.

Marshall, D.B. and Lawn, B.R.; **1979**, J. Mater. Sci., **14**, 2001-2012.

Marshall, D.B. and Ritter, J.E.; **1987**, Am. Ceram. Soc. Bull., **66**, 309-317.

Matveiko, N.P. and Khramtsov, P.G.; **1989**, Khim. Prom-st., **3**, 201.

Maxell, W.A.; **1951**, Proceeding of the Metallurgy and Materials Information Meeting, Vol. 1, Report No. TID-5061, Journal announcement; NSA 12.

McColm, I.J.; **1990**, in Ceramics Hardness, (Plenum, New York).

Mendelson, M.I., **1969**, J. Am. Ceram. Soc., **52**, 433-46.

Merzhanov, A.G. and Borovinskaya, I.P., **1972**, Dokl. Akad. Nauk. SSSR (Chem), **204**, 429-32.

Merzhanov, A.G. and Borovinskaya, I.P., **1975**, Comb. Sci. Tech., **10**, 195.

Merzhanov, A.G., Novikov, N.P. and Borovinskaya, I.P.,; **1975**, in Combustion Processes in Chemical Technology and Metallurgy, edited by Merzhanov, A.G., (Chernogolovka), 174.

Merzhanov, A.G.; **1990**, in Combustion and Plasma Synthesis of High Temperature Materials, edited by Munir, Z.A. and Holt, J.B., (VCH, New York), 1.

Meschter, P.J.; **1991**, Mat. Res. Soc. Symp. Proc., **213**, 1027-1032.

Meschter, P.J. and Schwartz, D.S.; **1989**, JOM, **41**, 52-55.

MIL-STD 1942(A); **1983**, Flexural Strength of High Performance Ceramics at Ambient Temperaturem, in U.S. Army Military Standard, U.S. Army Materials Technology Laboratory, Waterdown, MA.

Miyamoto, Y., Koizumi, M. and Yamada, O.; **1984**, J. Am. Ceram. Soc., **67**, C-224.

Miyamoto, Y.; **1990**, Am. Ceram. Soc. Bull., **69**, 686.

Morgolis, S.B., Matkowsky, B.J. and Botty, M.R., **1990**, in Combustion and Plasma Synthesis of High Temperature Materials, edited by Munir, Z.A. and Holt, J.B., (VCH, New York), 73.

Munroe, P.R. and Baker, I.; **1988**, Metals and Materials, **7**, 435-438.

Munz, D., Shannon, Jr., J.L. and Bubsey, T.; **1980**, Int. J. Frac., **16**, R137-41.

Munz, D., Bubsey, R.T. and Shannon Jr., J.L.; **1981**, J. Am. Cerm. Soc., **63**, 300-306.

Munz, D.; **1983**, in Fracture Mechanics of Ceramics, Vol. **5**, edited by Brandt, R.C., (Plenum, NY), 457-78.

Munir, Z.A. and Anselmi-Tamburni, U.; **1989**, Materials Reports, **3**, 277-365.

Munz, D.G., Shannon Jr., J.L. and Bubsey, T.; **1980**, Int. J. Fracture, **16**, R137-41.

Murarka, S.P.; **1983**, in Silicides for VLSI Aplication, (Academic Press, NY).

Nakamura, M.; **1994**, Metallurgical and Materials Transaction A, **25A**, 331-340.

Newman, J.C.; **1984**, in Chevron-Notched Specimens: Testing and Stress Analysis, edited by Underwood, J.H., ASTM STP 855, 5-31.

Nose, T. and Fujii, T.; **1988**, J. Am. Ceram. Soc., **71**, 328-333.

Novikov, N.P.; **1960**, Dokl. Akad. Nauk, **131**, USSR, 1400.

Novikov, N.P.; **1962**, Dokl. Akad. Nauk, **142**, USSR, 1328.

Novikov, N.P., Borovinskaya, I.P. and Merzhanov, A.G.; **1975**, in Combustion Process In Chemical Technology and Metallurgy, edited by Merzhanov, A.G., (Chernogolovka), 174.

Olesinski, R.W. and Abbaschian, G.J.; **1984**, Bull. Alloy Phase Diagrams, **5**, 5.

Orawan, E.; **1949**, Rep. Prog. Psy., **12**, 185.

Ostojic, P. and McPherson, R.; **1987**, Int. J. of Fract., **33**, 297-312.

Parthe, E., Jeitschko, W. and Sadagopan, V.; **1965**, Acta Crystallogr., **19**, 1031-1037.

Pampuch, P. And Haberko, K.; **1983**, in Ceramic Powders, edited by Vincenzini, P., (Elsevier Scientific, Amsterdam, 623-624.

Patankar, S.N., Xiao, S.Q., Lewandowski, J.J. and Heuer, A.H.; **1993**, J. Mater. Res., **8**, 1311-6.

Patibandla, N. and Hillig, W.B.; **1993**, J. Am. Ceram. Soc., **76**, 1630-34.

Petric, A., Yi, H.C. and Yang, W.Y.; **1993**, in ASM/AIME Conf. Proc., Edited by Ravi, V.A. and Srivatsan, (Pittsburgh, PA).

Petrovic, J.J. and Jacobson, L.A.; **1974**, in Ceramics for High Performance Applications, edited by Burke, J.J.m Gorum, A.E. and Katz, R.N., (Chestnut Hill, Mass.), 397-414.

Petrovic, J.J. and Jacobson, L.A., Talty, P.K. and Vasudevan, A.K.; **1975**, J. Am. Ceram. Soc., **58** [3-4], 113-66.

Petrovic, J.J. and Honnell, R.E.; **1990**, Ceram. Eng. Sci. Proc., **11** [7-8], 734-744.

Petrovic, J.J. and Honnell, R.E.; **1990**, J. of Mater. Sci., **25**, 4453-4456.

Petrovic, J.J., Honnell, R.E., Mitchell, T.E., Wade, R.K. and McClellan, K.J.; **1991**, Ceram. Eng. Sci. Proc., **12** [9-10], 1633-1642.

Petrovic, J.J.; **1995**, Mater. Sci. Eng., **A192/193**, 31-37.

Polanyi, M.; **1921**, Z. Phys., 7, 323.

Poter, D.L., Evans, A.G. and Heuer, A.H.; **1979**, Acta. Metall., **27**, 1649-54.

Porter, D.A. and Eastering K.E.; **1989**, in Phase Transformations in Metals and Alloys, T.L. Press, Cornwall, UK), 74.

Puszynski, J., Degreve, J. and Hlavaek, V.; **1987**, Ind. Eng. Chem. Res., **26**, 1424.

Rajaiah, J., Dandekar, H., Puszynski, J., Degreve, J. and Hlavacek, V.; **1988**, Ind. Eng. Chem. Res., **27**, 513.

Reed, J.S., Carbone, T. and Scott, C.; **1978**, in Materials Science and Research, Vol. **11**, edited by Palmour, H., (Plenum Press, NY), 171-180.

Richardson, G.Y., Rice, R.W. and McDonough, W.J.; **1986**, Ceram. Eng. Sci. Proc., **7**, 761.

Richardson, K.K. and Freitag, D.W.; **1991**, Ceram. Eng. Sci. Proc., **14**, 1679-1689.

Rice, R.W. and Hockey B.J.; **1979**, The Science of Ceramics Machining and Surface Finishing II, NBS Special Publication 562.

Rice, R.W., Freman, S.W. and Becher, P.F.; **1981a**, J. Am. Ceram. Soc., **64** [6], 345-349.

Rice, R.W., Freman, S.W. and Becher, P.F.; **1981b**, J. Am. Ceram. Soc., **64** [6], 350-354.

Rice, R.W.; **1981**, Ceram. Eng. Sci. Pro., **2** [7-8], 661-701.

Rice, R.W. and McDonough, W.J.; **1985**, J. Am. Ceram. Soc., **68**, c-122.

Rice, R.W., McDonough, W.J., Richardson, G.Y., Kunutz, J.M. and Schroeter, T.; **1986**, Ceram. Eng. Sci. Proc., 7, 751.

Rice, R.W.; **1986**, Ceram. Eng. Sci. Proc., **11**, 1203.

Rühle, M. and Heuer, A.H.; **1984**, in Science abd technology of Zirconia II, Advances In Ceramics, Vol. **12**, edited by Claussen, N., Rühle, M. and Heuer, A.H., (Am. Ceram. Soc., Ohio).

Rühle, M., Claussen, N. and Heuer, A.H.; **1986**, J. Am. Ceram. Soc., **69**, 195-7.

Rühle, M. And Evans, A.G.; **1989**, Progress in Materials Science, **33**, 85-167.

Sadananda, K. and Feng C.R.; **1993**, Mater. Sci. Eng., **A170**, 199-214.

Sadananda, K., Feng C.R., Jones H. and Petrovic J.J.; **1992**, Mater. Sci. Eng., **A155**, 227.

Salem, J.A. and Shannon Jr., J.L.; **1987**, J. Mater. Sci., **22**, 321-4.

Samsonov, G.V.; **1959**, in Silicidies and Their Use in Engineering, (Akad. Nauk. Ukr. SSR, Kiev), **44**, 106-112.

Samsonov G.V., Kislyi, P.S.; **1967**, in High Temperature Non-Metallic Thermocouples and Sheaths, Consultants Bureau, (Plenum, NY), 103.

Samsonov, G.V. and Vinitiskii, I.M.; **1980**, Handbook of Refractory Compounds, (Plenum Press, NY).

Scherg, P.; **1988**, Elecktrowaerme Int. Edn., **B46**, 248.

Schlichting, J.; **1978**, High-Temp.-High Press., **10**, 241.

Schwarz, R.B., Srinivasan, S.R., Petrovic, J.J. and Maggiore, C.J.; **1992**, Mater. Sci. Eng., **A155**, 75-83.

Schreiber, E. Anderson, O.L. and Soga N.; **1973**, in Elastic Constants and Their Measurements, (McGraw-Hill Book Company, NY), 6.

Sibieude, F. and Benezech G.; **1989**, J. Mater. Sci. Let., **8**, 1323.

Shih, T.T.; **1979**, Eng, Frac. Mech., **12**, 479-498.

Steinbrech, R.W.; **1992**, J. Eur. Ceram. Soc., **10**, 131-142.

Subrahmanyam, J., Vijayakumar, M. and Ranganath, S.; **1989**, Met. Mater. Proc., **1**, 105.

Subrahmanyam, J.; **1993**, J. Am. Ceram. Soc., **76** [1], 226-228.

Subrahmanyam, J.; **1994**, J. Mater. Res., **9** [10], 2620-2626.

Subrahmanyam, J. and Mohan Rao, R.; **1994**, Mater. Sci. Eng., **A183**, 205.

Subrahmanyam, J. and Mohan Rao, R.; **1995**, J. Am. Ceram. Soc., **78** [2], 487-490.

Sung, J.; **1988**, Ph.D. Thesis, Defect-Initiated Fracture and Strength of Ceramics, McMaster University, Hamilton, Ontario, Canada.

Suzuki, M., Nutt, S.R. and Aikin, R.M.; **1993**, Mater. Sci. Eng., **A162**, 73-82.

Swain, M.V.; **1976**, J. Mater. Sci., **11**[12], 2345-48.

Tien, J.K., Vignoul, G.E. and Kopp, W.M.; **1991**, Mater. Sci. Eng., **A143**, 43.

Tiwari, R., Herman, H. and Sampath S.; **1992**. Mater. Sci. Eng., **A155**, 95-100.

Tuffe, S.E., Plucknett, K.P. and Wilkinson, D.S.; **1993**, Ceram. Eng. Sci. Proc., **14**, 1199-1208.

Unal, O., Petrovic, J.J., Carter, D.H. and Mitchell, T.E.; **1990**, J. Am. Ceram. Soc., **73** [6], 1752-1757.

Vahldiek, F.W. and Mersol, S.A.; **1968**, J. Less-Common Met., **15**, 165-171.

Vasudévan A.K. and Petrovic J.J.; **1992**, Materials Science and Engineering, **A155**, 1-17.

Wade, R.K. and Petrovic, J.J.; **1992a**, J. Am. Ceram. Soc., **75** [6], 1682-1684.

Wade, R.K. and Petrovic, J.J.; **1992b**, J. Am. Ceram. Soc., **75** [11], 3160-62.

Wang, L.L. and Munir Z.A.; **1995**, Metal. Mat. Tran. B, **26B**, 595-601.

Weherman, R.; **1967**, in High Temperature Materials and Technology, edited by Campbell, I.E. and Sherwood, E.M., (Wiley, NY), 399.

Wiederhorn, S., Gettings, R.J., Roberts, D.E., C. Ostertag, C. and Petrovic, J.J.; **1992**, Mater. Sci. Eng., **A155**, 209.

Whitehead, M.W.; **1994**, M. Eng. Thesis, Synthesis and Mechanical Properties of Electrophoretically Deposited Alumina/Zirconia Laminated Composites, McMaster University, Hamilton, Ontario, Canada.

Yamada, O., Miyamoto, Y. and Koizumi, M.; **1985**, Am. Ceram. Soc. Bull., **64**, 19.

Yang, J.M. and Jeng, S.M.; **1991**, J. Mater. Res., **6** [3], 505-513.

Yi, H.C. and Moore J.J.; **1989**, J. Mat. Sci. Let., **8**, 1182-1184.

Yi, H.C. and Moore J.J.; **1990**, J. Mat. Sci., **25**, 1159-1168.

Yi, H.C., Petric, A. and Moore, J.J.; **1992**, J. Mat. Sci., **27**, 6797-6806.

Zeitsch, K. and Fitzer, E.; **1970**, High Temp.-High Press., **2**, 241.

Zhang, S. and Munir, Z.A.; **1991**, J. Mat. Sci., **26**, 3685-3688.